# Snow and Glacier Melt Contributions and SLA-ELA Relationship in Himalayan Basins

**Ph.D. Thesis**

*by*

**PARUL VINZE**

**Department of Civil Engineering**
**Indian Institute of Technology Indore**
**January 2026**

# Snow and Glacier Melt Contributions and SLA-ELA Relationship in Himalayan Basins

**A Thesis**

*Submitted in partial fulfillment of the*
*requirements for the award of the degree of*

**DOCTOR OF PHILOSOPHY**

*by*

**PARUL VINZE**

**Department of Civil Engineering**
**Indian Institute of Technology Indore**
**January 2026**

# Indian Institute of Technology Indore

I hereby certify that the work which is being presented in the thesis entitled "**Snow and Glacier Melt Contributions and SLA-ELA Relationship in Himalayan Basins**" in the partial fulfilment of the requirements for the award of the degree of **Doctor of Philosophy** and submitted in the **Department of Civil Engineering, Indian Institute of Technology Indore**, is an authentic record of my own work carried out during the time period from July 2019 to September 2025 under the supervision of Dr. Mohd. Farooq Azam, Associate Professor, Department of Civil Engineering, Indian Institute of Technology Indore.

The matter presented in this thesis has not been submitted by me for the award of any other degree of this or any other institute.

Parul Vinze

Signature of the Student

(Parul Vinze)

---

This is to certify that the above statement made by the candidate is correct to the best of my knowledge.

Mohd. Farooq Azam

Signature of Thesis Supervisor

(Dr. Mohd. Farooq Azam)

---

**Parul Vinze** has successfully given her Ph.D. Oral Examination held on 07 Jan 2026

Mohd. Farooq Azam

Signature of Thesis Supervisor

(Dr. Mohd. Farooq Azam)

# ACKNOWLEDGEMENTS

First and foremost, I thank God for providing me strength, patience and resilience throughout this journey. Without that divine presence, the completion of this work would not have been possible.

I am profoundly grateful to my supervisor, Dr. Mohd. Farooq Azam, for his invaluable guidance and constant support throughout the course of this research. His encouragement, patience, and thoughtful mentorship during challenging times have been an immense support. I am especially thankful for his constant motivation, insightful advice and faith in my abilities, which have shaped not only the direction of this work but also my academic journey and personal growth. I am truly fortunate to have had the opportunity to work with him.

I would like to express my heartfelt gratitude to Dr. Adina E Racoviteanu for her continuous support and guidance throughout this research. Her generous sharing of knowledge has been a constant source of motivation. It has been a privilege to collaborate with her and learn from her expertise.

I would also like to express my sincere gratitude to my PG Student's Progress Committee members, Prof. Sandeep Chaudhary and Dr. Lalit Borana, for their insightful feedback and constructive suggestions, which have greatly strengthened and enriched this work.

I would like to thank the Department of Civil Engineering for all their support and IIT Indore for giving me this opportunity to be a part of IIT community.

Special thanks to my friends Smriti, Sushmita, Abhishek, Rosa and Ghulam for their invaluable support during my difficult times. I am also thankful to Arif, Himanshu, Sachin and Manoj for their support throughout this journey.

My deepest gratitude goes to my parents and my grandparents for their unconditional love and support; their sacrifices and values have been my foundation. A big thanks to my brother and my sister-in-law for their support, constant encouragement and care. I am very grateful to my in-laws for their support and patience throughout this journey.

A very special thanks to my husband, Rishi, whose support, patience and encouragement have carried me through every challenge, he has been my greatest strength and I feel blessed to have him by my side.

To all who, in ways big or small, have contributed to this work and walked alongside me on this path, I offer my heartfelt thanks.

***Dedicated to my beloved family***

# ABSTRACT

Snow and glacier meltwater are critical hydrological components in the glacierized and snow-covered basins of the Himalaya-Karakoram (HK), yet their accurate quantification remains challenging due to limited in-situ observations in this remote and rugged terrain. This thesis aims to advance the understanding of meltwater dynamics, improve modelling approaches, and enhance glacier monitoring techniques using remote sensing to better assess hydrological responses of glacierized basins to climatic variability in the region. The thesis focuses on three glacierized basins situated in distinct climatic regimes of HK. In the western Himalaya, the Snowmelt Runoff Model (SRM) was applied in the Chandra-Bhaga Basin, using a data-rich reference catchment of Chhota Shigri Glacier to constrain key parameters from extensive field observations, while the remaining parameters were calibrated against observed discharge. Daily discharge simulations for 2003–2018 indicated that flow was primarily controlled by summer temperature in the Chhota Shigri Catchment and by summer SCA at the basin scale. Although parameters calibrated in the reference catchment produced good results at the catchment scale, their direct application to the basin scale resulted in substantial overestimation of discharge, indicating that the parameters are not transferable even within the same basin. In the central Himalaya, the long-term melt contributions and their climatic controls in the Gangotri Glacier System (GGS) were examined over 1980–2020, by applying a high-resolution glaciohydrological model Spatial Processes in Hydrology (SPHY) forced with Indian Monsoon Data Assimilation and Analysis reanalysis data. Two-tier calibration using in-situ discharge and geodetic mass balance estimates, and validation against improved MODIS snow cover data, showed that snowmelt contributed 64%, glacier melt 21% followed by rainfall-runoff 11% and baseflow 4%. A shift in the discharge peak from August to July after 1990 was attributed to reduced winter precipitation and enhanced early summer melting. Summer precipitation and winter temperature were identified as the dominant climatic controls on annual discharge. In Dudh Koshi Basin of the central Himalaya, an improved method for snowline altitude (SLA) extraction was developed and applied to assess the relationship of SLA with the equilibrium line altitude (ELA). Comparisons on Mera Glacier therein revealed that remotely sensed end-of-ablation season SLA ($SLA_{max}$) consistently underestimated field-based ELA, challenging the common assumption that $SLA_{max}$ approximates ELA in monsoon-dominated regions. The observed discrepancies were linked to surface processes such as sublimation, wind erosion, and snow redistribution, underscoring the need for caution when using SLA as a proxy for ELA in this region. By integrating enhanced modelling frameworks with improved remote sensing approaches, this work provides new insights into the hydrological behaviour of Himalayan glacierized basins. The sensitivity of discharge to climatic factors and the limitations of parameter transferability and ELA proxy, thereby contributing to more robust water resource assessments under changing climate conditions.

# LIST OF PUBLICATIONS

## A. Publications from Ph.D. thesis work:

1. **Vinze, P.** and Azam, M. F. 2023. On the transferability of snowmelt runoff model parameters: Discharge modeling in the Chandra-Bhaga Basin, western Himalaya. Frontiers in Water, 4, p.1086557. Doi: 10.3389/frwa.2022.1086557 (IF 2.8)
2. **Vinze, P.**, Hussain, G., Srivastava, S., Azam, M. F., Hussain, M. A. and Haritashya, U. 2025. Hydrological contributions of snow and glacier melt from the Gangotri Glacier System and their climatic controls since 1980. Journal of the Indian Society of Remote Sensing. https://doi.org/10.1007/s12524-025-02274-0 (IF 2.2)

## B. Articles under review:

1. **Vinze, P.**, Racoviteanu, A. E., Azam, M. F. and Wagnon, P. Challenges in estimating ELAs from satellite imagery in monsoon-dominated regions: Dudh Koshi basin, central Himalaya. Journal of Glaciology (IF 2.6)

## C. List of conferences

1. **Vinze, P.** and Azam, M. F.: Evaluation of Parameter Transferability of Snowmelt Runoff Model in Chandra-Bhaga Basin, India, EGU General Assembly 2023, Vienna, Austria, 24–28 Apr 2023, EGU23-534, https://doi.org/10.5194/egusphere-egu23-534
2. **Vinze, P.**, Racoviteanu, A. and Azam, M. F.: Challenges in Snowline Estimation from Optical Imagery: Case Studies from Chhota Shigri and Mera glaciers, Himalaya, AGU annual meeting 2023, San Francisco, CA, 11–15 Dec 2023, https://ui.adsabs.harvard.edu/abs/2023AGUFM.C44B..07V/abstract

# TABLE OF CONTENTS

# LIST OF TABLES

# LIST OF FIGURES

# ACRONYMS

| | |
|---|---|
| Himalaya-Karakoram | HK |
| Snow line altitude | SLA |
| Equilibrium line altitude | ELA |
| Snowmelt runoff model | SRM |
| Snow cover area | SCA |
| Spatial Processes in Hydrology | SPHY |
| Gangotri Glacier System | GGS |
| Indian summer monsoon | ISM |
| Western Disturbances | WDs |
| Near infrared | NIR |
| Shortwave infrared | SWIR |
| Normalized difference snow index | NDSI |
| Accumulation area ratio | AAR |
| Automatic weather station | AWS |
| Digital elevation model | DEM |
| Lapse rate | LR |
| Land use landcover | LULC |
| Rainfall contributing area | RCA |

# Chapter 1

# Introduction

## 1.1 Himalaya-Karakoram and its importance

High mountain regions play a crucial role in the hydrological cycle, storing and releasing freshwater that sustains populations far beyond the mountain boundaries. Among these, the Himalaya-Karakoram (HK) region holds a particularly important position, being one of the largest glacierized regions outside the polar areas and often referred to as the “Water Tower of Asia” (Immerzeel et al., 2020; Azam et al., 2021). The HK region stretches across parts of Afghanistan, Pakistan, India, Nepal, Bhutan, and China, encompassing some of the highest peaks in the world. Its glaciers, perennial snow cover, and permafrost collectively store an immense volume of water, acting as a natural reservoir that regulates river flows across multiple climatic zones.

The meltwater from HK glaciers and snowfields feeds largest river systems, notably the Indus, Ganga, and Brahmaputra. These rivers originate in the high mountains and flow through densely populated agricultural plains before reaching the sea. Together, they provide water for drinking, irrigation, hydropower, and industrial activities to more than a billion people (Azam et al., 2021; Nepal et al., 2023). The Indus River basin is one of the most glacier and snowmelt dependent basin, with meltwater contributing a substantial proportion of its annual flow, particularly during the summer months (Bookhagen and Burbank, 2010; Lutz et al., 2014; Immerzeel et al., 2020). The Ganga and Brahmaputra basins, although more influenced by monsoon rainfall, also depend on seasonal snowmelt and glacier melt to sustain flows during the pre-monsoon and dry season (Lutz et al., 2014; Azam et al., 2021).

This glacier and snowmelt contribution is particularly critical during dry periods, when meltwater buffers the seasonal variability of precipitation (Pritchard, 2019; Immerzeel et al., 2020). It supports agricultural production, hydropower generation especially during lean flows, and sustains ecosystems dependent on perennial streams (Pritchard, 2019; Immerzeel et al., 2020). Therefore, the HK region is therefore not only a vital environmental system but also an essential socio-economic resource.

## 1.2 Climatic regimes in HK

The HK region is not climatically uniform; rather, it spans multiple climatic regimes that influence the hydrology and cryospheric processes in distinct ways. The western Himalaya and Karakoram are primarily influenced by western disturbances (WDs), receiving most of their annual precipitation in the form of snowfall (Thayyen and Gergan, 2010). As a result, summer flows in rivers such as the Indus are dominated by snow and glacier melt (Bookhagen and Burbank, 2010; Azam et al., 2021).

The central and eastern Himalaya are predominantly monsoon-fed, with the majority of annual precipitation occurring June through September (Thayyen and Gergan, 2010). Snow and glacier melt play a smaller role in total discharge compared to rainfall, but they can still be important during the pre-monsoon season and in high-altitude catchments (Lutz et al., 2014; Azam et al., 2021). These spatial variations mean that climate change impacts will not be uniform across the HK region; some areas may experience short-term increases in meltwater followed by declines, while others may be more affected by changes in rainfall patterns (Lutz et al., 2014). To capture the range of climatic and hydrological conditions in HK, this thesis focuses on three glacierized basins distributed across the western and central Himalaya (Figure 1.1).

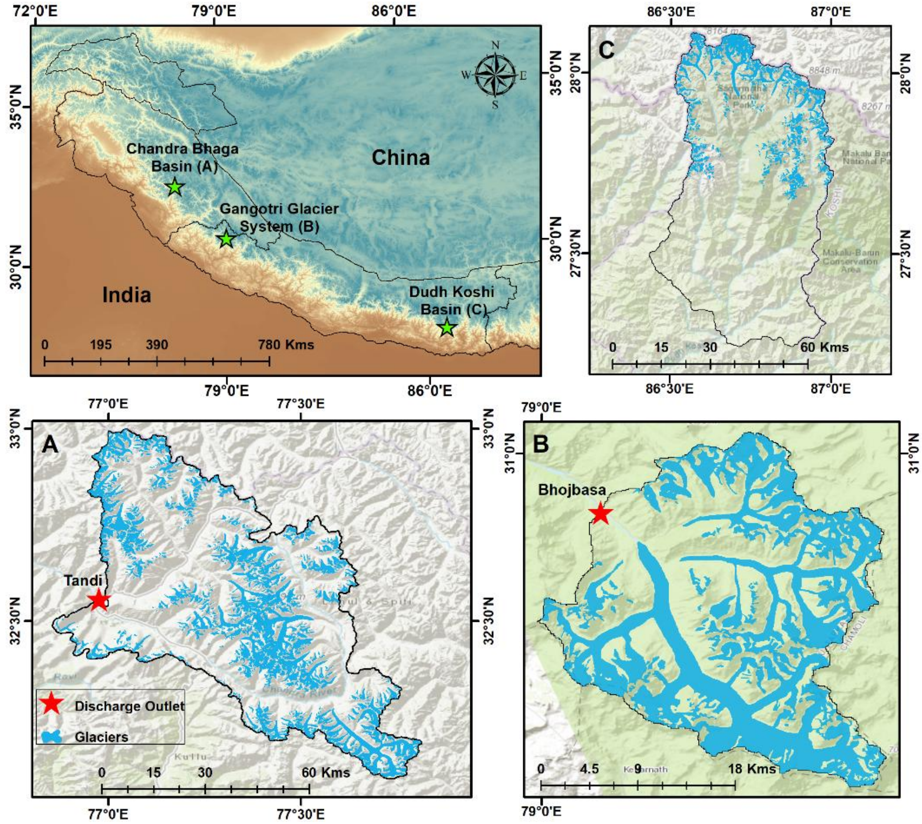

Figure 1.1 Geographic location of the study basins: (A) Chandra-Bhaga Basin in the western Himalaya, (B) Gangotri Glacier System in the central Himalaya, and (C) Dudh Koshi Basin in the central Himalaya. Glacier extents are indicated in blue, and red stars denote discharge measurement stations.

## 1.3 Climate change and observed cryospheric changes

Over recent decades, the HK region has experienced significant climatic changes, most notably warming trends that have exceeded the global average in many locations (Krishnan et al., 2019; Pörtner et al., 2022). In-situ records and reanalysis data indicate that mean annual temperatures have increased across much of the region, with particularly strong warming at higher elevations (Pepin et al., 2015). The latest IPCC Sixth Assessment Report (2022) projects that global warming will reach or exceed 1.5°C above pre-industrial levels within the next two decades, with pronounced impacts on high mountain cryospheric systems (Pörtner et al., 2022).

Himalayan glaciers have been losing mass at an accelerating rate (Brun et al., 2017; Azam et al., 2018; Maurer et al., 2019; Shean et al., 2020). Remote sensing studies have shown widespread retreat of glacier terminus and thinning of ice, though with notable spatial variability. The Karakoram Range, for instance, has exhibited a relatively stable or slightly positive mass balance in recent decades, a phenomenon known as the “Karakoram Anomaly” (Hewitt, 2005; Gardelle et al., 2013). However, there are emerging evidence of glacier wastage in the Karakoram over the recent decades (Hugonnet et al., 2021). Seasonal snow cover has also declined in duration and extent in many parts of the HK region, with earlier onset of melt and shifts in the timing of peak runoff (Brown et al., 2010; Bormann et al., 2018).

These cryospheric changes have direct hydrological consequences. In the short term, increased glacier melt can enhance river flows during the melt season, but in the longer term, as glaciers lose mass, their meltwater contribution is expected to decline (Kraaijenbrink et al., 2017; Pritchard, 2019). This shift could have profound impacts on water availability during critical agricultural periods and may intensify water scarcity in already vulnerable downstream regions. Furthermore, changes in snowmelt timing can affect seasonal water storage, hydropower scheduling, and flood risk management (Lutz et al., 2014).

The combined effects of glacier retreat, snow cover decline, and altered precipitation patterns are likely to change the seasonality of river flows, with potential implications for both water security and hazard occurrence, including floods, landslides, and glacial lake outburst floods (GLOFs) (Harrison et al., 2018; Veh et al., 2020; Sattar et al., 2025). Understanding these changes and their hydrological consequences requires robust monitoring and modelling tools capable of capturing the complex interplay between climate, cryosphere, and hydrology.

## 1.4 Hydrological modelling in HK

Hydrological modelling is a key tool for estimating the relative contributions of snowmelt, glacier melt, baseflow and rainfall-runoff to river discharge, particularly in high mountain regions where direct measurements are limited (Hock, 2003; Immerzeel et al., 2010; Ragettli and Pellicciotti, 2012). In such environments, models help bridge the gap between sparse observations and the need for continuous, long-term hydrological records. Two broad approaches are commonly applied for estimating the melt, viz. Physically-based energy-balance models and temperature-index (degree-day) models.

Physically based energy-balance models simulate melt processes by resolving the surface energy budget, incorporating inputs such as incoming and outgoing radiation, air temperature, humidity, wind speed, and the phase of precipitation (Oerlemans, 1992; Favier et al., 2004; Azam et al., 2014b; Srivastava and Azam, 2022a). These models can offer a physically consistent representation of melt dynamics but require extensive meteorological and glacier surface data, which are often unavailable in HK due to the scarcity of high-altitude observation networks (Vishwakarma et al., 2022). Temperature-index (degree-day) models take a simpler empirical approach, relating melt rates directly to air temperature through degree-day factors for snow and ice (Hock, 2003). Although they do not explicitly resolve the full energy balance, these models require fewer inputs and can be implemented using readily available datasets, including gridded meteorological products and remote sensing-derived snow cover information (Immerzeel et al., 2009; Tahir et al., 2011). This makes them particularly useful in regions where ground-based meteorological measurements are sparse (Hock, 2003; Azam et al., 2014).

In both approaches, model performance depends heavily on parameter calibration. When only discharge data are available for calibration, there is a risk of equifinality, where different parameter combinations can reproduce similar discharge patterns but imply different contributions from snow and glacier melt (Beven, 2016; Azam et al., 2021). Additionally, many studies calibrate parameters for a single basin without evaluating their applicability elsewhere, leaving uncertainty about whether these parameters can be transferred to other catchments with similar climatic or physiographic conditions. This lack of tested parameter transferability and model calibration with a limited dataset is the critical limitations for large-scale water resource assessments in glacierized regions.

## 1.5 Satellite-based monitoring of snowline altitude

Remote sensing has become crucial for monitoring glacier conditions across HK, enabling consistent and frequent observations over large and often inaccessible areas (Racoviteanu et al., 2008; Brun et al., 2017; Dehecq et al., 2019). Among the many glacier parameters that can be observed from space, the snowline altitude (SLA) is particularly important. SLA represents the boundary between snow-covered and snow-free area at a given time, and its highest position at the end of the ablation season ($SLA_{max}$) is often used as a proxy for the equilibrium line altitude (ELA), the elevation at which accumulation equals ablation (Braithwaite and Raper, 2009; Cuffey and Paterson, 2010). Since ELA is directly linked to the glacier mass balance, monitoring SLA provides a valuable means of assessing glacier health and detecting changes in response to climate variability (Braithwaite and Raper, 2009; Rabatel et al., 2013).

The use of SLA as an indicator has grown with the availability of high- to medium-resolution satellite imagery from sensors such as Landsat, Sentinel, SPOT, etc. (Racoviteanu et al., 2019; Liu et al., 2021). SLA mapping methods can be broadly grouped into manual, semi-automated, and automated approaches. Manual delineation involves expert visual interpretation of satellite images to draw the snowline, often with high accuracy when cloud-free images are available, but it is time-consuming and can be subjective (Rabatel et al., 2016). Semi-automated techniques typically use spectral band ratios such as near-infrared (NIR) to shortwave infrared (SWIR), to differentiate snow, ice and bare land, combined with thresholding methods to define the snowline (Racoviteanu et al., 2019). Automated approaches extend these methods to large datasets, sometimes incorporating additional information such as slope, aspect, and elevation to refine the classification (Naegeli et al., 2019; Loibl et al., 2025).

Recent developments in machine learning have made large-scale, long-term SLA monitoring more efficient, allowing for consistent mapping across extensive spatial and temporal domains (Prieur et al., 2022). Such datasets have multiple applications, including detecting long-term glacier change, supporting hydrological model calibration and validation, and analyzing glacier-climate interactions. However, despite its widespread adoption, the use of SLA as a proxy for ELA has not been comprehensively validated in HK. This limits the ability to fully assess the accuracy of SLA-derived ELA estimates and highlights the need for systematic evaluation against reliable field-based measurements.

## 1.6 Research gaps

Despite significant progress in understanding glacier hydrology in the HK region, important gaps remain that constrain the accuracy and applicability of current modelling and monitoring approaches. A key uncertainty arises from the limited evaluation of hydrological model parameter transferability between catchments. In many studies, parameters such as degree-day factors, runoff coefficients, temperature lapse rates, etc. are calibrated for a single basin and, in some cases, applied to other basins without thorough testing. Given the considerable variability in precipitation regimes, glacier characteristics, and topographic conditions across the region, such untested parameter application can introduce substantial biases into discharge simulations and meltwater estimates.

Another limitation concerns the reconstruction of long-term meltwater contributions. Most modelling efforts have been restricted to relatively short observational periods and often rely on single-variable calibration, typically discharge, which increases susceptibility to equifinality and reduces the robustness of process representation. Integrating multiple datasets within a multi-tier calibration framework offers a way to address these issues, yet such approaches remain rare, mainly due to the sparse data. Without multi-decadal reconstructions constrained by diverse observations, the temporal evolution of snow and glacier melt contributions and their relationship to climatic variability cannot be fully characterized.

In addition, the use of $SLA_{max}$ at the end-of-ablation season as a proxy for the ELA in HK remains insufficiently validated. While this relationship is well established for winter-accumulation glaciers, the summer-accumulation regime of the monsoon-dominated Himalaya introduces complexities such as simultaneous accumulation and ablation, episodic summer snowfall, persistent cloud cover, and post-monsoon accumulation. These factors can cause significant deviations between $SLA_{max}$ and the true ELA. Although advances in semi-automated SLA extraction methods have improved spatial and temporal coverage, their reliability in monsoon-dominated settings has not been systematically assessed against field-based ELA measurements. This gap limits the confidence with which SLA can be used for mass balance estimation, model calibration, and long-term monitoring in these regions.

Addressing these gaps requires an integrated approach that combines glacio-hydrological modelling, remote sensing analysis, and field validation. Such an approach can improve the accuracy and reliability of meltwater contribution estimates, enhance understanding of SLA-ELA relationships in complex climatic regimes and provide a stronger basis for assessing the impacts of climate change on HK water resources.

## 1.7 Objectives of the thesis

The main aim of this thesis is to improve the understanding of glacier hydrology and melt contributions in the Himalayan region through the integration of remote sensing, glaciohydrological modelling, and field validation. It focuses on three climatically distinct glacierized basins to explore meltwater contributions, model parameter transferability, and the SLA-ELA relationship. The specific objectives are:

1. To evaluate the transferability of snowmelt runoff model parameters in the Chandra-Bhaga basin,
2. To simulate long-term snow and glacier melt contributions in the Gangotri Glacier System,
3. To develop an improved method for snowline extraction, and
4. To examine the relationship between snowline altitude (SLA) and equilibrium line altitude (ELA).

## 1.8 Organisation of the thesis

### Chapter 1: Introduction

This chapter presents a brief overview of HK, climatic regimes across different glacierized regions, and challenges in modelling snow and glacier melt. It summarises the existing methods and highlights research gaps related to SLA estimation, SLA-ELA relationships, long-term melt contribution estimation, and model parameter transferability. The chapter concludes by defining the objectives of the thesis.

### Chapter 2: Literature review

This chapter provides a comprehensive review of the different glaciohydrological models used for estimating melt contributions, highlighting their advancements and limitations. It also identifies key methodological gaps in SLA estimation and the SLA-ELA relationship in the Himalaya.

### Chapter 3: Assessing model parameter transferability between the glacier and basin scale in the western Himalaya

The chapter assesses the transferability of SRM parameters from a data-rich glacier catchment (Chhota Shigri) to its basin (Chandra-Bhaga) in the western Himalaya. The SRM was calibrated for Chhota Shigri using field-constrained parameters and validated with observed discharge over 2010–2015. When these calibrated parameters were applied to the Chandra-Bhaga basin, significant overestimations in discharge were observed, indicating that SRM parameters are not directly scalable even within the same basin having similar climatic and physiographic settings. Sensitivity analysis further revealed that the runoff coefficient for snow and the degree-day factor are dominant controls on model output. This chapter highlights the importance of site-specific calibration and cautions against using parameter sets from reference catchments for other or more heterogeneous basins.

### Chapter 4: Snow and glacier melt contributions from the Gangotri Glacier System and their climatic controls

Chapter 4 presents long-term glaciohydrological modelling of Gangotri Glacier System (GGS) using the SPHY model, forced with bias-corrected IMDAA reanalysis data over 1980–2020. The model was calibrated using in-situ discharge and available geodetic mass balance and validated against improved MODIS snow cover data. Results show that snowmelt is the dominant contributor to total discharge (64%), followed by glacier melt (21%), rainfall-runoff (11%) and baseflow (4%). Statistical analysis identifies summer precipitation and winter temperature as key climatic drivers of runoff variability. This chapter underscores the value of multi-constraint calibration and remote sensing inputs in long-term melt modelling for Himalayan basins.

### Chapter 5: Improved snowline extraction method

This chapter presents an improved methodology for estimating glacier SLA from optical satellite imagery. The method integrates a semi-automated band ratio-based SLA extraction routine with Otsu method and a robust post-processing filtering scheme to address challenges posed by cloud cover, cast shadows, steep slopes, and temporary snow. The processing framework is implemented in Python and validated using high-resolution Planet and Venµs imagery. This chapter contributes to a reproducible and scalable approach for generating sub-monthly SLA time series suitable for climatological and glaciological analyses in data-scarce, complex mountain environments.

### Chapter 6: SLA-ELA relationship in the monsoon-dominated region

Chapter 6 investigates the relationship between remotely sensed end-of-ablation season $SLA_{max}$ and field-based ELA in the monsoon-dominated central Himalaya. Using a multi-year SLA dataset generated through the improved extraction method in Chapter 5, this chapter evaluates the validity of using $SLA_{max}$ as a proxy for ELA on Mera Glacier, where longest field observations are available in the central Himalaya. The analysis considers the influence of surface processes such as sublimation, wind redistribution, and temporary snow cover, which complicate SLA fluctuations and challenge the SLA-ELA assumption. This chapter highlights the limitations of applying standard SLA-based ELA estimation methods in regions with complex monsoon-driven accumulation and ablation patterns.

### Chapter 7: Conclusions and future work

The thesis concludes with a summary of the key findings and a discussion on the potential directions for future research.

# Chapter 2
# Literature review

## 2.1 Glaciohydrological modelling in HK

Glaciohydrological modelling in the HK region has advanced substantially over the past two decades, motivated by the need to quantify meltwater contributions to river systems and assess their response to climate change. Numerous studies indicate that snow and glacier melt constitute a substantial fraction of annual runoff in many HK basins, particularly those with high glacierized area, such as the Indus basin (Bookhagen and Burbank, 2010; Lutz et al., 2014; Azam et al., 2021). Model projections consistently suggest that rising temperatures will enhance meltwater yields in the near term, after which melt contributions will decline as glacier storage diminishes (Lutz et al., 2014; Huss and Hock, 2018). However, the magnitude and timing of these changes vary considerably between basins and modelling frameworks, reflecting large uncertainties in both climatic forcing and process representation (Ragettli et al., 2013; Pritchard, 2019). A persistent challenge in the HK region is accurately partitioning runoff into rainfall-runoff, snowmelt, and glacier melt components, as observational data remain sparse and heterogeneous across catchments (Armstrong et al., 2019; Azam et al., 2021; Vishwakarma et al., 2022).

The modelling approaches applied in HK span from empirical temperature-index (degree-day) models to physically based energy-balance models, as well as hybrid and distributed frameworks that integrate multiple processes. For melt calculations, temperature-index approach are the most widely used due to their fewer input requirements and their adaptability to basins with limited meteorological observations in HK (Hock, 2003;

Immerzeel et al., 2009; Butt and Bilal, 2011; Panday et al., 2014; Azam et al., 2019). These models relate melt rates to air temperature using degree-day factors for snow and ice and can be coupled with satellite-derived snow cover to constrain spatial melt patterns (Tahir et al., 2011; Aggarwal et al., 2014). While effective in simulating seasonal flow in many HK catchments, their performance is sensitive to the estimation of model parameters, which vary with elevation, debris cover, and season (Hock, 2003; Zhang et al., 2006; Heynen et al., 2013). Physically based energy-balance approach resolves the surface energy budget and can capture additional processes such as sublimation, wind redistribution, and debris-cover effects (Reid et al., 2012; Shea et al., 2015; Buri et al., 2016; Miles et al., 2016), but their application in the HK is constrained by the scarcity of high-resolution meteorological data and the complexity of calibration (Ragettli et al., 2013; Vishwakarma et al., 2022).

Advances in distributed and hybrid modelling have improved the spatial variability of simulations by integrating topographic variability, glacier hypsometry, and temporally varying snow cover (Immerzeel et al., 2013; Lutz et al., 2014; Khanal et al., 2021). Latest models combine temperature-index melt formulations with distributed hydrological structures that also account for seasonal snowpack evolution and glacier dynamics (Terink et al., 2015). The integration of high-resolution remote sensing products, including improved MODIS snow cover (Muhammad and Thapa, 2020; Salim and Pandey, 2021) and geodetic glacier mass balance (Shean et al., 2020), into model forcing and calibration has improved process representation. Bias-corrected reanalysis datasets have also been increasingly adopted to address the lack of in-situ meteorological observations (Arora et al., 2024; Srivastava et al., 2024). However, uncertainties persist due to biases in gridded precipitation, which often underestimates high-altitude snowfall (Eeckman et al., 2017; Immerzeel et al., 2020), and due to equifinality, where different parameter combinations produce similar discharge outputs but divergent melt partitioning (Ragettli et al., 2013; Beven, 2016).

To address these limitations, recent studies have adopted multi-constraint calibration approaches, simultaneously tuning models against discharge, snow cover, and glacier mass balance observations (Azam et al., 2019; Singh et al., 2023; Srivastava et al., 2024; Arora et al., 2024). This has improved the accuracy of meltwater partitioning and reduced uncertainty. Ensemble modelling, incorporating multiple models and climate scenarios, has been used to quantify uncertainty ranges and identify robust trends (Lutz et al., 2014; Kraaijenbrink et al., 2017). Incorporating additional processes, such as the role of debris cover in insulating glacier ice (Vatsal et al., 2024) or the effect of snow/ice avalanching, can further enhance the efficiency of glaciohydrological models. The literatures show that progress in HK hydrological modelling will remain dependent on improved high-elevation monitoring networks, expanded benchmark glacier studies, and enhanced integration of remote sensing with physically consistent modelling frameworks (Azam et al., 2021; Vishwakarma et al., 2022).

## 2.2 Parameter transferability in hydrological models

Parameter transferability in glaciohydrological models has been a recurring necessity in the HK region due to the scarcity of long-term hydro-meteorological observations at high elevations (Hock, 2003; Nepal et al., 2023). In many modelling studies, key parameters such as degree-day factors, runoff coefficients, precipitation gradient, and temperature threshold for snow/rain partitioning are adopted from neighboring catchments or literature rather than calibrated locally (Singh and Jain, 2002; Butt and Bilal, 2011; Panday et al., 2014; Hayat et al., 2019). While this approach enables simulations in data-scarce basins, it introduces the risk that parameters optimized under one set of climatic, topographic, and glaciological conditions may not be valid elsewhere (Ragettli et al., 2013; Beven, 2016). The HK region exhibits substantial heterogeneity in glacier hypsometry, debris-cover extent, precipitation regime, and snow persistence (Maussion et al., 2014; Scherler et al., 2018; Garg et al., 2024), all of which can exert a huge impact on optimal parameter values. Consequently, such applications of parameters across basins may lead to substantial biases in simulated runoff and melt partitioning.

Climatic regime differences across HK present one of the most significant barriers to parameter transferability. Glacierized basins in the western part of HK, influenced predominantly by WDs, are snowmelt-dominated, whereas monsoon-fed eastern part are characterized by high-intensity summer rainfall and comparatively lower snowmelt contributions (Thayyen and Gergan, 2010). Temperature thresholds for snow-rain separation, precipitation gradient, and melt coefficients often differ significantly between these regimes, making inter-regime parameter transfer unreliable. Similarly, debris-cover variability exerts a strong control on melt rates (Zhang et al., 2006; Scherler et al., 2018). Parameters calibrated for clean-ice glaciers can substantially overestimate melt for debris-covered glaciers, and vice versa, unless debris effects are explicitly modelled (Buri et al., 2016; Miles et al., 2016).

The risks of parameter transfer are further compounded by equifinality, where multiple parameter sets yield similar discharge simulations but different internal process representations (Ragettli et al., 2013; Beven, 2016). This is particularly problematic for future projections, as parameter sets that reproduce present-day hydrographs may not be physically robust under altered climate forcing (Lutz et al., 2014; Kraaijenbrink et al., 2017). To reduce such uncertainties, recent HK studies have increasingly employed multi-criteria calibration approaches, simultaneously optimizing model performance against discharge, snow cover, and glacier mass balance data (Singh et al., 2023; Srivastava et al., 2024; Arora et al., 2024). Ensemble modelling across multiple basins has also been proposed as a means to identify parameter ranges that perform satisfactorily across varied physiographic and climatic settings, thereby improving transferability while quantifying uncertainty (Lutz et al., 2014).

In summary, while parameter transferability offers a practical approach for ungauged HK basins, its success is highly dependent on various factors. Evidence suggests that parameter transfer may be reliable when basins are physically and climatically similar, and when uncertainties are explicitly quantified. However, the heterogeneity of the HK region in terms of glacier characteristics, debris cover, and climatic regime substantially limits the general applicability of parameter sets. Basin-specific calibration, informed by multi-source observations and sensitivity analysis, remains the preferred approach for robust glaciohydrological simulations in HK.

## 2.3 Quantifying snow and glacier melt contributions

Quantifying the relative contributions of snowmelt, glacier melt, baseflow and rainfall-runoff to river discharge is very important in glaciohydrological research in HK (Hock, 2003; Bolch et al., 2019; Azam et al., 2021). These estimates are essential for understanding seasonal water availability (Immerzeel et al., 2010; Lutz et al., 2014), managing water resources in downstream regions (Pritchard, 2019; Nepal et al., 2023), and anticipating the impacts of climate change on river flow (Kraaijenbrink et al., 2017; Khanal et al., 2021). A variety of approaches ranging from model-based simulations to remote sensing assimilation and tracer-based hydrograph separation have been applied across the region (Singh and Jain, 2002; Immerzeel et al., 2009; Maurya et al., 2011; Andermann et al., 2012; Brun et al., 2017; Azam et al., 2019). Reported contributions vary substantially between basins, reflecting differences in climatic regime, glacier extent, and catchment hypsometry (Thayyen and Gergan, 2010; Srivastava and Azam, 2022b), as well as variations in datasets, model structures, and calibration methods (Ragettli et al., 2013; Beven, 2016).

In the Upper Indus Basin, combined snow and glacier melt contributions are estimated as 62–72% of annual discharge (Fowler and Archer, 2005; Lutz et al., 2014; Maussion et al., 2014), with glacier melt alone contributing ~21–40% (Fowler and Archer, 2005; Lutz et al., 2014). Glacier-fed tributaries such as the Hunza River can exceed 60‒92% meltwater during peak summer flows (Shrestha et al., 2015; Shrestha and Nepal, 2019). In contrast, the upper Ganges and Brahmaputra basins, dominated by monsoon rainfall, show annual meltwater contributions of only 10–20% (Lutz et al., 2014). Central Himalayan basins such as the Dudh Koshi are snowmelt-dominated, with total melt contributions of ~30–35% annually (Nepal et al., 2014; Savéan et al., 2015). Smaller glacierized catchments in the western Himalaya, such as the Chandra-Bhaga, have roughly equal snow and glacier melt contributions, totalling around half of annual runoff (Srivastava et al., 2024). In general, meltwater dominates in the sub-basins of the western Himalaya and Karakoram (Bookhagen and Burbank, 2010; Lutz et al., 2014) but plays a smaller role in the monsoon-dominated central and eastern Himalaya (Nepal et al., 2014; Savéan et al., 2015).

Despite these general patterns, absolute estimates often differ noticeably for the same basin or catchment, such as Langtang valley in the central Himalaya that showed meltwater contributions ranging from 30 to 90% from different approaches (Azam et al., 2021). Discrepancies arise from differences in input datasets such as precipitation products, glacier inventories (Bookhagen and Burbank, 2010; Immerzeel et al., 2010), calibration strategies, and definitions of "glacier melt" (Lutz et al., 2014; Kraaijenbrink et al., 2017). Some studies define glacier melt strictly as ice melt, while others include seasonal snow on glaciers, leading to higher apparent contributions (Reid et al., 2012; Shea et al., 2015). High-altitude precipitation uncertainty is a major source of variability (Eeckman et al., 2017; Vishwakarma et al., 2022), with lower assumed precipitation resulting in higher inferred melt fractions (Ragettli et al., 2013; Kraaijenbrink et al., 2017). Spatial scale also matters; upper-basin studies report higher melt dependence than basin-wide analyses that include downstream rainfall-fed tributaries (Bookhagen and Burbank, 2010; Lutz et al., 2014). Uncertainty is compounded by sparse high-elevation observations (Bolch et al., 2019; Vishwakarma et al., 2022), the dependence on extrapolated climate data (Kraaijenbrink et al., 2017; Huss and Hock, 2018), and parameter equifinality (Ragettli et al., 2013; Beven, 2016). Tracer-based methods can help separate melt sources but often face end-member overlap between snow and ice melt (Maurya et al., 2011; Müller et al., 2025). Reducing variability in melt estimates requires improved quantification of high-altitude precipitation and consistent definitions of melt components. Standardised methodologies and harmonized datasets will enable more comparable and reliable assessments across HK basins.

## 2.4 Snowline estimation using remote sensing

Given the difficulty of conducting frequent in-situ observations at high altitudes, remote sensing-based SLA mapping serves as a proxy for the ELA and helps to assess spatial and temporal variations in glacier response to climate forcing. Early efforts primarily relied on manual delineation from satellite imagery such as Landsat, Sentinel, SPOT, etc., where visual interpretation enabled tracing of the transient snowline on glaciers, particularly during the end of the ablation season when the contrast between snow and ice is usually high (Pelto, 2011; Mernild et al., 2013; Rabatel et al., 2016; Tawde et al., 2016; Barandun et al., 2018; Chandrasekharan et al., 2018). While manually derived snowlines remain valuable for detailed studies or for validation, they are constrained by operator bias and limited scalability across large regions or multiple time steps (Rabatel et al., 2013).

Subsequent studies increasingly adopted semi-automated approaches based on spectral thresholding, particularly the normalized difference snow index (NDSI), to classify snow pixels and infer the snowline as the upper limit of exposed glacier ice (Rastner et al., 2015; Racoviteanu et al., 2019; Barandun et al., 2021; Liu et al., 2021). The NDSI method exploits the spectral contrast between snow and non-snow surfaces in the visible and shortwave infrared bands to enable robust snow classification. These methods have been widely applied to medium-resolution imagery from MODIS, Landsat, and Sentinel and were capable of deriving snowline elevation for numerous glaciers. Often, a fixed threshold value is used to classify snow cover (Rastner et al., 2015; Racoviteanu et al., 2019). However, some workflows determine the threshold adaptively by employing Otsu algorithm on a near-infrared band histogram to automatically separate snow from ice (Rastner et al., 2019; Liu et al., 2021). The Otsu method is a histogram-based thresholding approach that objectively separates classes by maximizing inter-class variance, allowing image-specific threshold selection without manual tuning. More sophisticated multi-step classification schemes based on surface albedo have also been introduced to better delineate the snowline (Lei et al., 2012; Naegeli et al., 2019; Barandun et al., 2021). To improve scalability and consistency, recent efforts make use of Google Earth Engine for regional-scale SLA mapping (Liu et al., 2021; Loibl et al., 2025) and apply machine-learning algorithms to refine snow/ice classification under diverse conditions (Prieur et al., 2022). To improve the reliability of results, various post-processing filters are introduced. For example, Loibl et al. (2025) excluded scenes based on percent cloud cover and standard deviation of SLA. Other studies applied slope and elevation thresholds to remove false snowline pixels in steep terrain (Girona-Mata et al., 2019; Racoviteanu et al., 2019). Additionally, some workflows filtered the snowline based on the percent snow cover area in each elevation zone (Rastner et al., 2019; Prieur et al., 2022; Loibl et al., 2025). Another strategy to minimize topographic bias is to restrict snowline tracing to the glacier's central flowline, rather than across its entire width, thereby reducing the influence of aspect and shading variations (Rabatel et al., 2017; Davaze et al., 2020).

Despite these advancements, continuous sub-monthly SLA monitoring in high-mountain environments remains difficult because complex topography (steep slopes, cast shadows, debris-covered or superimposed ice, crevasses) and frequent cloud cover—especially during the monsoon season—often confound automated classification (Racoviteanu et al., 2019; Rastner et al., 2019). Data discontinuities continue to restrict high-frequency, glacier-scale SLA monitoring across the HK region. The lack of standardization in SLA extraction procedures also complicates inter-study comparisons and trend detection. Nonetheless, integrating multi-sensor data (optical, SAR, and thermal), employing ensemble approaches, and increasing ground-truth datasets for training and validation hold promise for improving SLA estimates across spatial and temporal scales. Continued methodological refinement, particularly in semi-automated and machine learning-based approaches, is critical to advance the operational use of SLA tracking for hydrological and climate assessments in the HK region.

## 2.5 SLA-ELA relationship

The relationship between SLA and ELA has been investigated across glacierized regions, and its applicability in the HK region has gained increasing attention due to the scarcity of in-situ mass balance observations and the region's complex climatic and topographic settings. SLA, particularly during the late ablation season, is commonly employed as a remote sensing proxy for ELA under the assumption that it approximates the altitude where annual accumulation equals ablation (Rabatel et al., 2012). This simplification supports numerous efforts to infer mass balance and climatic sensitivity from satellite imagery. However, this approach is complicated in HK, where monsoon dynamics and frequent summer snowfall introduce spatial and temporal heterogeneity in snow accumulation and melt (Wagnon et al., 2013; Brun et al., 2015). Wagnon et al. (2013) observed that under extreme melt conditions, the ELA can exceed the glacier's highest elevation, rendering SLA-based ELA estimates misleading. Moreover, glacier-specific topographic factors such as slope and aspect can also result in localized SLA-ELA discrepancies, underscoring the importance of spatial filtering in remote sensing analyses.

Alternative statistical and empirical approaches have been proposed to improve SLA-ELA inference. Oien et al. (2022) assessed the performance of the accumulation-area ratio (AAR) and area-altitude balance ratio (AABR) methods applied to satellite-derived snowlines and found glacier-specific variability in their performance. Braithwaite and Raper (2009) and Owen and Benn (2005) suggested that using mean SLA over multiple years may offer a reasonable approximation of long-term ELA; however, they caution that this relationship can be sensitive to outlier years and variable accumulation regimes. Pelto (2011) further proposed that SLA migration rates during the melt season may provide a more dynamic and sensitive indicator of glacier-climate interactions than absolute snowline positions.

In summary, while SLA remains a feasible remote sensing-based indicator for estimating ELA and assessing glacier health in data-scarce regions like HK, its utility is highly context-dependent. The presence of complex monsoonal influence and topographic effects introduces biases that limit the validity of SLA-ELA relationships across the region. Methodological improvements, including topographic corrections, integration of snow persistence metrics, and cross-validation with mass balance and ELA in-situ observations, are essential to enhance the accuracy and reliability of SLA-derived ELA estimates in HK.

# Chapter 3

# Assessing model parameter transferability between the glacier and basin scale in the western Himalaya

## 3.1 Introduction

The Himalaya-Karakoram (HK) Range, also known as the Water Tower of Asia, contains a huge storage of water in the form of a large number of glaciers, snow cover, and permafrost. The HK Range contributes to the discharge of major river systems like the Ganga, Indus, and Brahmaputra in the form of snow and glacier melt (Immerzeel et al., 2020; Azam et al., 2021). Due to global and regional warming (Banerjee and Azam, 2016; Pörtner et al., 2022), glaciers in the Himalaya have been losing their mass at an accelerating rate since 2000 (Brun et al., 2017; Azam et al., 2018; Bolch et al., 2019; Maurer et al., 2019; Shean et al., 2020), which resulted in the increased discharge volume in these rivers (Lutz et al., 2014; Azam et al., 2021). The latest IPCC 6th assessment report stated that global warming will reach or exceed 1.5 ºC above the pre-industrial level in the next two decades (Pörtner et al., 2022). This temperature rise would result in decreasing snow cover, retreating glaciers, changes in river seasonality, and higher river discharge, which can be the main cause of different hazards like floods, landslides, etc. The discharge from snow-covered and glacierized catchments mainly involves contributions from snowmelt, glacier melt, baseflow, and rainfall-runoff. The snowmelt contribution to the river discharge is large in the Indus Basin (Karakoram and western Himalaya) because it receives a major portion of annual precipitation in the form of snow during winter that provides snowmelt discharge during summer (Azam et al., 2021). Conversely, in the Ganga and Brahmaputra basins (central and eastern Himalaya), the total discharge is dominated by the monsoonal rains as these basins receive the maximum precipitation from Indian Summer Monsoon (ISM) during summer. A study by (Bookhagen and Burbank, 2010) found a pronounced contribution of snowmelt to total discharge in the Karakoram and western Himalaya as compared to the central and eastern Himalaya. Since snowmelt plays a significant role in the discharge of Himalayan rivers, it must be accurately estimated using suitable methods and modelling techniques with appropriate model parameters and inputs.

Snowmelt runoff modelling has usually been done using temperature-index or energy balance models. Whereas the temperature-index models are simple and need fewer input data, the energy balance models are sophisticated and require plenty of meteorological data (Hock, 2003; Shea et al., 2015; Srivastava and Azam, 2022b). In the Himalayan region, due to the adverse situations induced by steep terrain, harsh climatic conditions, and remote access to the high-altitude regions, monitoring of meteorological data is very difficult; hence, the application of energy balance models is very challenging. The temperature-index models follow the degree-day approach to estimate the melt (Hock, 2003). The snowmelt runoff model (SRM), based on the degree-day approach, is developed to simulate the daily discharge under the changing climate from mountain basins where the snowmelt plays an important role (Martinec et al., 2007). SRM has widely been applied and tested on more than 100 basins of varying areas by different agencies (Martinec et al., 2007) to simulate and forecast the daily discharge from the glacierized catchments in different mountain ranges. This model uses long-term meteorological and remotely sensed snow cover data as basic input for generating discharge at the outlet (Martinec et al., 2007; Tahir et al., 2011).

The SRM has also been applied in several studies for simulating daily discharge in the HK range (Immerzeel et al., 2009; Bookhagen and Burbank, 2010; Jain et al., 2010; Tahir et al., 2011; Panday et al., 2014). As snow cover area (SCA) has also been included in SRM for the simulation of daily discharge hence it can also be applied to study the impact of reduced snow cover on discharge (Immerzeel et al., 2009). For the regions where only the gridded precipitation and temperature datasets are available, SRM performs as an efficient tool for snowmelt runoff modelling. Several studies tested this model with gridded datasets of temperature and precipitation like APHRODITE, TRMM, etc. (Immerzeel et al., 2009; Bookhagen and Burbank, 2010; Tahir et al., 2011; Zhang et al., 2014). Jain et al. (2010) applied SRM in the Sutlej Basin (western Himalaya) and found that seasonally varied temperature lapse rate increases the efficiency of the SRM, which shows the model is sensitive to the temperature lapse rate parameter. Applying the SRM in the Hunza River Basin (Karakoram), Tahir et al. (2011) demonstrated that SRM, using SCA as an input, is relatively less sensitive to the precipitation input; hence, its efficiency is not hampered in high-altitude catchments where the precipitation measurements contain large uncertainties. The high accuracy of SRM runoff simulation in the Astore River Basin part of the Indus Basin showed that the SRM is suitable for the runoff forecast and water resource management (Butt and Bilal, 2011). Tahir et al. (2019) applied SRM in the Shyok River Basin (Karakoram) to assess the snowmelt discharge under climate change scenarios and found that the SRM is an efficient tool to simulate the snowmelt discharge in data-scarce regions. SRM was also applied for future runoff simulation under different climate scenarios in the Astore Basin (Karakoram) and Hunza Basin (western Himalaya) and resulted in an effective tool for runoff forecast (Hayat et al., 2019). Different SCA products from MODIS, like MOD10A2 and MOD10C2, have been widely used and shown to perform well in several studies (Immerzeel et al., 2009; Bookhagen and Burbank, 2010; Tahir et al., 2011; Panday et al., 2014; Zhang et al., 2014; Haq et al., 2020, 2021).

Available studies suggested that the SRM is a simple and efficient model which can be applied in high-altitude catchments due to its flexibility with the gridded dataset, and SCA integration in the modelling scheme. Further, SRM requires a set of parameters that depends on the catchment area characteristics and the climatic conditions in the catchment. Due to the lack of information about the observed parameters in the Himalayan catchments, these parameters are being calibrated with the observed discharge or have been taken from previous studies (Butt and Bilal, 2011; Tahir et al., 2011; Panday et al., 2014; Hayat et al., 2019). But since model parameters play a vital role in model calibration to constrain the model from overfitting, they require special attention in snowmelt runoff modelling.

In the present study, SRM was applied to reconstruct the daily discharge from a small catchment of Chhota Shigri Glacier (34.7 km$^2$; volume of Chhota Shigri glacier is 1.69 km$^2$ (Haq et al., 2021)) and Chandra-Bhaga Basin (including Chhota Shigri Catchment) having a large area (~4108 km$^2$) up to the point of confluence of Chandra and Bhaga rivers at Tandi village in Himachal Pradesh. The daily discharge was simulated for the period of 2003−2018 for both the study regions: Chhota Shigri Catchment and Chandra-Bhaga Basin. Small and large scales were selected to check the performance of SRM for snowmelt runoff modelling at the catchment scale and basin-scale, having distinct characteristics. The main objectives for this study are (a) to reconstruct the daily discharge separately for the Chhota Shigri Catchment and Chandra-Bhaga Basin and assess the discharge pattern characteristics, (b) to analyse the model sensitivity to all input parameters in SRM, and (c) to assess the transferability of model parameters calibrated at Chhota Shigri Catchment to simulate the discharge in the Chandra-Bhaga Basin.

## 3.2 Study area and datasets

### 3.2.1 Topographical and climatic characteristics of the study area

Chandra-Bhaga Basin is a part of the Indus River system located in the western Himalaya, it is formed by the confluence of rivers Chandra and Bhaga at Tandi village in the Lahaul-Spiti Valley, Himachal Pradesh, India (Figure 3.1A, B, C). It covers an area of ~4108 km$^2$ up to Tandi, which lies between the elevation range from 2846 m a.s.l. to 6370 m a.s.l. (Figure 3.2B). This basin is having 25% glacierized area as per the GAMDAM inventory (Sakai, 2019). The Chhota Shigri Catchment, situated in the same basin, covers an area of 34.7 km$^2$, having a discharge site at 3840 m a.s.l. downstream of the Chhota Shigri Glacier terminus (Azam et al., 2016) (Figure 3.1D). Chhota Shigri Catchment lies between the elevation range of 3840 to 6263 m a.s.l. and contains 47% of the glacierized area (Figure 3.2A). The Chandra-Bhaga Basin is selected because this basin, as well as its Chhota Shigri Glacier Catchment, has been investigated for glaciohydrology by several studies (Azam et al., 2019; Mandal et al., 2020; Azam, 2021; Singh et al., 2021a; Azam et al., 2021; Gaddam et al., 2022; Srivastava et al., 2022) and also, the Chhota Shigri Glacier Catchment is having the longest series of observed meteorological data and discharge measurements that were available for the present study (Azam, 2021).

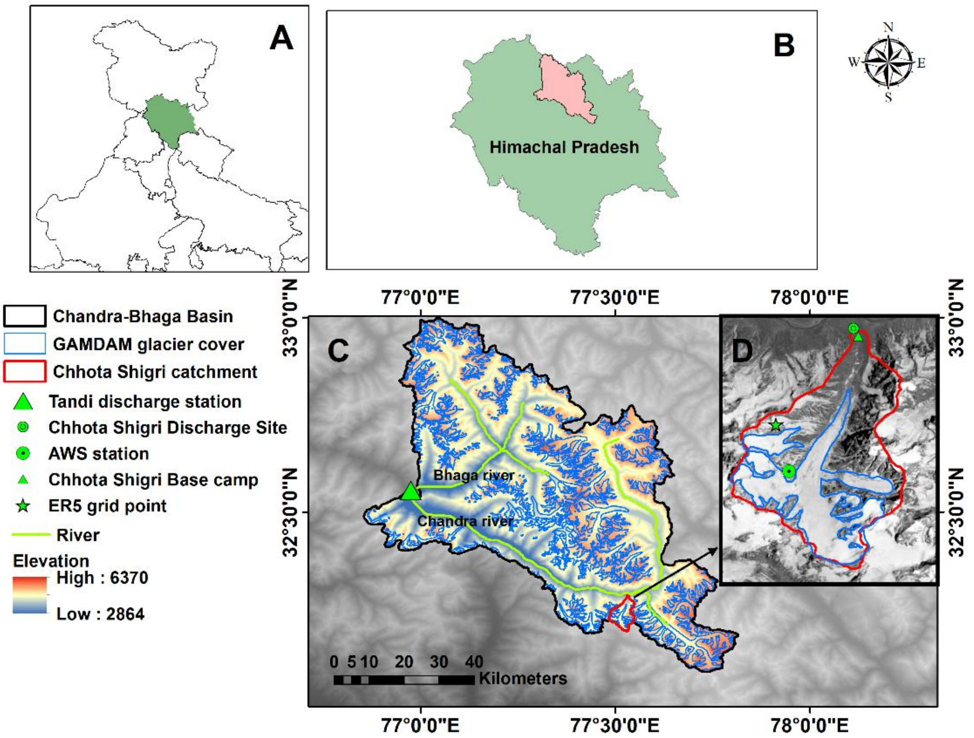

Figure 3.1 Location map of Chandra-Bhaga Basin (A–C), Basin boundary (black) with Tandi discharge site (green), river (green) and GAMDAM glacier cover (blue). Inset is the map of Chhota Shigri Catchment (D) with the catchment outline (red), Chhota Shigri Glacier (blue), and location of AWS station, discharge site, Chhota Shigri base camp, and ERA5 grid point (green symbols).

The climate of the Chandra-Bhaga Basin is governed by two weather systems: ISM and WDs (Dimri et al., 2015, 2016); however, 67% of the precipitation (Mandal et al., 2020) comes in the form of snow during winter months from WDs (Pratap et al., 2019; Singh et al., 2019; Mandal et al., 2020; Laha et al., 2021). The study region receives maximum precipitation in February and March from WDs (Mandal et al., 2020). Major discharge contribution in this basin is governed by the seasonal snow and glacier melt from major glaciers like Bara Shigri, Samudra Tapu, Sutri Dhaka, Batal, Chhota Shigri, and Hamtah, which are losing their mass over the last few decades (Singh et al., 2019; Mandal et al., 2020; Vishwakarma et al., 2022). In the Chhota Shigri Catchment, the discharge is dominated by snowmelt having around 69% contribution to the total discharge (Srivastava and Azam, 2022b). The maximum discharge in the Chhota Shigri Catchment occurs in July–August, corresponding to the maximum temperature (Mandal et al., 2020).

## 3.2.2 Datasets

### 3.2.2.1 DEM data and elevation zones

For snowmelt runoff modelling Cartosat Digital Elevation Model (DEM) having 30 m resolution was downloaded from the Bhuvan portal (https://bhuvan-app3.nrsc.gov.in) and extracted separately for both, the catchment and basin. The Chhota Shigri Catchment was divided into three 700 m interval elevation zones and the Chandra-Bhaga Basin was divided into sixteen 200 m interval elevation zones and their mean elevation and zone area were extracted using the digital elevation model (Table 3.1, Figure 3.2). The Chandra-Bhaga Basin was divided into the maximum possible number of elevation zones in SRM (WinSRM), but a higher elevation difference was used in the Chhota Shigri Catchment because the zonal areas were too small with the same elevation difference as the Chandra-Bhaga Basin.

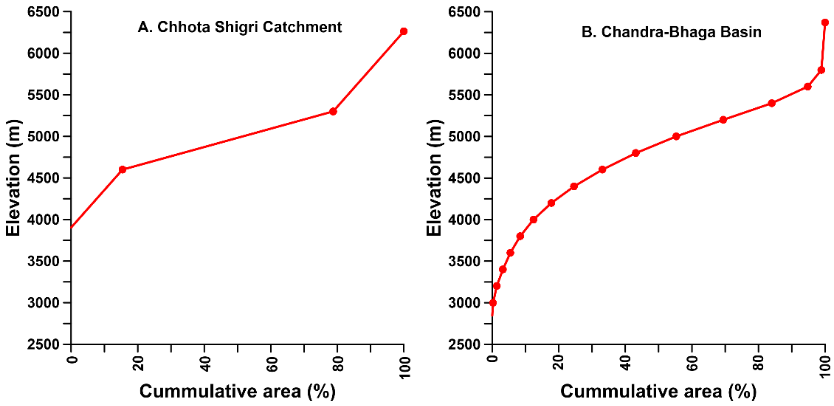

Figure 3.2 Hypsometry curve for Chhota Shigri Catchment (A) and Chandra-Bhaga Basin (B) showing the area distribution over the different elevations. Points represent the maximum elevations for each zone and cumulative percentage area.

#### 3.2.2.2 Meteorological data, discharge data and bias correction

Reanalysis product ERA5 precipitation and temperature data at resolution 0.25º x 0.25º were downloaded (https://cds.climate.copernicus.eu) at the nearest ERA5 grid point to the automatic weather station (AWS) at 4863 m a.s.l. in the Chhota Shigri Catchment (Figure 3.1D). ERA5 reanalysis data is available since 1950. For this study, the ERA5 temperature and precipitation data were bias-corrected using the field observations from the Chhota Shigri Catchment. The in-situ precipitation data was available from the Chhota Shigri base camp (3850 m a.s.l.) over 2012−2020 from an automatic precipitation gauge (Geonor T-200B) and the temperature data was available from the AWS (Campbell CR1000 data logger; details can be found in (Mandal et al., 2020) (4863 m a.s.l.) in the Chhota Shigri Catchment over 2009−2019 (Azam et al., 2016; Mandal et al., 2020) (Figure 3.1D). For the bias correction of temperature data, a linear regression equation was developed between the daily raw ERA5 temperature and the observed temperature, whereas monthly scale factors were used to bias correct the raw ERA5 precipitation series. The ERA5 bias-corrected data was used for snowmelt runoff modelling in the Chhota Shigri Catchment as well as Chandra-Bhaga Basin.

Table 3.1 Characteristics of different zones used in SRM for Chhota Shigri Catchment and Chandra-Bhaga Basin

| Zone | Elevation range (m) | Mean elevation (m) | Area (km$^2$) | Area (%) |
|---|---|---|---|---|
| | | **Chhota Shigri Catchment** | | |
| **1** | 3840–4600 | 4328 | 5.4 | 15.7 |
| **2** | 4600–5300 | 4981 | 21.7 | 62.6 |
| **3** | 5300–6263 | 5673 | 7.5 | 21.7 |
| | | | 34.7 | 100 |
| | | **Chandra-Bhaga Basin** | | |
| **1** | 2846–3000 | 2943 | 11.3 | 0.3 |
| **2** | 3000–3200 | 3107 | 44.0 | 1.1 |
| **3** | 3200–3400 | 3304 | 75.9 | 1.8 |
| **4** | 3400–3600 | 3506 | 91.8 | 2.2 |
| **5** | 3600–3800 | 3706 | 121.7 | 3.0 |
| **6** | 3800–4000 | 3906 | 164.2 | 4.0 |
| **7** | 4000–4200 | 4107 | 221.6 | 5.4 |
| **8** | 4200–4400 | 4304 | 280.0 | 6.8 |
| **9** | 4400–4600 | 4504 | 347.6 | 8.5 |
| **10** | 4600–4800 | 4705 | 415.2 | 10.1 |
| **11** | 4800–5000 | 4904 | 497.6 | 12.1 |
| **12** | 5000–5200 | 5102 | 581.1 | 14.1 |
| **13** | 5200–5400 | 5298 | 599.6 | 14.6 |
| **14** | 5400–5600 | 5489 | 443.4 | 10.8 |
| **15** | 5600–5800 | 5682 | 168.3 | 4.1 |
| **16** | 5800–6370 | 5985 | 44.4 | 1.1 |
| | | | 4107.5 | 100 |

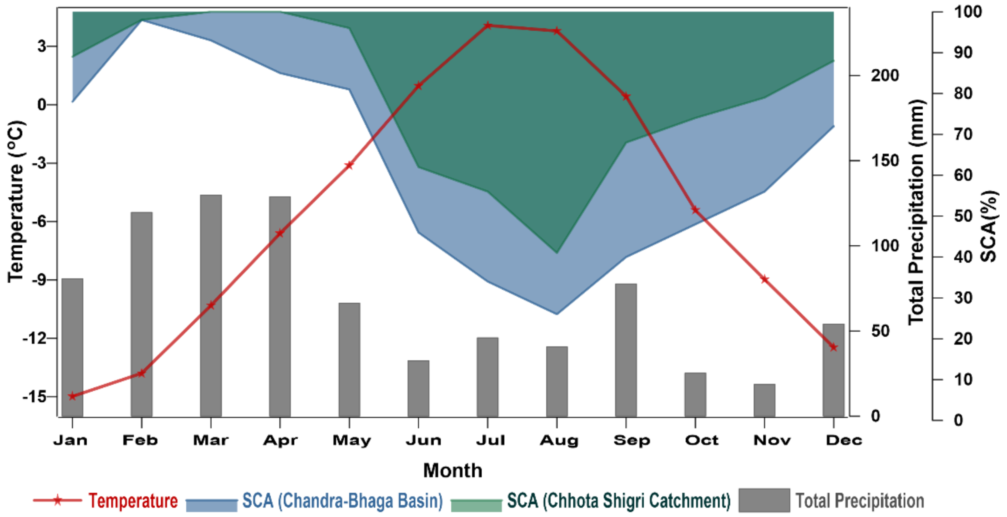

Figure 3.3 Monthly variation of model variables ERA5 bias-corrected (temperature, precipitation) and SCA for Chhota Shigri Catchment and Chandra-Bhaga Basin over 2003–2018.

The ERA5 bias-corrected mean annual temperature at the nearest ERA5 grid point was −5.5 ºC over 2003–2018, with the maximum mean monthly and minimum mean monthly temperature of 4.1 ºC in July and −14.9 ºC in January. The mean monthly temperature for summer (May–September) was 1.2 ºC and for winter (January–April and October–December) it was −10.3 ºC (Figure 3.3). The ERA5 bias-corrected mean annual precipitation was 819.9 mm over 2003–2018, with maximum monthly precipitation of 129.7 mm in March and minimum monthly precipitation of 18 mm in November (Figure 3.3). The mean precipitation for summer and winter was 263.1 mm and 556.8 mm, respectively. The higher mean precipitation in winter shows that the major portion of the precipitation occurs in winter, as suggested by previous studies (Azam et al., 2014; Mandal et al., 2020).

The observed daily discharge data from Chhota Shigri Catchment at a gauging site (~3840m a.s.l.), ~2km downstream of the Chhota Shigri glacier terminus, is available for the summer months over 2010–2015 (Azam et al., 2019). The measurement of discharge was done using the velocity-area method. A graduated staff gauge for monitoring the water level, dipsticks for measuring the cross-sectional area, and a current meter for the measurement of velocity were used (Mandal et al., 2020). The daily discharge measurements for the Chandra-Bhaga Basin are available over 2004–2006 at a gauging site located at Tandi village. This gauging site is maintained by the Central Water Commission (CWC). For the measurement of discharge by CWC at this gauging site, the velocity-area method was used with a current meter for velocity, a rod and bamboo for depth measurement (http://cwc.gov.in/mco/discharge-observation).

### 3.2.2.3 Snow cover data

Snow cover data for the study area was available from an enhanced snow cover and glacier combined product MOYDGL06* at the 8-day interval for the period 2002–2018. This product is generated by reducing the overestimation caused by MODIS sensors and underestimation caused by cloud cover in MODIS snow cover products MOD10A2.006 (Terra) and MYD10A2.006 (Aqua) (Muhammad and Thapa, 2020). This product is freely available in tiff format and WGS1984 projection (https://doi.pangaea.de/10.1594/PANGAEA.901821). For this study, a total of 736 images were used between 2003–2018. The SCA for each elevation zone of the Chhota Shigri Catchment and Chandra-Bhaga Basin was extracted for each 8-day interval and linearly interpolated to get the daily values.

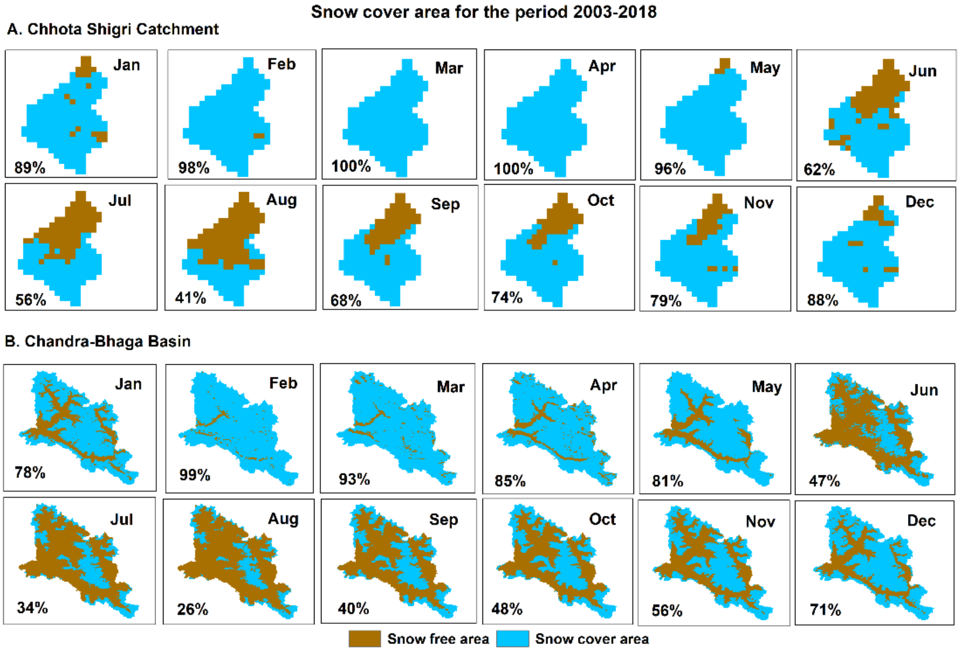

Figure 3.4 Mean monthly variation of SCA for Chhota Shigri Catchment (A) and Chandra-Bhaga Basin (B) over 2003–2018. Maps of both the areas are not on the same scale.

In the Chhota Shigri Catchment, SCA was least in August (41% of the catchment area) and started increasing from September, achieved maximum SCA in March–April (100% of the catchment area), and then started decreasing in May (Figure 3.3 and Figure 3.4A). Whereas in the Chandra-Bhaga Basin, the SCA started increasing in September and decreased from March. Chandra-Bhaga Basin showed the maximum SCA in February (99% of the basin area) and the minimum SCA in August (26% of the basin area) (Figure 3.3 and Figure 3.4B). The mean summer and winter SCA were 65% and 90%, respectively, in the Chhota Shigri Catchment, whereas for the Chandra-Bhaga Basin, it was 45% and 76% of the total basin area, respectively.

## 3.3 Methodology

### 3.3.1 Snowmelt runoff model

SRM (WinSRM version 1.12) is based on the degree-day approach and runs for a maximum of 366 days in one simulation. This model can be applied in two ways: basin-wide and zone-wise applications. For reconstructing the discharge in the Chhota Shigri Catchment and Chandra-Bhaga Basin, the model was run zone-wise to compute the catchment-wide or basin-wide discharge. The simulated discharge is a combination of snowmelt runoff and rainfall runoff superimposed on recession flow to transform all the components into daily discharge (Martinec et al., 2007). This model follows eq. 3.1 for the daily discharge computation from each zone:

$$Q_{n+1} = \left[C_{S_n} * a_n(T_n + \triangle T_n)S_n + C_{R_n}P_n\right]\frac{A * 10000}{86400}(1 - k_{n+1}) + Q_n\, k_{n+1} \tag{3.1}$$

Where Q is the daily discharge in $m^3/s$, $C_S$ and $C_R$ are the runoff coefficients for snow and rain, respectively, a is the degree-day factor ($cm^{o}C^{-1}d^{-1}$), $T_n + \triangle T_n$ are the degree days ($^{o}Cd^{-1}$) after extrapolation for each zone mean elevation, S is the ratio of snow-covered area to the zone area, P is precipitation contributing to runoff (cm), A is the zone area ($km^2$), k is the recession coefficient (input as ‘x’ and ‘y’ in the model) and n shows the sequence of days.

The critical temperature ($T_{crit}$) is used to decide the precipitation phase as snow or rain. If the precipitation is determined as snow, its delayed effect is considered in two ways: (1) snowfall over the snow-covered area is assumed to become part of the snowpack and its contribution is determined by the snow depletion curve (Martinec et al., 2007) and (2) snowfall occurring over snow-free areas contributes to the discharge immediately, depending on the available degree days. When the precipitation is determined as rain its contribution to the discharge depends on the snowpack characteristics. In winter, the snowpack is dry and thick, so the rain falling over the SCA is retained by the snowpack and the rain contribution to the total runoff is limited to the only snow-free area. Later in the summer, the snow becomes ripe, and the rain is allowed to contribute to the runoff from the entire zone area. The rainfall-induced melting and base flow (sub-surface fluxes) are ignored in SRM (Martinec et al., 2007). Further, the glacier ice melt contribution is also ignored (Tahir et al., 2011).

### 3.3.2 Model parameters

In SRM, a total of nine different parameters are used. These parameters are runoff coefficient for snow and rain ($C_S$ and $C_R$), degree-day factor (a), temperature lapse rate (LR), critical temperature ($T_{crit}$), time lag, recession coefficients (x and y), and rainfall contributing area (RCA). In rough terrain like the Himalaya, the measurement of these parameters is very difficult because of the remote access and adverse climate conditions. But the Chhota Shigri Catchment is one of the glacier catchments which is having the longest series of observed meteorological data and discharge measurements (Azam, 2021), hence among the nine parameters three parameters (LRs, 'x' and 'y') were calculated and constrained using the field measurements in the Chhota Shigri Catchment, whereas the other model parameters were calibrated for the Chhota Shigri Catchment.

$C_S$ and $C_R$ represent the losses between the available water (snowmelt + rainfall) and the runoff volume from the catchment or basin; it depends on the surface conditions in the catchment or basin. The default values of $C_S$ and $C_R$ in the model were adopted initially for the Chhota Shigri Catchment as 0.7 and 0.6 for $C_S$ and $C_R$, respectively (Martinec et al., 2007). 'a' is converting the positive temperatures on a particular day into the melt depth. For the Chhota Shigri Catchment, the initial 'a' was considered as 5.28 mm°C$^{-1}$d$^{-1}$ (Azam et al., 2014). The daily temperature LRs for the Chhota Shigri Catchment were available between the two temperature measurement stations at 3850 m a.s.l. (base camp) and 4863 m a.s.l. (AWS station) (Mandal et al., 2022; Srivastava et al., 2022). The mean LR was 0.63 °C(100m)$^{-1}$ and it was 0.71°C(100m)$^{-1}$ for summer (May–September) and 0.57 °C(100m)$^{-1}$ for winter (October–April). For precipitation extrapolation, a precipitation gradient ($P_G$) of 0.20 m/km was adopted, constrained through a mass balance model calibration on the Chhota Shigri Glacier (Azam et al., 2014). $T_{crit}$ is the threshold temperature that determines the precipitation phase. The time lag is the time interval between the start of increasing temperature and the corresponding increase in discharge. For both the catchment and basin, a time lag range from 6 to 18 hours was adopted, varying with the elevation zones from previous studies (Martinec et al., 2007; Tahir et al., 2011; Panday et al., 2014). The time lag tends to increase with elevation because at higher elevations, the mean temperature is less and the travel time for the melted water to the discharge point is more as compared to the lower zones, which results in the delayed discharge from the higher elevations. k deals with the proportion of the daily discharge which appears immediately in the runoff. In the SRM, this coefficient is used in the form of 'x' and 'y', which is usually determined by the historical discharge series. Based on the relation between k, 'x', 'y', and discharge i.e., $k = \frac{Q_{n+1}}{Q_n}$ and $k_{n+1} = xQ_n{}^{-y}$ the values of 'x' and 'y' can be determined (Martinec et al., 2007). In our study, the value of 'x' and 'y' were calculated from the available discharge series for the Chhota Shigri Catchment and Chandra-Bhaga Basin. The RCA was taken as 1 for summer and 0 for winter depending on the melting season for both catchment and basin. RCA 1 represents that the rain from the total zone area is contributing to the runoff and 0 shows that rain only from the snow-free area is contributing to the runoff.

### 3.3.3 Model variables

Precipitation, temperature, and SCA are the three most important input variables in SRM, which are required to simulate the daily discharge (Martinec et al., 2007). The bias-corrected temperature and precipitation data were extrapolated from the ERA5 grid point for the mean altitude of each elevation zone using the daily LR and $P_G$, respectively, available from previous studies in the Chhota Shigri Catchment (Azam et al., 2019; Srivastava et al., 2022). The extrapolated daily temperature and precipitation values were fed into the model, separately for each zone in both the Chhota Shigri Catchment and Chandra-Bhaga Basin. The model also needs daily SCA fractions as an input, which is the ratio of zonal SCA to the total zonal area. For each zone, these values were calculated at a daily timestep as discussed in section 3.2.2.3.

### 3.3.4 Model calibration and validation

The model for the Chhota Shigri Catchment was calibrated with the observed discharge values over 2010–2013 (Figure 3.5A). The parameters $T_{crit}$, 'a', $C_S$, $C_R$, x, and y were calibrated over 2010–2013 while LR, time lag, and RCA were kept constant. The calibrated parameters were kept within a permissible range corresponding to the previous studies on SRM to avoid the overfitting of the model. The calibration was done by considering different performance criteria, i.e., coefficient of determination ($R^2$), RMSE, and NSE (Nash-Sutcliff efficiency), which is determined using the equation:

$$R^2 = \left[\frac{\sum_{i=1}^{n}\{(O_i-O')*(S_i-S')\}}{\sqrt{\sum_{i=1}^{n}(O_i-O')^2 * \sum_{i=1}^{n}(S_i-S')^2}}\right]^2 \qquad (3.2),$$

$$RMSE = \sqrt{\frac{\sum_{i=1}^{n}(O_i-S_i)^2}{n}} \qquad (3.3),$$

$$NSE = 1 - \frac{\sum_{i=1}^{n}(O_i-S_i)^2}{\sum_{i=1}^{n}(O_i-O')^2} \qquad (3.4),$$

Here, n, $O_i$, $S_i$, $O'$ and $S'$ are the number of observations, observed discharge, simulated discharge, mean observed discharge and mean simulated discharge, respectively. NSE lies between 1 to $-\infty$ where 1 corresponds to the perfect match and $R^2$ lies between 0 to 1. The calibrated parameters are shown in Table 3.2.

### 3.3.5 Sensitivity and uncertainty estimation

To understand the sensitivity of simulated discharge to different model parameters, sensitivity analysis was performed for eight model parameters including k (x and y), $C_S$, $C_R$, ‘a’, $T_{crit}$, LR, and time lag. The sensitivity analysis was performed separately for both the Chhota Shigri Catchment and Chandra-Bhaga Basin over 2003–2018. For sensitivity analysis, each parameter was increased and decreased one by one by 10%, 20%, and 30% while keeping all other parameters constant, and the sensitivities were estimated using simulated mean daily discharge (Oerlemans et al., 1998) as follows:

$$S = \frac{Q_H - Q_L}{2} \qquad (3.5),$$

Here, S is the sensitivity of each parameter, $Q_H$ $and$ $Q_L$ is the mean daily discharge values at the highest (+10%, +20% and +30%) and lowest (−10%, −20% and −30%) values of parameters. For the uncertainty estimation in the simulated discharge, each model parameter among x, y, $C_S$, $C_R$, ‘a’, and $T_{crit}$ were changed one by one, within a 10% range of its calibrated value (Heynen et al., 2013; Ragettli et al., 2013). The parameters which were not calibrated kept the same i.e., LR, time lag, and RCA, using the field observations from Chhota Shigri Catchment, are not changed in this process. The uncertainty estimation was done for both the study region Chhota Shigri Catchment and Chandra-Bhaga Basin separately. The overall mean uncertainty in the simulated daily discharge was estimated using the error propagation law as following:

$$U = \sqrt{\sum_{1}^{n} \left(\frac{Q_{+10\%} - Q_{-10\%}}{2}\right)^2} \qquad (3.6),$$

Here, U is the overall uncertainty, n is the number of parameters, and $Q_{+10\%}$ $and$ $Q_{-10\%}$ are the mean daily simulated discharge when the parameters increased and decreased by 10%.

## 3.4 Results and discussions

### 3.4.1 Calibration and validation

The calibrated daily discharge over 2010–2013 showed a good agreement with the observed data ($R^2$ = 0.90, RMSE = 2.92 and NSE = 0.05) (Figure 3.5A). However, the mean calibrated discharge showed an underestimation of 41%

(Figure 3.5A, Figure 3.7A). As already highlighted, all the model parameters were kept within plausible ranges based on previous studies to avoid overfitting of the SRM. The 41% underestimation is most probably due to the lack of baseflow and glacier melt contribution in the SRM (details in section 3.4.7). After the calibration, the SRM output for the Chhota Shigri Catchment was validated with the observed discharge over 2014–2015. In validation the mean simulated discharge showed a good agreement with the observed discharge ($R^2 = 0.94$, RMSE = 2.34 and NSE = −0.13) (Figure 3.5B) but with an underestimation of 34% (Figure 3.5B, Figure 3.7A). After the validation, the same calibrated model was used to simulate the daily discharge for the Chhota Shigri Catchment over 2003–2018.

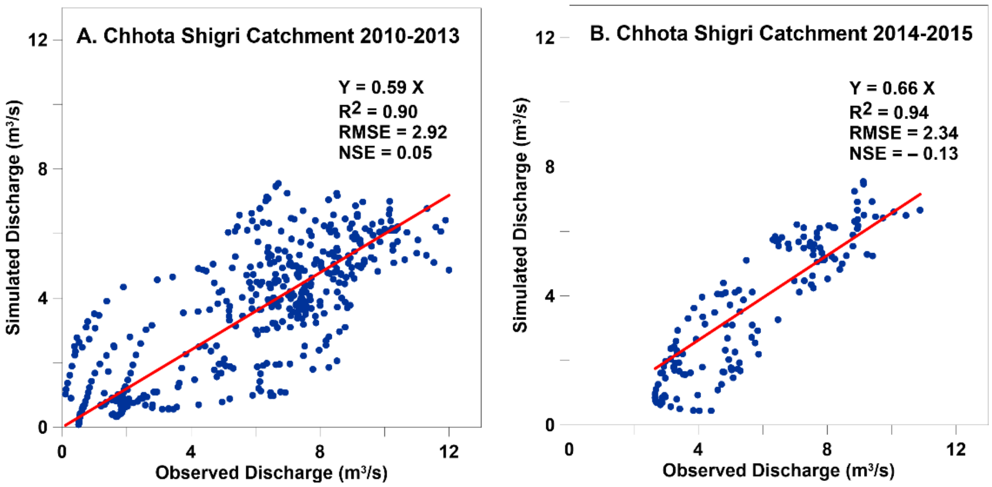

Figure 3.5 Scatter plots for calibration on Chhota Shigri Catchment over 2010–2013 (A) and validation on Chhota Shigri Catchment over 2014–2015 (B). Plots are showing the relations between observed and simulated discharges.

The observed daily discharge was also available for the Chandra-Bhaga Basin over 2004–2006. To check the transferability of catchment-scale calibrated model parameters to basin-scale discharge simulation, the discharge for Chandra-Bhaga Basin was simulated over 2004–2006 for two different case scenarios. Case-I: the calibrated parameters on Chhota Shigri Catchment were applied on all the zones in Chandra-Bhaga Basin and Case-II: the calibrated parameters were applied on zones having elevation above 3900 m a.s.l., as the Chhota Shigri Catchment is having a minimum elevation of ~3900 m a.s.l. and altered parameters (based on previous SRM studies) were applied for zones below 3900 m a.s.l.

In Case-II, for the zones below 3900 m a.s.l., the parameters were altered based on previous studies (Tahir et al., 2011; Panday et al., 2014). A lower value of ‘a’ (4.5 mm$^{o}$C$^{-1}$d$^{-1}$) was adopted for the lower zones because ‘a’ is expected to decrease with a decrease in elevation, due to the high direct solar radiation at higher altitudes (Hock, 2003; Zhang et al., 2006; Tahir et al., 2011; Panday et al., 2014). $T_{crit}$ for rain/snow separation was taken as 1.5 ºC for lower zones, like the previous studies in the western Himalaya (Singh and Jain, 2003; Aggarwal et al., 2014; Kiba et al., 2021). The values of $C_S$ and $C_R$ were also varied with the zone elevation, for the higher altitudes, the values for $C_S$ are higher and the values for $C_R$ are less as compared to the lower zones (Tahir et al., 2011; Panday et al., 2014). In the Chandra-Bhaga Basin for the lower elevations (below 3900 m a.s.l.), the values for these coefficients were altered as 0.5 and 0.75 for $C_S$ and $C_R$, respectively. The values of x, y, RCA, time lag, and LR were kept the same as the Chhota Shigri Catchment for all the zones (Table 3.2).

With the mentioned values of all the parameters for Case-I and Case-II (Table 3.2), the daily discharge for Chandra-Bhaga Basin was simulated over 2004–2006. The daily simulated discharge in both cases showed a good agreement with the observed discharge over 2004–2006 (Figure 3.6A, B) but an overestimation of 83% in Case-I and an overestimation of 74% in Case-II. Despite the underestimation in simulated discharge at Chhota Shigri Catchment, large discharge overestimation in the Chandra-Bhaga Basin showed that the catchment-scale calibrated parameters are not transferable for basin-scale discharge simulation. This overestimation is further discussed in section 3.4.7.

Table 3.2 List of calibrated parameters and their calibrated values for the Chhota Shigri Catchment over 2010–2013 and Chandra-Bhaga Basin over 2004–2006. 'Z' denotes the elevation zone.

| **Parameter** | **Chhota Shigri Catchment** | **Case-I (Chandra-Bhaga Basin)** | **Case-II (Chandra-Bhaga Basin)** | **Case-III (Chandra-Bhaga Basin)** |
|---|---|---|---|---|
| Critical temperature for snow/rain ($T_{crit}$) (ºC) | 0.1 (Z1–Z3) | 0.1 (Z1–Z16) | 1.5 (Z1–Z6),<br>0.1 (Z7–Z16) | 2 (Z1–Z6),<br>1 (Z7–Z16) |
| Degree day factor (a) ($mm^{o}C^{-1}d^{-1}$) | 6.8 (Z1–Z3) | 6.8 (Z1–Z16) | 4.5 (Z1–Z6),<br>6.8 (Z7–Z16) | 4.5 (Z1–Z6),<br>5.0 (Z7–Z16) |
| Runoff coefficient for snow (Cs) | 0.75 (Z1–Z3) | 0.75 (Z1–Z16) | 0.5 (Z1–Z6),<br>0.75 (Z7–Z16) | 0.4 (Z1–Z6),<br>0.5 (Z7–Z16) |
| Runoff coefficient for rain ($C_R$) | 0.70 (Z1–Z3) | 0.70 (Z1–Z16) | 0.75 (Z1–Z6),<br>0.70 (Z7–Z16) | 0.5 (Z1–Z6),<br>0.4 (Z7–Z16) |
| x | 0.85 | 0.85 | 0.85 | 1.0499 |
| y | 0.002 | 0.002 | 0.002 | 0.061 |

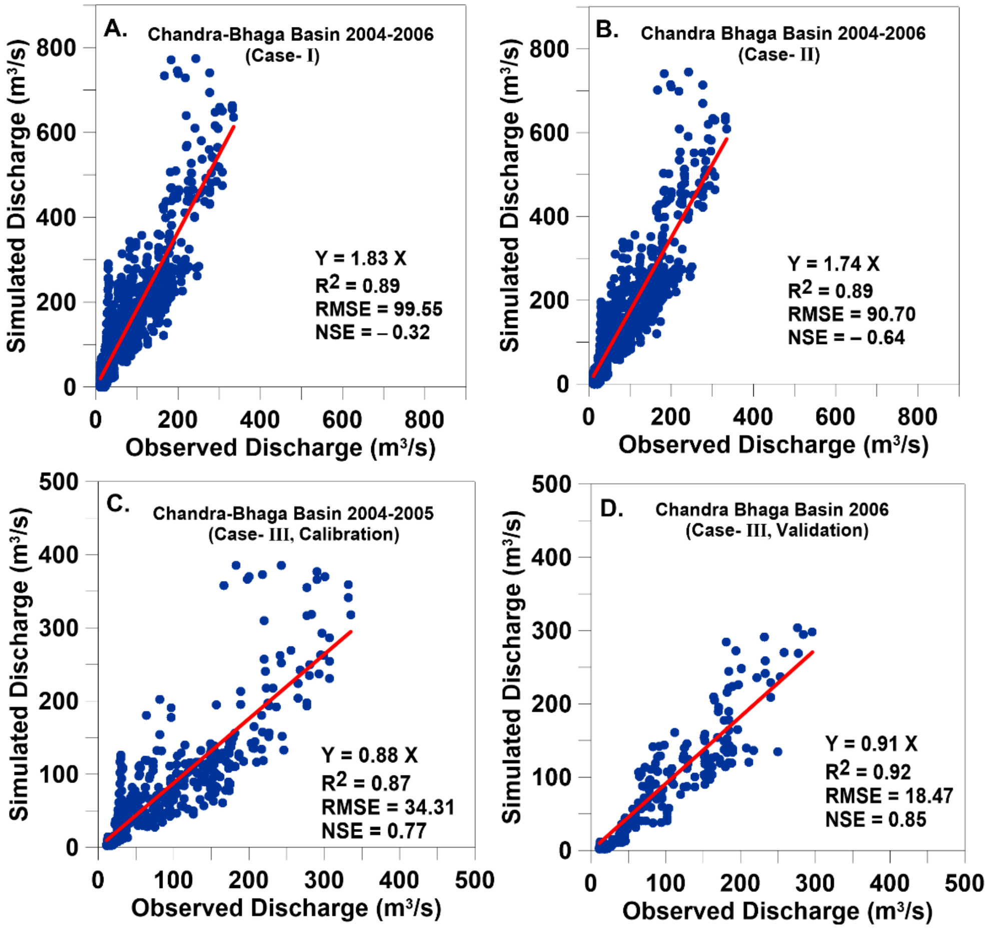

Figure 3.6 Scatter plots between the observed and simulated discharge for Chandra-Bhaga Basin in all three case scenarios (A) for Case-I, (B) for Case-II and (C) and (D) for Case-III.

Apart from these two case scenarios (Case-I and Case-II), where the Chandra-Bhaga simulated discharge is largely overestimated, an independent model calibration was performed for the Chandra-Bhaga Basin using the discharge data from Tandi village (Case-III; Table 3.2), ignoring the calibrated parameters on Chhota Shigri Catchment. The calibrated daily discharge over 2004–2005 showed a good agreement with the observed data with $R^2 = 0.87$, RMSE = 34.31 and NSE = 0.77 (Figure 3.6C). After the calibration, the same model was validated with the observed data for 2006 that showed a good agreement with $R^2 = 0.92$, RMSE = 18.47 and NSE = 0.85 (Figure 3.6D). The calibrated and validated modelled discharge in Chandra-Bhaga Basin showed an underestimation of 12% and 9%, respectively unlike the overestimation shown in Case-I and Case-II for the same basin. The daily discharge for the

Chandra-Bhaga Basin was simulated with these calibrated parameters over 2003–2018.

### 3.4.2 Reconstructed daily discharge and its pattern

The discharge from Chhota Shigri Catchment and Chandra-Bhaga Basin was reconstructed for 2003–2018 at a daily time step (Figure 3.7). The mean of daily discharges over 2003–2018 for the Chhota Shigri Catchment was 1.2 ± 0.2 $m^3/s$ (Figure 3.7A). In the Chhota Shigri Catchment, the simulated daily discharge starts increasing in April and reaches the maximum in July. The highest peak in daily discharge was observed on 11th July 2005 of 7.9 ± 1.4 $m^3/s$. The mean of daily discharges in the Chandra-Bhaga Basin was 55.9 ± 12.1 $m^3/s$ over 2003–2018 (Figure 3.7B). The daily discharge starts increasing in March and reaches its peak in July. The highest daily discharge was observed on 16th July 2011 of 386.7 ± 21.2 $m^3/s$. The observed daily discharge values for the Chhota Shigri Catchment over 2010–2015 and for Chandra-Bhaga Basin over 2004–2006 are also shown in Figure 3.7. The comparison showed that the simulated discharge in both the catchment and basin was underestimated (discussed in section 3.4.1).

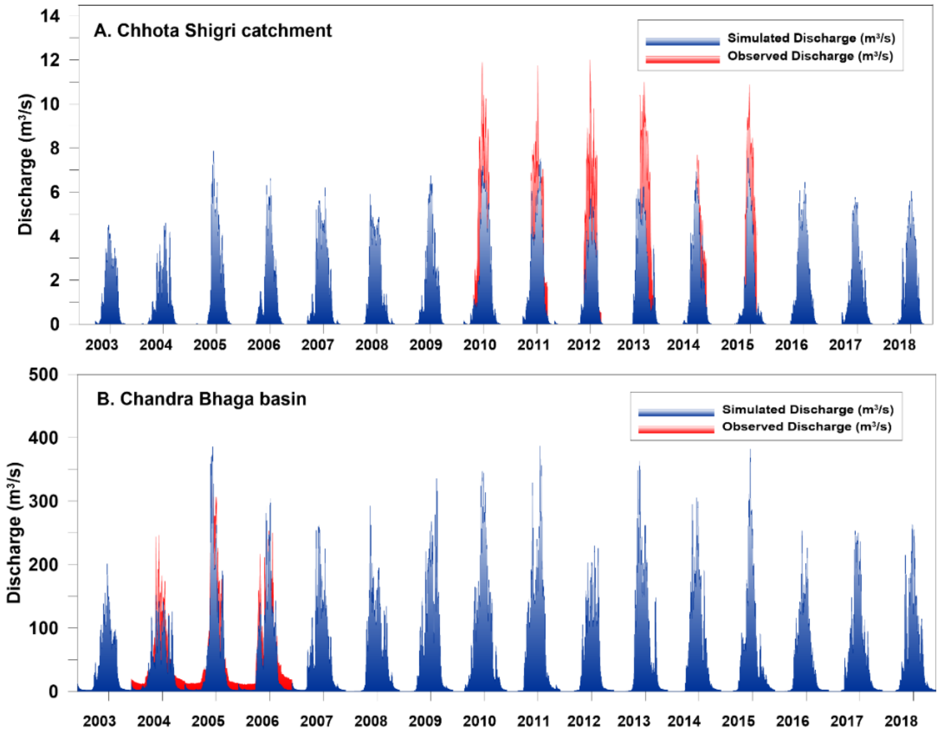

Figure 3.7 Simulated discharge of Chhota Shigri Catchment (A) and Chandra-Bhaga Basin (B) over 2003–2018 (blue color). The observed discharge for

Chhota Shigri Catchment (A) and Chandra-Bhaga Basin (B) in red color over 2010–2015 and 2004–2006, respectively.

### 3.4.3 Seasonal and annual discharge patterns

To understand the seasonal and annual patterns, the seasonal and annual discharge was computed using daily simulated discharge for Chhota Shigri Catchment and Chandra-Bhaga Basin over 2003–2018. Summer discharge has been considered from May to September and winter discharge has been considered from October to December and January to April in the same year. The mean summer discharge and winter discharge were found as 2.7 ± 0.5 $m^3/s$ and 0.1 ± 0.05 $m^3/s$ for Chhota Shigri Catchment, Similarly, for Chandra-Bhaga Basin it was 123.9 ± 22.3 $m^3/s$ and 6.7 ± 3.3 $m^3/s$, respectively. The simulated discharge ranged from 0.02 ± 0.01 $m^3/s$ to 0.2 ± 0.04 $m^3/s$ and 2.6 ± 1.2 $m^3/s$ to 13.3 ± 4.7 $m^3/s$ in winter and 1.9 ± 0.3 $m^3/s$ to 3.4 ± 0.6 $m^3/s$ and 77.6 ± 13.7 $m^3/s$ to 164.5 ± 28.3 $m^3/s$ in summer for Chhota Shigri Catchment and Chandra-Bhaga Basin, respectively. The annual discharge is the mean discharge in both seasons over the same year. The mean annual discharge for the Chhota Shigri Catchment was found as 1.2 ± 0.2 $m^3/s$ over 2003–2018 with a minimum annual discharge of 0.8 ± 0.1 $m^3/s$ in 2004 and a maximum of 1.5 ± 0.3 $m^3/s$ in 2011 (Figure 3.8B). The mean annual discharge for the Chandra-Bhaga Basin was found as 55.9 ± 12.1 $m^3/s$ over 2003–2018 with a minimum annual discharge of 39.9 ± 9.1 $m^3/s$ in 2003 and a maximum annual discharge of 75.1 ± 13.2 $m^3/s$ in 2010 (Figure 3.8C). The mean summer discharge dominates the mean winter discharge over 2003–2018 in the Chhota Shigri Catchment as well as in the Chandra-Bhaga Basin. Similar results were also suggested for the Chhota Shigri Catchment and Chandra Basin in the western Himalaya (Singh et al., 2021a; Gaddam et al., 2022; Srivastava and Azam, 2022b).

The year 2016 has the maximum temperature and minimum precipitation (Figure 3.8A). It is noteworthy that 2016 was the warmest year over a century (Wuebbles et al., 2017). This year, though the winter SCA was relatively less, the Chhota Shigri catchment showed more than the average discharge because of excessive snowmelt runoff production, mainly supported by quasi average summer SCA (Figure 3.8B). Conversely, in the Chandra-

Bhaga Basin, the modelled discharge was less than average because of the lowest precipitation (Rain + Snow), and lowest winter as well as summer SCA (Figure 3.8C). Similarly, in 2011 the Chhota Shigri Catchment showed the maximum discharge having average precipitation and associated with the higher snowmelt due to higher temperature and higher summer SCA (Figure 3.8B). While the Chandra-Bhaga Basin showed the maximum discharge in 2010 due to the maximum precipitation and higher summer SCA (Figure 3.8C).

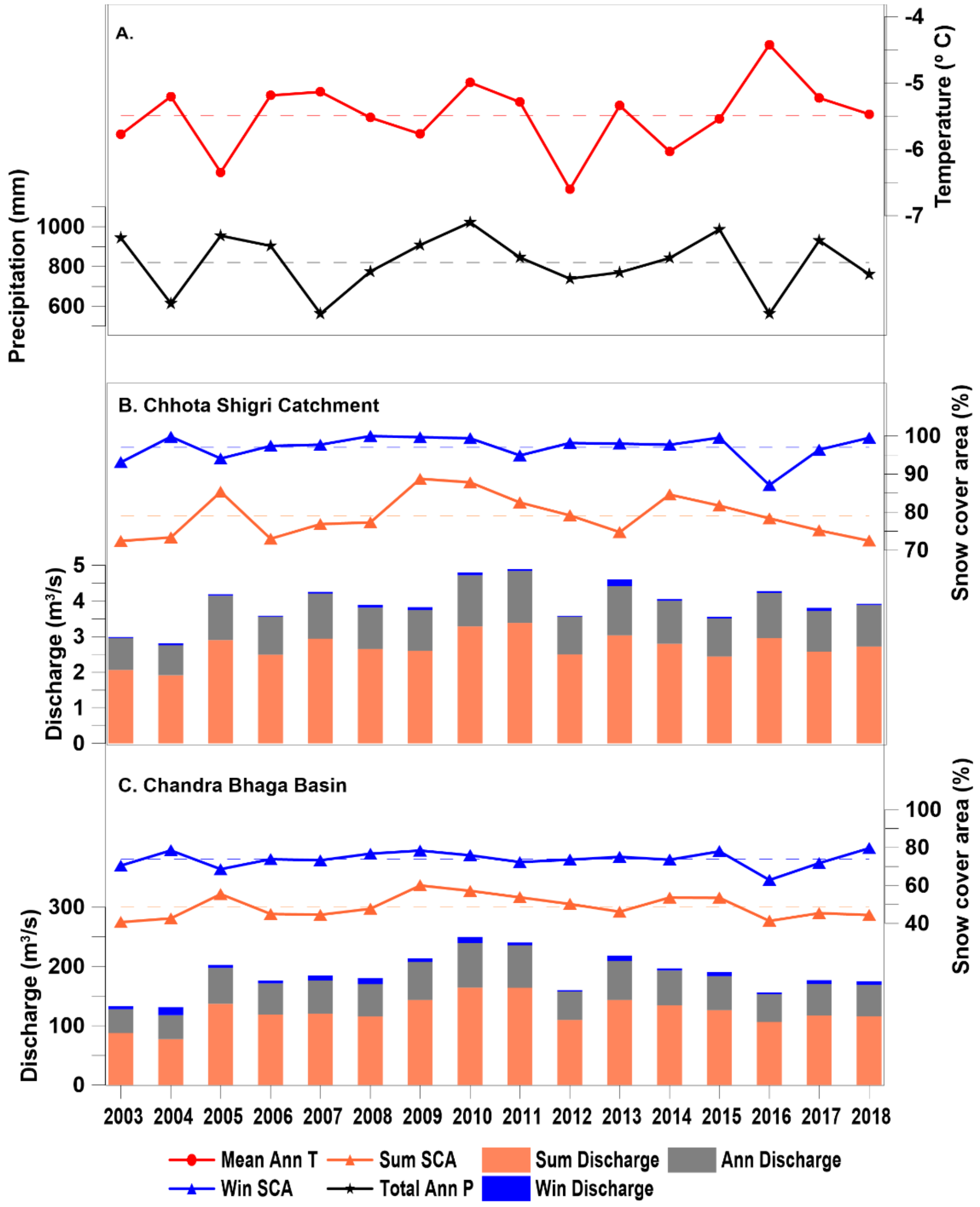

Figure 3.8 Seasonal (summer in orange and winter in blue) and annual (grey) discharge patterns over 2013–2018 with total precipitation (black) and mean temperature (red) patterns for Chhota Shigri Catchment (B) and Chandra-

Bhaga Basin (C). The summer season is from May to September and the Winter season is from October to December and January to April. Total precipitation and mean temperature patterns plotted here represent the data from the ERA5 grid point location (A). Dashed lines show the average values over 2003–2018 of temperature (red), Precipitation (black), winter SCA (blue), and summer SCA (orange).

Further, to understand the influence of variables on discharge, the interrelationships between the discharge (annual, summer, and winter), SCA (annual, summer, and winter), and temperature and precipitation (annual, summer, and winter) were explored with the help of the correlation matrix developed separately for both the study regions (Figure 3.9). In both the study regions, the annual discharge is highly correlated with the summer discharge as the maximum melting occurs in summer (Figure 3.9). The annual discharge in the Chhota Shigri Catchment is more correlated with summer temperature (r = 0.51) and summer SCA (r = 0.47) and has a very weak correlation with the annual precipitation (Figure 3.9A). These relations are expected because the higher altitude of the catchment provides more snowfall than rainfall hence catchment discharge is mainly dominated by snowmelt. Similarly, the summer discharge also showed the same relationship with the summer temperature and summer SCA (Figure 3.9A). Due to very low temperatures, winter discharge was negligible (4% of summer discharge) hence relationships were insignificant.

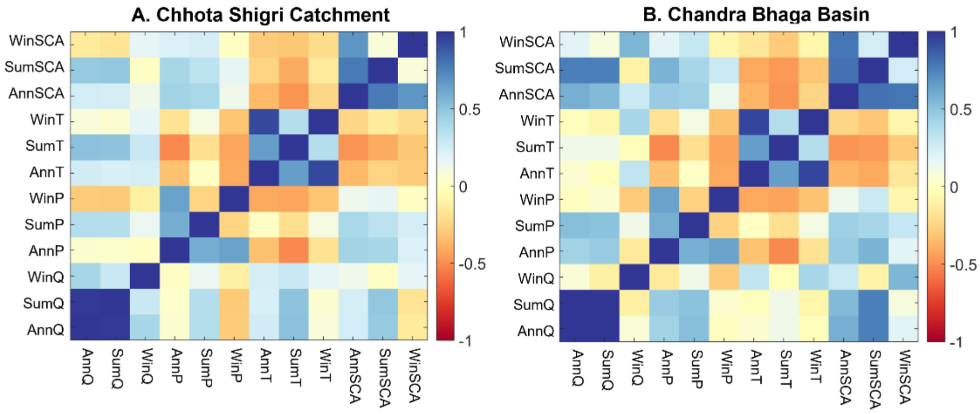

Figure 3.9 Correlation matrix for Chhota Shigri Catchment and Chanda-Bhaga Basin. The values from −1 to 1 denote the correlation coefficients and the color range denotes the intensity of the correlation (1 denotes the completely

positive correlation, dark blue, and −1 denotes the completely negative correlation, dark brown). Ann, Sum, and Win = annual, summer, and winter season, and Q, P, T, and SCA are discharge, precipitation, temperature, and SCA, respectively.

In the Chandra-Bhaga Basin, the annual discharge showed a strong correlation with the summer SCA (r = 0.74) followed by summer precipitation (r = 0.53) (Figure 3.9B), as the basin has lower altitudes (up to 2804 m a.s.l.), receives a significant contribution of rainfall that directly contributes to discharge. The same relation was also shown by the summer discharge with summer SCA and summer precipitation (Figure 3.9B). Though the winter discharge was only 6% it was fairly correlated with the winter SCA (r = 0.56) and winter temperature (r = 0.41) (Figure 3.9) because sometimes at lower altitudes positive temperatures may occur in March and April which generates some snowmelt. In all, the discharge in Chhota Shigri Catchment is equally driven by both summer temperature and summer SCA while in the Chandra-Bhaga Basin summer SCA and summer precipitation exert a strong control on the discharge.

### 3.4.4 Contribution of different components to total discharge

The modelled discharge from SRM includes the contribution from rainfall and snowmelt. The snowmelt is considered in two ways: melt from 'New snow' and 'Initial snow'. 'New snow' melt is the sum of melts from the snow melt from nth day snowfall and remained snow on the previous days from the non-snow cover area in the catchment. 'Initial snow' melt is the melt contribution coming from the depletion of snow cover. The percentage contribution of different components in discharge for Chhota Shigri Catchment and Chandra-Bhaga Basin is shown in Figure 3.10.

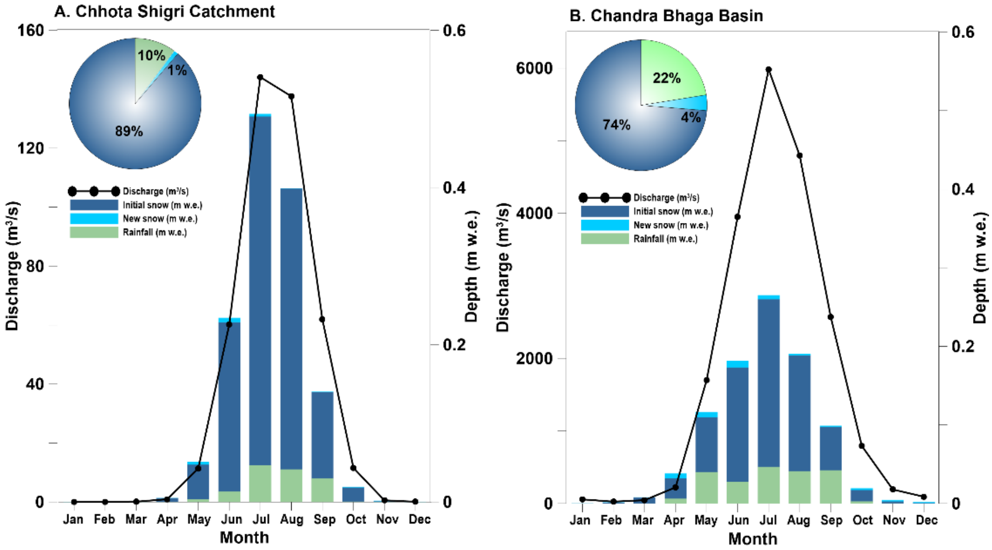

Figure 3.10 Monthly hydrograph of total discharge (black line) and depth of different components contributing to the total discharge: Initial snow (blue), new snow (sky blue), and rainfall (light green) over 2003–2018 for Chhota Shigri Catchment (A) and Chandra-Bhaga Basin (B). The pie chart shows the percentage contribution of each component.

The percentage contribution of snowmelt as initial snow from SCA to total discharge was highest with 89% and 74% in Chhota Shigri Catchment and Chandra-Bhaga Basin, respectively. The contribution of monthly snowmelt from the SCA was maximum over July in both the study regions in agreement with the maximum monthly mean temperatures (Figure 3.3). As expected, the contribution of total snow melt (initial snow + new snow) to total discharge was significantly more in the Chhota Shigri Catchment (90%) compared to the Chandra-Bhaga Basin (78%) (Figure 3.10). Whereas the contribution of new snow was higher in Chandra-Bhaga Basin (4%) as compared to the Chhota Shigri Catchment (1%). The higher melt contribution of new snow in the Chandra-Bhaga Basin was due to the higher temperatures at the lower zones (below 3900 m a.s.l.) than Chhota Shigri Catchment, which promotes the melting of new snow. As expected, the rainfall contribution to total discharge was higher (22%) in the Chandra-Bhaga Basin than in the Chhota Shigri Catchment (10%) due to the lower elevation zones (below 3900m a.s.l.) that favour more rainfall due to higher temperatures.

The monthly depth (new snowmelt + initial snowmelt + rainfall) was maximum in July as 0.49 ± 0.03 m w.e. and 0.27 ± 0.02 m w.e. for Chhota

Shigri Catchment and Chandra-Bhaga Basin, respectively (Figure 3.10A and 3.10B). The total annual depth (1.34 ± 0.01 m w.e.) in Chhota Shigri Catchment was more than the Chandra-Bhaga Basin (0.93 ± 0.05 m w.e.) because the higher $T_{crit}$ (1 °C at above 3900 m a.s.l. and 2°C at below 3900 m a.s.l.) in the Chandra-Bhaga Basin compared to $T_{crit}$ (0.1 °C) in the Chhota Shigri Catchment results in a relatively higher amount of snow available for melt from snowfall (section 3.4.1). Snow takes relatively more time to contribute to the discharge and sometimes may not produce melt due to limited degree days and become part of storage that is nullified at the end of each calendar year, a limitation of the SRM discussed in section 3.4.7. Due to the lower $T_{crit}$ (0.1 °C) a larger portion of precipitation is considered as rainfall in Chhota Shigri Catchment which directly contributes to the discharge and further results in higher depth than Chandra-Bhaga Basin.

### 3.4.5 Decadal discharge patterns

Studies suggest that volumetric and seasonal changes are occurring in the HK river runoffs due to climate change (Azam et al., 2021; Lutz et al., 2014). Though our simulation period is short (2003−2018), the decadal variations in discharge were analysed by comparing two time periods of equal length as 2003−2010 and 2011−2018. A higher discharge was found over 2011−2018 period than 2003−2010 period in both Chhota Shigri Catchment and Chandra-Bhaga Basin. The mean monthly discharge in the Chhota Shigri Catchment increased by 8% from 1.1 ± 0.2 $m^3/s$ to 1.2 ± 0.3 $m^3/s$ over 2011−2018 as compared to 2003−2010. Similarly in the Chandra-Bhaga Basin, the mean monthly discharge increased by 2% from 54.9 ± 11.2 $m^3/s$ to 56.2 ± 13.9 $m^3/s$ over 2011−2018 as compared to 2003−2010. In both the study regions, the maximum monthly discharge occurred in July (Figure 3.11). The maximum monthly discharge increased by 11% from 4.4 ± 0.7 $m^3/s$ to 4.9 ± 0.7 $m^3/s$ for the Chhota Shigri Catchment and by 9% from 184.1 ± 25.9 $m^3/s$ to 201.8 ± 24.8 $m^3/s$ for the Chandra-Bhaga Basin in 2011−2018 as compared to 2003−2010 (Figure 3.11A and 3.11B).

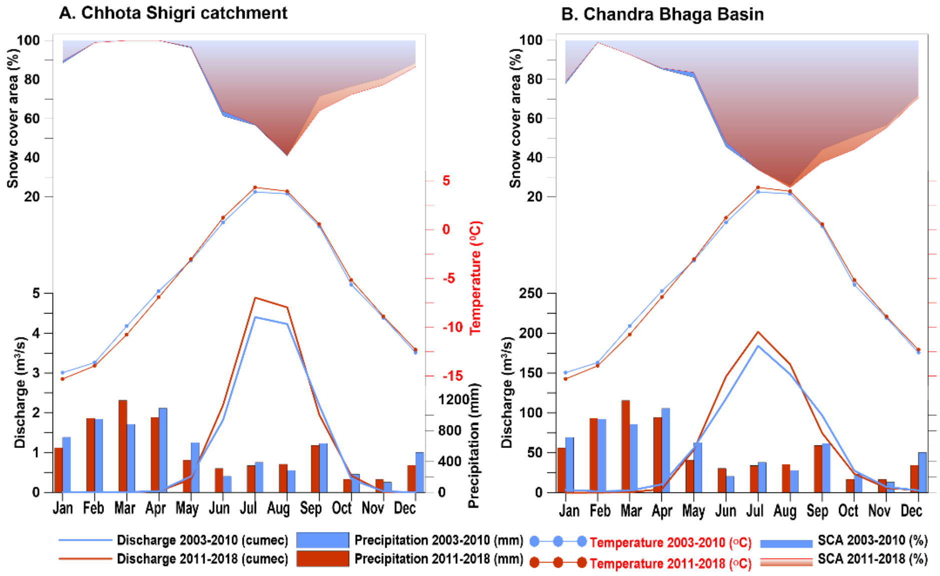

Figure 3.11 Decadal comparison of discharge with precipitation, temperature, and snow cover area over the two time periods 2003–2010 (blue color) and 2011–2018 (red color) for Chhota Shigri Catchment (A) and Chandra-Bhaga Basin (B).

In the Chhota Shigri Catchment, the mean monthly discharge over June-August increased by 11% from 4.3 ± 0.64 $m^3/s$ in the 2003-2010 to 4.8 ± 0.76 $m^3/s$ in 2011–2018 (Figure 3.11A). This increased discharge was due to the increased temperature in 2011–2018 (3.3 ºC) as compared to 2003–2010 (2.7 ºC) over June–August (Figure 3.11), having almost the same SCA in both periods (53% and 54%). Conversely, the discharge decreased in September over 2011–2018 as compared to 2003–2010 due to the lower SCA (64% as compared to 71%), even having a higher temperature by 0.2 ºC in 2011–2018 (Figure 3.11A). In the Chandra-Bhaga Basin, the mean monthly discharge also increased in summer by 11% from 126.5 ± 20.6 $m^3/s$ over 2003–2010 to 140.4 ± 30.4 $m^3/s$ over 2011–2018, except in September (Figure 3.11B). This increment in summer discharge resulted due to the increased precipitation from 882 mm in 2003–2010 to 1023 mm in 2011–2018 (over June–August) and increased SCA (over May–June) from 63% in 2003–2010 to 66% in 2011–2018 (Figure 3.11B). Similarly, in September the decreased precipitation by 27 mm and decreased SCA (37% as compared to 44%) resulted in lower discharge in the basin (Figure 3.11B). Though the summer discharge increased, the winter discharge decreased in both the study regions over 2011–

2018 period. In the Chhota Shigri Catchment the variations were negligible (< 1%) whereas in the Chandra-Bhaga Basin the winter discharge showed a significant decrease of 32% from 7.9 ± 5.2 $m^3/s$ over 2003–2010 to 5.3 ± 3.4 $m^3/s$ over 2011–2018 due to the decreased temperature over January–April by 0.6 ºC in 2011–2018 and decreased SCA (56% as compared to 60%) over October–December (Figure 3.11B). In line to section 3.4.3, the decadal analysis also suggested a large control of summer temperature and summer SCA in the Chhota Shigri Catchment and summer SCA and summer precipitation in Chandra-Bhaga Basin, for discharge generation in summer, and winter temperature and winter SCA control on winter discharge in the Chandra-Bhaga Basin.

Further, the hydrograph is also slightly shifted in early summer approximately by 10 days in the Chhota Shigri Catchment and 20 days in the Chandra-Bhaga Basin. The early onset of discharge or the seasonality shift was also observed in previous studies in the Indus Basin (Immerzeel et al., 2010; Tahir et al., 2011; Lutz et al., 2014; Hasson, 2016). In this study, the change in seasonality occurred due to the higher temperatures and higher SCA in the early summer months (May and June) and also the early occurring precipitation peak in March over 2011–2018 as compared to April over 2003–2010 (Figure 3.11). Similar to our study (Lutz et al., 2014) and (Immerzeel et al., 2010) also highlighted the increased precipitation and shift in the snowmelt peak (due to high temperature) as the main cause of the seasonality shift in the Indus Basin.

## 3.4.6 Sensitivity analysis

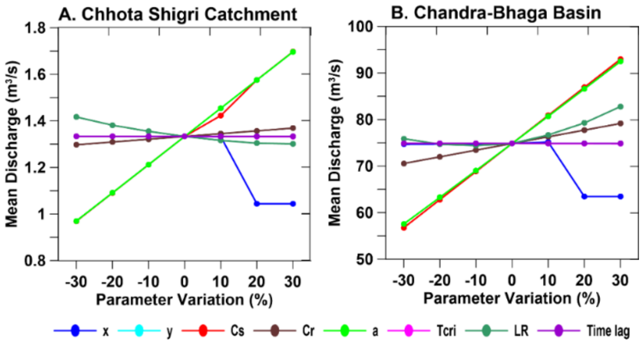

Figure 3.12 Sensitivity analysis results for Chhota Shigri Catchment (A) and Chandra-Bhaga Basin. The X-axis shows the percentage variation in the values

of each parameter and the Y-axis shows the corresponding simulated mean daily discharge values.

In the Chhota Shigri Catchment, the simulated discharge was almost equally sensitive to ‘a’ and $C_S$ with a sensitivity of 0.098 and 0.099 $m^3/s$, respectively (Figure 3.12A, Table 3.3). Other parameters $C_R$, and LRs showed mean sensitivities of −0.011 $m^3/s$, and 0.015 $m^3/s$, respectively, whereas the model is less sensitive to ‘x’ and $T_{crit}$ (Table 3.3). Parameters ‘y’ and time lag showed no impact on simulated discharge in the Chhota Shigri Catchment. In the Chandra-Bhaga Basin, the simulated discharge was most sensitive to $C_S$ with a sensitivity of 5.2 $m^3/s$ followed by ‘a’ with a sensitivity of 5.0 $m^3/s$ (Figure 3.12B, Table 3.3) whereas among the other parameters the model is more sensitive to $C_R$, and LR as compared to ‘x’ and Tcrit with ‘y’ and time lag have no impact on simulated discharge, similar to the Chhota Shigri Catchment (Table 3.3). Other studies by Siemens et al. (2021) and Panday et al. (2014) also found that the parameters $C_{S,}$ $C_R$, ‘x’, and ‘y’ have substantial control over the simulated discharge. The analysis showed almost linear changes in the simulated discharge with variations in each sensitive parameter value except for parameter ‘x’ (Figure 3.12). The simulated discharge varied significantly when the parameter value of ‘x’ increased from 10% to 20% and became constant after this. Whereas it showed no significant change in the discharge when the value of ‘x’ was reduced. This varying pattern was due to the maximum limit of k as 0.99 in WinSRM (section 3.3.2), which restricts the value of ‘x’ and ‘y’ according to the maximum value of k. A significant impact of LR was found on simulated discharge, which is also highlighted by Jain et al. (2010) and Panday et al. (2014). In this study, daily temperature LRs were used which were observed in the Chhota Shigri Catchment, which is among the sensitive parameters in both the study regions. The adopted daily LR values enable the SRM to capture the seasonal variations in the discharge (Figure 3.8) which is not possible with constant LR values over a year. The daily LRs reduce the possibility of errors in the extrapolated temperature values which directly affects the snowmelt in the different seasons. The overall mean uncertainty in the simulated daily discharge was found as ± 0.2 $m^3/s$ and ± 12.1 $m^3/s$ for Chhota Shigri Catchment and Chandra-Bhaga Basin, respectively.

Table 3.3 List of model parameters and their sensitivities for the Chhota Shigri Catchment and Chandra-Bhaga Basin (Case-III)

| **Parameters** | **Sensitivities ($m^3/s$)** | |
|---|---|---|
| | **Chhota Shigri Catchment** | **Chandra-Bhaga Basin** |
| x | −0.0004 | −0.79 |
| Runoff coefficient for snow ($C_S$) | 0.099 | 5.2 |
| Runoff coefficient for rain ($C_R$) | −0.011 | 1.06 |
| Degree day factor (a) | 0.098 | 5.0 |
| Critical temperature ($T_{crit}$) | −0.00002 | −0.18 |
| Lapse rate (LR) | 0.015 | 1.3 |

* Parameters ‘y’ and time lag showed no impact on discharge

### 3.4.7 Model limitations and transferability of catchment-scale calibrated model parameters to basin scale

In section 3.4.1, the model limitations and transferability of catchment-scale calibrated model parameters to basin-scale discharge simulation in the same basin were introduced and investigated in this section in detail. The simulated daily discharge in the Chhota Shigri Catchment was underestimated (41% and 34%) over the calibration (2010–2013) and validation (2014–2015) periods, respectively (Figure 3.5A, 3.5B, Figure 3.7A). The SRM does not involve the baseflow and glacier melt runoff contribution to the total discharge. Given that the Chhota Shigri Catchment is highly glacierized (47%), base flow contribution can be neglected (Srivastava and Azam, 2022b). However, glacier melt contribution cannot be ignored, and probably this is the reason for the underestimation in simulated discharge as glacier provides significant runoff contribution through glacier melt (around 21% of the total runoff; (Srivastava and Azam, 2022b). In line, the simulated discharge in Case-III for the Chandra-Bhaga Basin was also underestimated (12% over 2004–2005 and 9% over 2006). The relatively less underestimation in the Chandra-Bhaga Basin is probably associated with the less glacierized area (25%) in the Chandra-Bhaga Basin as compared to the Chhota Shigri Catchment (47%). Another reason for this underestimation in SRM simulated discharge in both the catchment and basin scale could be the stored snow at higher altitudes (above zero-degree isotherm) which does not melt at the end of the year and cannot be added to the next successive year's simulation in the SRM scheme.

Conversely, when the calibrated model parameters from Chhota Shigri Catchment were applied to simulate the discharge from the Chandra-Bhaga Basin, the simulated discharge in Chandra-Bhaga Basin in Case-I and Case-II was overestimated (83% and 74%) by the SRM over 2004–2006 (section 3.4.1; Figure 3.6 A, B). The overestimation in simulated discharge could partially be due to the parameter values which may not be applicable for lower elevation zones (below 3900m a.s.l.) in Chandra-Bhaga Basin. The precipitation phase (snow vs rain) patterns over Chhota Shigri Catchment and lower zones of Chandra-Bhaga Basin (below 3900 m a.s.l.) are quite different as the Chhota Shigri Catchment receives frequent snowfall while the Chandra-Bhaga Basin is having relatively more rainfall frequency due to the inclusion of the lower altitudes in the basin. The values of $T_{crit}$ in Case-I (0.1 ºC) and Case-II (1.5 ºC ) are lower than the calibrated value of Tcrit in Case-III (2 ºC) for lower zones of Chandra-Bhaga Basin. These lower values of $T_{crit}$ (Case-I and II) are expected to convert a large portion of precipitation into rainfall instead of snowfall as in Case-III. This extra amount of rainfall considered in Case-I and Case-II due to lower $T_{crit}$ contributes to the overestimation of simulated discharge while the additional snowfall in Case-III due to higher $T_{crit}$ may not be melted out completely. Further, the higher value of $C_S$ used in Case-I (0.75) and Case-II (0.5) for lower zones (below 3900 m a.s.l.) also causes the discharge overestimation in the Chandra-Bhaga Basin in Case-I and Case-II because these values are higher than the calibrated value (0.4) at the basin (Case-III). Similarly, the value for $C_R$, which directly increases the discharge, is also higher in Case-I (0.7) and Case-II (0.75) than the calibrated value (0.5) in Case-III.

Though the underestimation in the Chhota Shigri Catchment and overestimation in the Chandra-Bhaga Basin (Case-I and Case-II) can also partially be attributed to the high uncertainty of up to 25% in field discharge measurements in the turbulent Himalayan rivers (Eeckman et al., 2017). Our analysis clearly indicates that even after applying the SRM in a data-plenty catchment, the calibrated model parameters at the catchment scale may not be transferable to basin scale discharge simulation, even in the same basin therefore utmost care must be taken while using model parameters from other basins for the SRM applications.

### 3.4.8 Comparison with other studies

Previous studies estimated the discharge from the Chhota Shigri Catchment using a simplified glacio-hydrological model (Azam et al., 2019; Srivastava et al., 2022). In agreement with those studies, a dominance of snowmelt in the hydrology of the Chhota Shigri Catchment is suggested. Further, similar to our study, summer temperature was also one of the main drivers for discharge generation in the Chhota Shigri Catchment (Azam et al., 2019). The mean monthly hydrograph showed the maximum discharge in July (Figure 3.10A) however the peak of snowmelt runoff was found in July and total runoff in

August in (Azam et al., 2019). This is because SRM does not consider glacier ice melt in the simulation of discharge and the runoff generation is solely due to snow melt (from SCA and fresh snow) that peaks in July. In August, the snow cover is usually melted out up to 5000 m a.s.l. (Mandal et al., 2020) and ice is exposed to higher summer temperatures that contribute to runoff providing peak discharge (Azam et al., 2019). The rainfall contribution in the Chhota Shigri Catchment as 10% of the total discharge is similar to the previous study by (Srivastava and Azam, 2022b), showing a 10% combined contribution of rainfall from glacierized and nonglacierized areas. Hydrological studies are not available in the whole Chandra-Bhaga Basin, but a few studies cover the Chandra Basin (59% of Chandra-Bhaga Basin). These studies also showed a peak discharge in July (Singh et al., 2020, 2021b; Gaddam et al., 2022) similar to our study (Figure 3.10B). The increased discharge volume in 2011-2018 shown in this study is in agreement with the study by (Immerzeel et al., 2013) in the Baltoro watershed in the Indus Basin. Further, the seasonal shift observed in decadal hydrographs in our study has already been highlighted by some other studies in different regions of the Indus Basin (Immerzeel et al., 2010; Tahir et al., 2011; Lutz et al., 2014; Hasson, 2016).

## 3.5 Conclusions

The daily discharge series from the Chandra-Bhaga Basin and Chhota Shigri Catchment was reconstructed over the period 2003−2018 using SRM. Analysis showed that SRM efficiently simulated the discharge over the calibration and validation period. The mean annual discharge was found as 1.2 ± 0.2 $m^3/s$ and 55.9 ± 12.1 $m^3/s$ over 2003−2018 for the Chhota Shigri Catchment and Chandra-Bhaga Basin, respectively. The analysis suggests the overall discharge was mainly controlled by the summer temperature and summer SCA in the Chhota Shigri Catchment whereas by summer SCA and summer precipitation in the Chandra-Bhaga Basin. The decadal comparison showed that the mean discharge increased in 2011−2018 as compared to the mean discharge in 2003−2010 and also the hydrograph shifted in the early summer by 10 days in the Chhota Shigri Catchment and 20 days in the Chandra-Bhaga Basin associated with the higher mean temperature, higher SCA in early summer, and early precipitation peak in 2011–2018. Sensitivity analysis showed that the simulated discharge was equally sensitive to ‘a’ and $C_S$ in the Chhota Shigri Catchment and most sensitive to $C_S$ in the Chandra-Bhaga Basin. The daily LRs used in this study enable the SRM to capture the seasonal variations in discharge and further increase the model efficiency by simulating the discharge peaks accurately due to the varying LRs.

For the first time, the transferability of catchment-scale calibrated parameters to the basin-scale simulation of discharge was systematically checked using SRM. For this assessment, the model calibration was done on the data-plenty catchment of Chhota Shigri Glacier and calibrated parameters were then applied to the Chandra-Bhaga Basin in different case scenarios. This resulted in a large overestimation in the simulated discharge from the basin. Our analysis clearly showed that even though the model parameters in SRM are calibrated with plenty of field data at the catchment scale, their application to the basin-scale runoff simulation, even in the same basin, may not be applicable. Care must be taken while adopting the model parameters for SRM from other basins, especially for the ungauged basins. The calibrated SRM for the Chandra-Bhaga basin and the Chhota Shigri Catchment can be used to forecast future discharge and its patterns under various climate change scenarios. With a combination of an automatic calibration process and high-resolution snow cover product the efficiency of SRM can be improved in future work.

# Chapter 4

# Snow and glacier melt contributions from the Gangotri Glacier System and their climatic controls

## 4.1 Introduction

The snow and ice reserves of the Himalaya-Karakoram (HK) are essential water resources for the downstream populations, contributing to major rivers like the Indus, Ganga, and Brahmaputra (Azam et al., 2021; Nepal et al., 2023). Significant climatic changes have been observed in recent decades in the HK region, resulting in noticeable changes in the cryosphere and the hydrological cycle (Zhan et al., 2017; Krishnan et al., 2019). These changes have significantly altered the dynamics of glacier-fed hydrological systems, accelerating glacial retreat and shifting seasonal discharge patterns, which have profound implications for both upstream and downstream water availability (Lutz et al., 2014; Jackson et al., 2023; Srivastava et al., 2024). Hence, understanding the contribution of glacier and snowmelt to regional hydrology is crucial for assessing the sustainability of water resources in HK river basins.

Hydrological modelling studies in the HK have been conducted at large-scale basins, focusing primarily on the Indus, Ganges and Brahmaputra rivers (Immerzeel et al., 2010; Lutz et al., 2014; Khanal et al., 2021). However, these studies remain limited and face several challenges, (1) the scarcity of in-situ data for model calibration and validation, (2) difficulties in separating discharge contributions from snowmelt and ice melt, (3) the problem of equifinality, where different sets of model parameters yield similar outputs, leading to uncertainty in discharge estimates and (4) the general exclusion of glacier dynamics, mainly due to the unavailability of ice thickness and velocity data (Azam et al., 2021). The issue of equifinality, in particular, can be addressed using a multi-tier calibration approach that incorporates multiple datasets, such as glacier mass balance, discharge, and snow cover area (Beven, 2016; Eeckman et al., 2019; Azam et al., 2021). To improve the accuracy of discharge estimates, long-term in-situ data, multi-tier model calibration, and glaciohydrological models incorporating glacier dynamics are critically needed in HK.

Few studies have examined small-scale basins or catchments where field data such as river discharge, local meteorology and glacier mass balance are available. These studies offer valuable insights into snow and ice melt contributions and runoff patterns (Singh and Jain, 2002; Singh et al., 2021a; Srivastava and Azam, 2022b; Singh et al., 2023; Soheb et al., 2024; Srivastava et al., 2024). They typically employ semi-distributed or fully distributed models to estimate discharge contributions from snowmelt, glacier melt, and rainfall.

At the small catchment scale, one of the most studied glacier systems is the Gangotri Glacier System (GGS) in HK. GGS discharge has been analyzed using in-situ discharge measurements, environmental isotopes, and hydrological models such as SNOWMOD, HBV, and Spatial Processes in Hydrology (SPHY) (Haritashya et al., 2006; Singh et al., 2006, 2008, 2011; Rai et al., 2019; Salim and Pandey, 2021; Singh et al., 2023; Arora et al., 2024). A previous study discussed GGS discharge patterns using in-situ measurements over 2000–2003, emphasizing the critical role of glacial melt in sediment transport and the strong relationship between temperature, discharge, and sediment yield (Haritashya et al., 2006; Singh et al., 2006). Another study employed SNOWMOD, a temperature index model, to simulate snowmelt runoff using a hydro-meteorological database established near the glacier snout over four melt seasons (2000–2003) (Singh et al., 2008). To explore the time lag between melt generation and runoff emergence at the Gangotri Glacier outlet, hourly discharge and temperature data were collected near the snout (~4000 m) for three melt seasons (2004–2006) to analyze diurnal variations in water storage and runoff (Singh et al., 2011). Additionally, to quantify the fractional contributions of snowmelt and glacier melt, isotope-based hydrograph separation was applied for the ablation period of 2005 (Rai et al., 2019). The glacier melt runoff was modelled from 2010 to 2019 using MODIS satellite data and the SNOWMOD model within a GIS framework (Salim and Pandey, 2021). Another study by Singh et al. (2023) coupled GlabTop2 and SPHY models to understand the impact of glacier thickness change on the runoff of GGS over 2011–2020. Recently, a semi-distributed conceptual hydrological model (HBV) was applied to evaluate the contributions of snowmelt, glacier melt, and rainfall runoff over 2013–2019 (Arora et al., 2024). While these studies have provided valuable insights into GGS, long-term discharge analysis, evolution of meltwater contribution and understanding of the climatic drivers affecting GGS are still lacking.

To address these research gaps, the present study combines remote sensing datasets with hydrological modelling and focuses on long-term discharge analysis to provide a more reliable and comprehensive understanding of GGS hydrology since 1980. The SPHY model is applied to reconstruct long-term discharge and is calibrated using a two-tier approach by using Gangotri Glacier geodetic mass balance and in-situ discharge measured at Bhojbasa (3 km downstream from the Gangotri Glacier snout). The major objectives of this study are: (i) to develop a long-term GGS discharge series and assess snow and glacier melt contributions since 1980, (ii) to assess volumetric and seasonal changes in GGS discharge using decadal analysis, and (iii) to understand the climatic drivers influencing GGS discharge.

## 4.2 Study area and climate conditions

The study area consists of the GGS, which includes Meru (7 km$^2$), Raktavaran (30 km$^2$), Chaturangi (75 km$^2$) and the largest glacier Gangotri (140 km$^2$) (Figure 4.1). The GGS forms the headwater of the upper Ganga basin and contributes to the streamflow of the Bhagirathi River in the central Himalaya. It was selected due to its hydrological and regional importance within the Ganga basin, where comprehensive assessments of long-term melt partitioning and its climatic controls remain limited despite extensive prior studies. This study considers the discharge measurement site at Bhojbasa (30.95ºN, 79.05ºE; ~3800 m a.s.l.) as the discharge outlet (Figure 4.1). GGS covers an area of 549 km$^2$, between the elevation range 3767 and 7072 m a.s.l. (Figure 4.1). GGS has 48% glacierized area (~264 km$^2$) as per GAMDAM glacier inventory (Sakai, 2019), among which ~23% is debris covered area (Scherler et al., 2018). GGS receives precipitation from the WDs during winter (October to April) and from ISM during summer (May to September) (Singh et al., 2005; Arora et al., 2024). The average seasonal rainfall (May to October) is around 260 mm, with an average mean temperature of 9.4 °C for the period 2000–2003 (Singh et al., 2005; Arora et al., 2024).

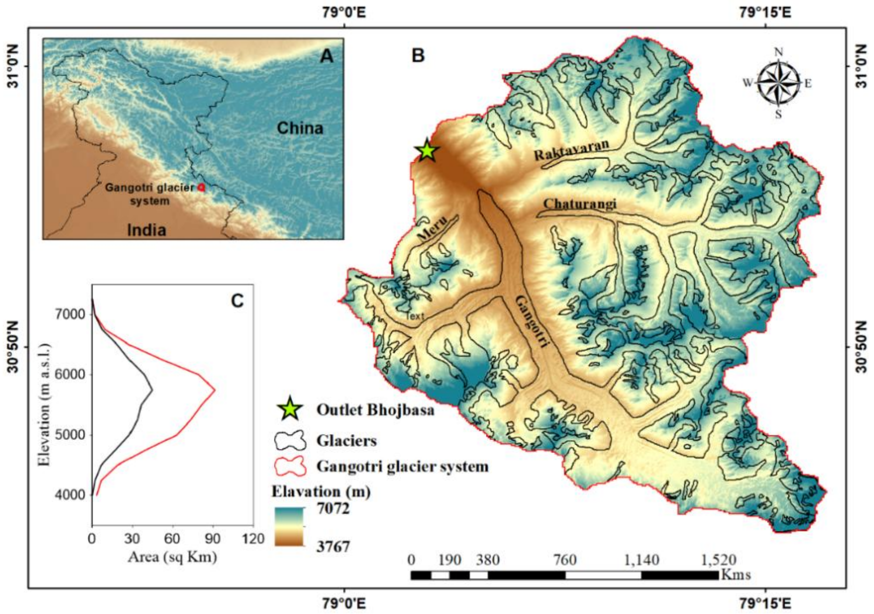

Figure 4.1 Study area (A) Country boundaries, (B) Gangotri Glacier System with the discharge measurement site at Bhojbasa (green star), and glaciers from the GAMDAM inventory shown in black; and (C) Area-altitude distribution of glacier area (black) and total area (red) in the GGS.

## 4.3 Dataset

### 4.3.1 Meteorological data

The Indian Monsoon Data Assimilation and Analysis (IMDAA) reanalysis gridded precipitation and temperature data were downloaded from the National Centre for Medium Range Weather Forecasting (NCMRWF) database over 1979–2020 (https://rds.ncmrwf.gov.in/dashboard/download). IMDAA is a regional atmospheric reanalysis dataset available at a 12 × 12 km spatial resolution since 1979, covering the Indian subcontinent (Rani et al., 2021). It assimilates a significantly larger set of Indian observations, of which some had not been used in any previous reanalysis, through a 4D-Var system and demonstrates improved representation of orographic precipitation, monsoon onset and withdrawal, and mesoscale convective systems (Rani et al., 2021). The IMDAA reanalysis accurately captures key features of ISM. IMDAA data has been used for different purposes, such as discharge modelling, drought assessment, and climate trend analysis over the Himalaya in the last few years, including a study specifically focused on GGS, demonstrating its suitability for high-altitude hydrological modelling (Singh et al., 2023; Gupta et al., 2024; Ahmed et al., 2024). IMDAA data was preferred in this study due to its high spatial resolution (12 km) and its specific development for the Indian subcontinent, making it more suitable for hydrological studies compared to coarser resolution global reanalysis products. The hourly IMDAA temperature and precipitation data were aggregated from hourly to daily resolution for the model simulations. These raw data were bias-corrected using in-situ temperature and precipitation measurements recorded at Bhojbasa from May to October during 2000–2003 (Figure 4.1; (Singh et al., 2005). For bias correction, a linear regression equation was developed between the mean monthly values of raw IMDAA data and in-situ data for the period 2000–2003 and derived the monthly scale factors for temperature as well as precipitation. These factors were then used to bias-correct the raw IMDAA temperature and precipitation data over 1980 to 2020.

### 4.3.2 In-situ discharge data

The in-situ daily discharge data was available from May to October at the Bhojbasa site in GGS over 2000–2003 (Figure 4.1; (Singh et al., 2005)). Discharge was measured using the area velocity method. The cross-section area of the channel was determined with the help of sounding rods at the beginning of the melt season and was rechecked at the end, while flow velocity was measured using wooden floats (Haritashya et al., 2006).

## 4.4 Methodology

### 4.4.1 Spatial Processes in Hydrology (SPHY) model

The Spatial Processes in Hydrology (SPHY) model is a spatially distributed, raster-based hydrological model designed to simulate key processes such as snow and glacier melt, rainfall-runoff, evapotranspiration, soil moisture dynamics, and groundwater recharge (Terink et al., 2015). SPHY is written in the Python programming language using the PCRaster dynamic modelling framework (Terink et al., 2015). The model can operate at different temporal and spatial scales. The model comprises different modules, including glacier, snow, groundwater, dynamic vegetation, simple routing, and lake/reservoir routing (Terink et al., 2015), which can be activated or deactivated based on study area requirements.

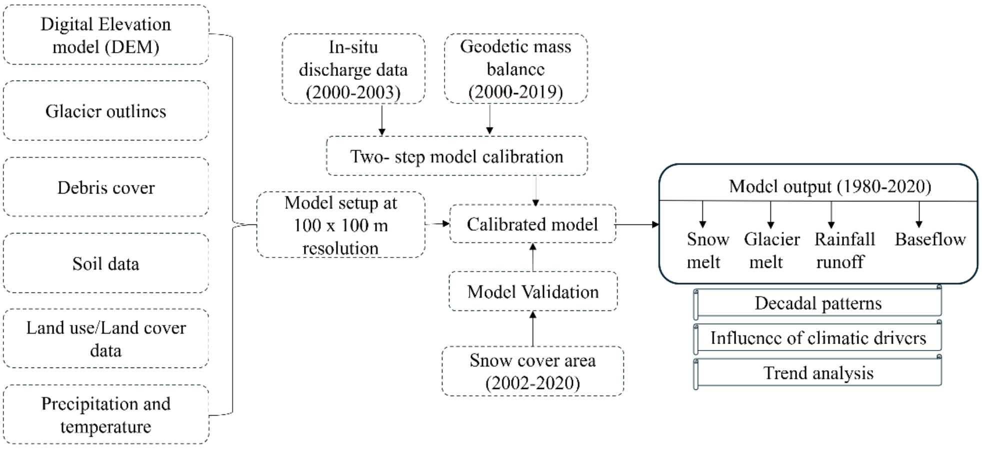

Figure 4.2 Flowchart showing the overall methodology, including input data, model setup, calibration and validation for glaciohydrological modelling.

The SPHY model uses a degree day approach to simulate discharge from snowmelt and glacier melt, making it suitable for data-scarce regions with limited long-term field measurements (Terink et al., 2015). To determine the liquid or solid form of precipitation, SPHY uses a critical temperature ($T_{crit}$). The precipitation phase is assigned as solid (snowfall) if the daily mean temperature in a cell is less than $T_{crit}$, otherwise, it is classified as rainfall (eq. 4.1).

$$\begin{cases} P_{snow} = P_{total}, P_{rain} = 0 \ \text{ if } \ T_{avg} \leq T_{crit} \\ P_{rain} = P_{total}, P_{snow} = 0 \ \text{ if } \ T_{avg} > T_{crit} \end{cases} \tag{4.1}$$

Where $P_{snow}$ (mm) is the precipitation as snowfall, $P_{rain}$ (mm) is the precipitation as rainfall, $T_{avg}$ (°C) is the mean air temperature, and $T_{crit}$ (°C) is the critical temperature threshold for precipitation to fall as snow.

When simulating discharge, rainfall and snowfall are handled differently. Snowfall contributes to snow storage, which is updated based on accumulation, melt and refreezing. Rainfall is partially transformed into surface runoff depending on the losses through infiltration, with infiltrated water contributing to baseflow depending on soil properties.

For glacier melt, SPHY distinguishes between clean ice and debris-covered ice, which melt at different rates. Multiple studies across glacierized regions have shown that despite slower melt rates, debris-covered glaciers can have similar mass loss due to the presence of features such as ice cliffs and supraglacial lakes (Buri et al., 2016; Miles et al., 2016; Hussain et al., 2022). In GGS, Gangotri Glacier exhibits such features in its lower ablation zone (4,000–4,750 m a.s.l.), contributing an additional 32% to ablation (Hussain et al., 2022). In SPHY, it is not possible to apply a different degree day factor for debris ($DDF_{debris}$) for different glaciers or at different elevation zones since it is a grid-based model. Hence, the same $DDF_{debris}$ and degree day factor for clean ice ($DDF_{ice}$) was calibrated and applied to all glaciers within GGS. However, a sensitivity test was performed for the selected $DDF_{debris}$ (section 4.4.4).

The snowmelt and glacier melt are calculated based on degree day factors, for which the following equations are used (Hock, 2003) (eq. 4.2):

$$\mathrm{Melt} = \begin{cases} \mathrm{T_{avg}} * \mathrm{DDF_{snow/ice/debris}} & \text{if } \mathrm{T_{avg}} > 0 \\ 0 & \text{if } \mathrm{T_{avg}} \leq 0 \end{cases} \tag{4.2}$$

Where $DDF_{snow/ice/debris}$ is the degree day factor for snow, clean ice and debris, respectively and $T_{avg}$ is the average daily temperature.

The SPHY model simulates soil water processes by dividing the soil into three layers: the root zone, subzone, and groundwater layer (Terink et al., 2015). Since SPHY operates on a daily time step, it does not capture short-term rainfall intensity variations and therefore, emphasizes the saturation excess runoff process (Hewlett, 1961) rather than the Hortonian runoff (Corradini et al., 1998; Beven, 2004). Lateral flow is modelled where slopes are steep and soils are permeable, occurring only when water content exceeds field capacity (Beven, 1981; Beven and Germann, 1982; Sloan and Moore, 1984). Water moves stepwise from the root zone to the subzone and groundwater layer, similar to the SWAT model (Neitsch et al., 2009).

Groundwater recharge, which may include glacier melt, often faces delays influenced by groundwater depth and soil properties, modelled using an exponential decay weighting function (Venetis, 1969; Sangrey et al., 1984).

To calculate the total discharge for each cell, various discharge components are combined (Figure 4.2) (eq. 4.3). These components include snowmelt ($Q_S$), Glacier melt ($Q_G$), rainfall-runoff ($Q_R$), and baseflow ($Q_B$). Rainfall-runoff is calculated as the sum of surface runoff and lateral flow from the first soil layer. The total discharge ($Q_T$) is calculated using the following equation:

$$Q_T = Q_S + Q_G + Q_R + Q_B \tag{4.3}$$

To obtain discharge at the outlet, $Q_T$ is routed through a flow direction network map (Terink et al., 2015). This map is generated using PCRaster in combination with DEM, which helps in delineating the river network accurately. Additionally, the model requires a glacier table that includes details about the initial glacier thickness and specifies whether a particular model cell is debris-covered or not to calculate glacier melt, including both clean ice and debris-covered ice. Most existing studies have suggested that a 250 m spatial resolution is suitable for obtaining reasonable modelling results in large-scale analysis across the HK region (Singh et al., 2021b; Srivastava et al., 2024). However, a coarser resolution may lead to the omission of small glacierized areas, especially when they occupy only a fraction of a grid cell, potentially resulting in the underestimation of glacier extent. Using a finer resolution not only offers more detailed outputs but also enhances the accuracy of the analysis by more precisely capturing smaller glaciers. Therefore, the model was run at a spatial resolution of 100 m × 100 m to reduce such limitations (Figure 4.2).

## 4.4.2 SPHY model inputs

SPHY model involves several raster data layers such as digital elevation model (DEM), land use/land cover (LULC), soil maps and glacier maps at a spatial resolution of 100× 100 m (Figure 4.3). Most of the input layers used in this study were derived from remote sensing products, which offer high-resolution, spatially continuous data essential for initializing glaciohydrological model in data-scarce region such as the GGS. The Shuttle Radar Topographic Mission

(SRTM) DEM (30m) was used in GlabTop2 model to calculate the initial ice depth. The GAMDAM glacier inventory was used for the glacier map developed by (Sakai, 2019). LULC layers were derived from the Globe Cover land cover map for the year 2009, created by the European Space Agency (ESA) (https://www.esa.int/ESA_Multimedia/Images/2010/12/ESA_s_2009_global_land_cover_map) (Figure 4.3). A high-resolution soil map (250 m²) and related parameters from HiHydroSoil version 1.2 (2016) (http://soilgrids1km.isric.org/) were used (Figure 4.3). The debris cover map was derived from supraglacial debris cover Geo Forschungs Zentrum (GFZ) data services (Scherler et al., 2018) for the preparation of glacier table and to differentiate a cell as debris covered or debris free.

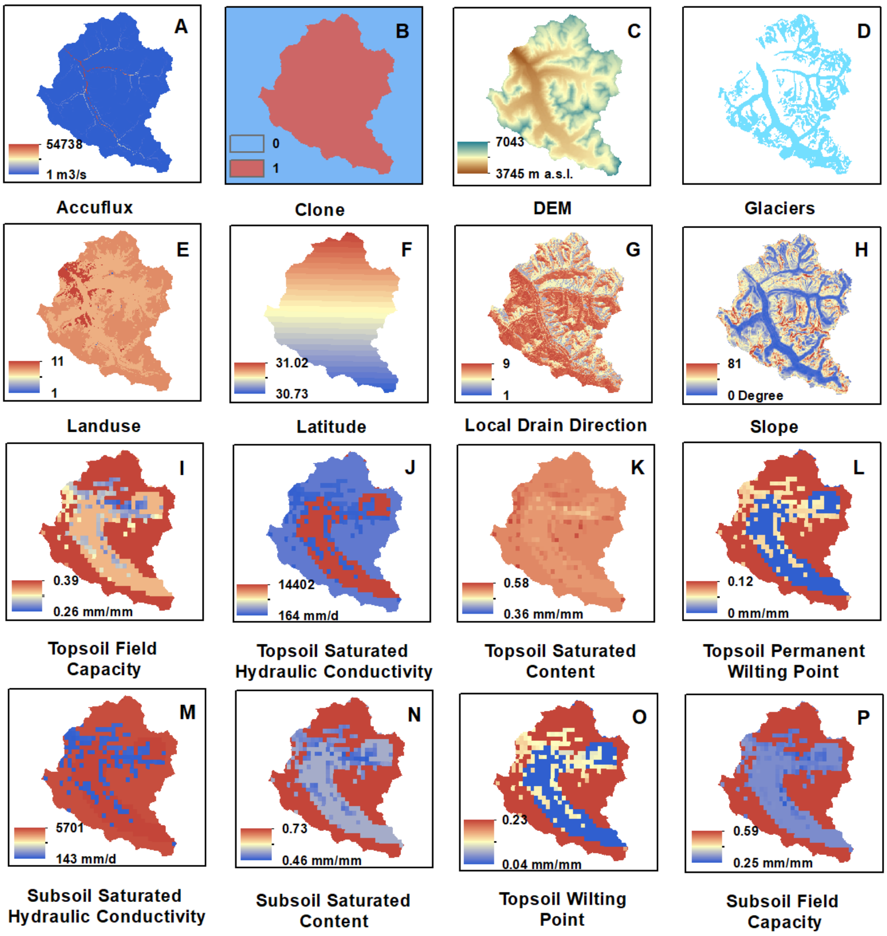

Figure 4.3 Input raster maps for SPHY model at 100m spatial resolution.

### 4.4.3 Model Calibration

In the SPHY model, both automatic and manual calibration could be performed (Terink et al., 2015). The automatic calibration was applied in the present study. The SPHY model parameters were altered within the plausible ranges, as mentioned in Table 4.1. The model parameters were calibrated using a two-tier approach using in-situ discharge over 2000–2003 and geodetic mass balance over 2000–2019 for GGS (section 4.4.3.1 and 4.4.3.2), the geodetic mass balance offered a broader calibration period and reinforced the two-tier calibration approach.

To check the performance of the model, the model calibration was done by considering the different performance criteria such as coefficient of determination ($R^2$) (eq. 4.4), root mean square error (RMSE) (eq. 4.5), percentage bias (PBIAS) (eq. 4.6), Nash–Sutcliffe model efficiency coefficient (NSE) (eq. 4.7) and Kling–Gupta efficiency (KGE) (eq. 4.8), which were calculated using the following equations:

$$R^2 = \left[\frac{\sum_{i=1}^{n}\{(O_i - O') * (S_i - S')\}}{\sqrt{\sum_{i=1}^{n}(O_i - O')^2 * \sum_{i=1}^{n}(S_i - S')^2}}\right]^2 \tag{4.4}$$

$$RMSE = \sqrt{\frac{\sum_{i=1}^{n}(O_i - S_i)^2}{n}} \tag{4.5}$$

$$PBIAS = \frac{\sum_{i=1}^{n}(S_i - O_i)}{\sum_{i=1}^{n} O_i} * 100 \tag{4.6}$$

$$NSE = 1 - \frac{\sum_{i=1}^{n}(O_i - S_i)^2}{\sum_{i=1}^{n}(O_i - O')^2} \tag{4.7}$$

$$KGE = 1 - \sqrt{(r-1)^2 + (\alpha - 1)^2 + (\beta - 1)^2} \tag{4.8}$$

where n, $O_i$, $S_i$, O′, S′, r, α and β are the number of observations, in-situ value, modelled value, mean in-situ value, mean modelled value, Pearson correlation coefficient, term representing the variability of prediction errors and bias term, respectively. α is ratio of standard deviation of modelled and in-situ values ($\sigma_s$ / $\sigma_o$) and β is ratio of mean modelled value to mean in-situ value ( S′ / O′). $R^2$ lies between 0 to 1, NSE and KGE lie between $-\infty$ to 1.

#### 4.4.3.1 In-situ Discharge

The SPHY model parameters such as glacier melt runoff factor (GlacF), rootzone thickness, sublayer thickness, groundwater layer thickness, saturated ground water content, capillary rise, alphaG$_w$, deltaG$_w$ and recession coefficient were calibrated using the in-situ daily discharge available at the Bhojbasa site for GGS over 2000–2003 (May to October) (Figure 4.3). The modelled daily discharge of GGS showed a good agreement with the in-situ daily discharge at Bhojbasa after calibration over 2000–2003 (May to October) ($R^2$ = 0.77, RMSE = 31.68 $m^3/s$, PBIAS = −2.88%, NSE = 0.61 and KGE = 0.51; Figure 4.4).

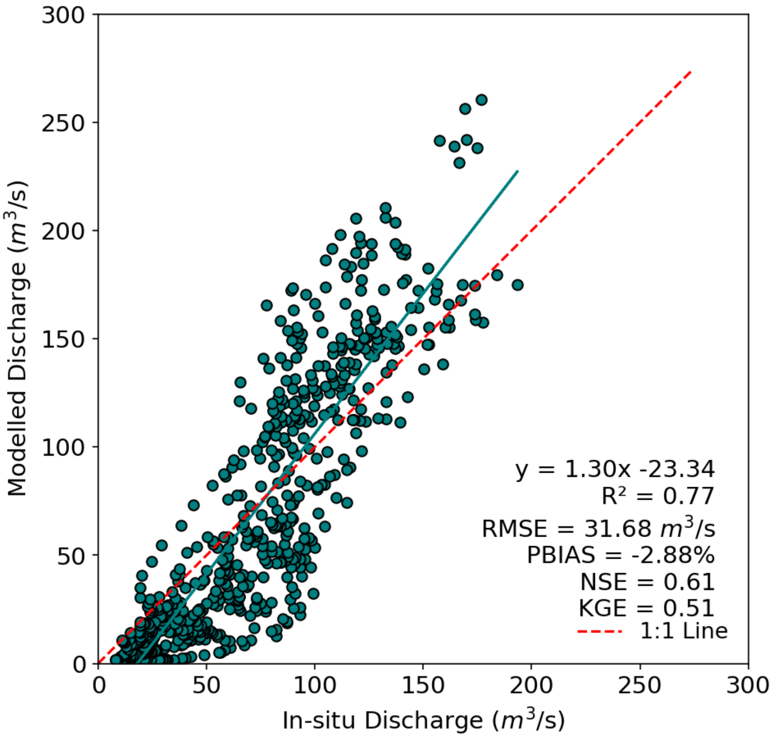

Figure 4.4 Regression plot between the daily in-situ and modelled discharge over the period 2000–2003 for GGS.

### 4.4.3.2 Geodetic mass balance

Geodetic mass balance represents glacier-wide mass change, derived by differencing DEMs to estimate glacier thickness change which is then converted to mass using standard density assumptions (Cogley, 2009; Huss, 2013). These estimates provide spatially distributed, temporally integrated measurements of glacier mass changes. However geodetic estimates are often available for a multi-annual scale hence do not provide inter-annual variability

(Cogley, 2009). These estimates are particularly valuable for model calibration in data-scarce regions like Himalaya (Zemp et al., 2009; Gardner et al., 2013). In this study, high-resolution, bias-corrected geodetic mass balance data from (Hugonnet et al., 2021) were used for Gangotri Glacier over 2000–2019 to calibrate the SPHY model. The latest version of SPHY, version 3, used in the present study includes glacier dynamics. It provides the annual ice thickness change, from which the glacier annual mass balances can be calculated (Khanal et al., 2021). After calibrating some of the model parameters of snow and glacier module with in-situ discharge (section 4.4.3.1), the rest of the model parameters such as snow storage capacity (SSC), the critical temperature for snow/rain ($T_{crit}$), degree day factor for snow ($DDF_{snow}$), degree day factor for ice ($DDF_{ice}$) and degree day factor for debris ($DDF_{debris}$) were calibrated with the available geodetic mass balances for the four different periods, i.e. 2000–2004, 2005–2009, 2010–2014 and 2015–2019 from (Hugonnet et al., 2021) of Gangotri Glacier (Figure 4.3). While calibrating, these model parameters were varied within the plausible ranges mentioned in Table 4.1. The calibrated model parameters are selected when the difference between the geodetic mass balance and modelled mass balances was minimal over 2000–2019 (Table 4.1). After calibration, the difference between the geodetic mass balance and modelled mass balance were 0.09, 0.05, −0.03 and 0.05 m w.e. for 2000–2004, 2005–2009, 2010–2014 and 2015–2019, respectively, with a mean difference of 0.04 m w.e. over 2000–2019 for Gangotri Glacier.

### 4.4.4 Model Validation

The SPHY model was validated against the improved 8-day MODIS snow cover product (ICIMOD, 2023) over the period 2002–2020 on a monthly scale (Figure 4.2). The improved MODIS snow cover product was generated using MODIS Terra and Aqua 8-day snow cover products MOD10A2 and MYD10A2 collection 6.1 (C61), respectively for High Mountain Asia and is freely available at ICIMOD regional database system (https://rds.icimod.org/DatasetMasters/BulkDownload/1973819). The data is available at 8-day temporal resolution and 500 m spatial resolution over the period 2002–2022 (ICIMOD, 2023). This product was generated by reducing the overestimation caused by MODIS sensors and underestimation caused by cloud cover in MODIS snow cover products (Muhammad and Thapa, 2020). The mean monthly snow cover area (%) i.e. the percentage of GGS area covered with snow, was extracted from the improved MODIS snow cover maps and SPHY derived snow cover maps over 2002–2020 for validation (Figure 4.5). The monthly comparison between the SPHY derived and improved MODIS snow cover (%) showed good agreement ($R^2$ = 0.79, RMSE = 12.75%, PBIAS = 12.33%, NSE = 0.65 and KGE = 0.62; Figure 4.5).

Table 4.1 Model parameters used in the SPHY model for the Gangotri Glacier System with its range, sensitivity range, uncertainty range, calibrated values and sensitivities.

| Parameters | Parameter range | Calibrated value | Uncertainty range | Sensitivity range | Sensitivity ($m^3/s$) |
|---|---|---|---|---|---|
| Snow storage capacity (SSC) | 0–1 | 0.05 | 0.045–0.055 | 0.045–0.055 | −0.22 |
| Degree day factor for snow ($DDF_{snow}$) (mm/d/ºC) | 2.5–8 | 5.6 | 5.04–6.16 | 5.04–6.16 | 1.48 |
| Degree day factor for clean ice $DDF_{ice}$ (mm/d/ºC) | 2.5–8 | 7.7 | 6.93–8.47 | 6.93–8.47 | 0.04 |
| Degree day factor for snow $DDF_{debris}$ (mm/d/ºC) | 2.5–8 | 4.8 | 4.32–5.28 | 4.32–5.28 | 0.05 |
| Critical temperature for snow/rain $T_{crit}$ (ºC) | −4 to 4 | 1.5 | 0.35–1.65 | 0.5–2.5 | −3.55 |
| Glacier melt runoff factor (GlacF) | 0–1 | 0.81 | 0.72–0.89 | 0.72–0.89 | 0.02 |
| root zone thickness (mm) | 300–1000 | 817 | 735–899 | 735–899 | −0.01 |
| sublayer thickness(mm) | 1000–2000 | 1932 | 1739–2125 | 1739–2125 | −0.01 |
| groundwater layer thickness(mm) | 1000–4000 | 2697 | 2427–2967 | 2427–2967 | 0.00 |
| saturated groundwater content(mm) | 500–3000 | 1303 | 1173–1433 | 1173–1433 | −0.003 |
| Capillary rise max (mm/day) | 2–10 | 6.2 | 5.58–6.82 | 5.58–6.82 | 0.00 |
| $alphaG_w$ | 0.1–1 | 0.9 | 0.81–0.99 | 0.81–0.99 | 0.00 |
| $deltaG_w$ (days) | 0–365 | 320 | 288–352 | 288–352 | −0.003 |
| Recession coefficient | 0.5–1 | 0.85 | 0.77–0.94 | 0.77–0.94 | −0.003 |

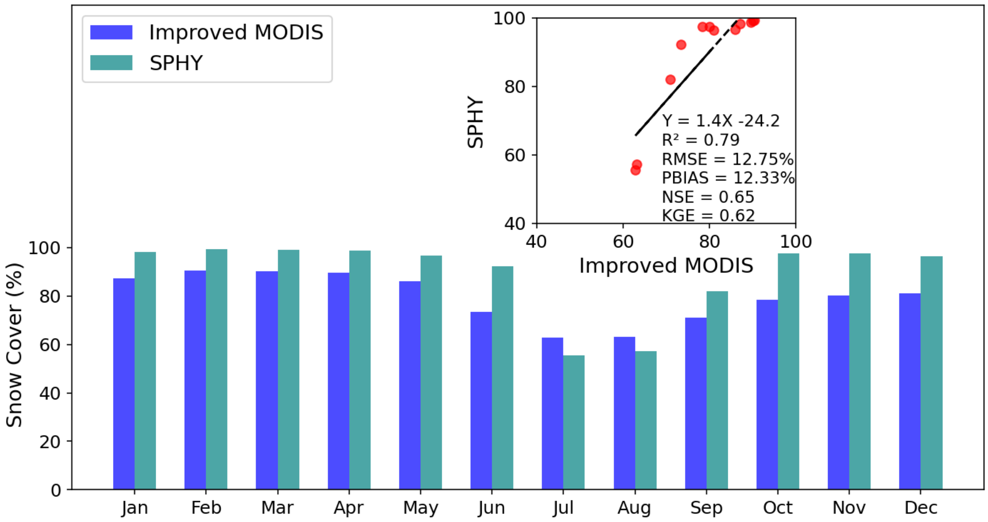

Figure 4.5 Comparison between the monthly snow cover % derived from SPHY and improved Snow cover product (ICIMOD, 2023). The inset figure is a regression plot between SPHY and improved MODIS snow cover %.

The SPHY modelled annual mass balances of Gangotri Glacier (section 4.4.3.2) were also compared with available annual mass balance estimates derived using the temperature index model in (Hussain et al., 2022) over 2000–2019. The comparison between the SPHY and temperature-index modelled annual mass balances showed a moderate agreement ($R^2$ = 0.40, RMSE = 0.57 m w.e.). The mean modelled annual mass balance was −0.50 m w.e. compared to −0.90 m w.e. reported by (Hussain et al., 2022) over 2000–2019. This difference can be attributed in part to the more detailed hydrological processes represented in the SPHY model, including refreezing and geometry changes, which were not included in the simplified modelling approach adopted by (Hussain et al., 2022). Another reason for the discrepancy lies in the two different values of $DDF_{debris}$ and $DDF_{ice}$ used in the present study, which fail to account for the additional melt due to the supraglacial lakes and ice cliff present on Gangotri Glacier, as discussed in section 4.4.1. To assess the impact, a sensitivity experiment was conducted by using the same value for $DDF_{debris}$ and $DDF_{ice}$ across all glaciers in GGS. This led to an increase in the mean annual GGS discharge by 0.42 $m^3/s$ (1.5%) and a slightly more negative mean annual mass balance of Gangotri Glacier as −0.57 m w.e. (13%) over 2000–2019.

### 4.4.5 Uncertainty and sensitivity analysis

To evaluate the sensitivity of GGS discharge to the SPHY model parameters, sensitivity analysis was performed with a total of 14 parameters including SSC, GlacF, $T_{crit}$, $DDF_{snow}$, $DDF_{ice}$, $DDF_{debris}$, rootzone thickness, sublayer thickness, groundwater layer thickness, saturated ground water content, capillary rise, $alphaG_w$, $deltaG_w$ and recession coefficient. The sensitivity was estimated by running the model at each 10% increase and decrease in parameter values except $T_{crit}$ while keeping other model parameters constant. For $T_{crit}$, the parameter values increased and decreased by 1ºC to evaluate sensitivity. One-At-a-Time (OAT) approach for sensitivity analysis was selected for its computational efficiency and interpretability in the context of a high-dimensional glaciohydrological model (Heynen et al., 2013). The ±10% perturbation range is consistent with previous studies (Ragettli et al., 2013; Azam et al., 2019; Srivastava et al., 2024). The sensitivity was calculated using the modelled GGS mean discharge over 1980–2020 and eq. 4.9 (Oerlemans et al., 1998).

$$s = \frac{Q_{TH} - Q_{TL}}{2} \tag{4.9}$$

Here, s is the sensitivity of each parameter, $Q_{TH}$ and $Q_{TL}$ are the GGS mean discharge over 1980–2020 at the highest (+10%) and lowest (−10%) values of parameters. The sensitivities were estimated over the period 1980–2020.

For the uncertainty estimation, each calibrated model parameter was altered by ±10% of its calibrated value and the uncertainty was estimated using the error propagation law as follows (Heynen et al., 2013; Ragettli et al., 2013):

$$u = \sqrt{\sum_{1}^{n} \left(\frac{Q_{TH} - Q_{TL}}{2}\right)^2} \tag{4.10}$$

Here, u is the overall uncertainty in the modelled discharge, n is the number of parameters and $Q_{TH}$ and $Q_{TL}$ are the same as mentioned in the sensitivity estimation above.

## 4.5 Results

### 4.5.1 Annual discharge

The mean annual discharge from the GGS was computed using the daily modelled $Q_T$ to understand the interannual variability over 1980–2020 (Figure 4.6). The annual $Q_T$ varies from 18.9 ± 1.4 $m^3/s$ in 2015 to 35.9 ± 2.4 $m^3/s$ in 2010 with a mean annual $Q_T$ of 28 ± 1.9 $m^3/s$ for GGS over 1980–2020 (Figure 4.6). The highest annual $Q_T$ in 2010 corresponds to the second highest annual temperature (4ºC) associated with higher precipitation (585 mm) (Figure 4.6). Though the annual temperature in 2009 was maximum (4.2ºC) but due to the reduced precipitation (446 mm), it results in less annual $Q_T$ as compared to 2010 (Figure 4.6).

Each discharge component showed different interannual variability with the mean annual $Q_S$, $Q_G$, $Q_R$, and $Q_B$ as 18.0, 5.7, 3.1 and 1.1 $m^3/s$, respectively, for GGS over 1980–2020. Overall, among all the discharge components, $Q_S$ contributes the major portion (64%) to $Q_T$ followed by $Q_G$ (21%), $Q_R$ (11%) and $Q_B$ (4%) over 1980–2020 (Figure 4.7). Despite being the dominant contributor, $Q_S$ showed less interannual variability compared to $Q_G$ (Figure 4.6). $Q_S$ varies from 11.6 $m^3/s$ in 2016 to 22.6 in 2005, whereas $Q_G$ varies from 1.1 $m^3/s$ in 2015 to 12.6 $m^3/s$ in 2001 (Figure 4.6). $Q_G$ contribution was maximum in 2001, because of the reduced annual precipitation (492 mm) and increased annual temperature (3.4 ºC) for GGS (Figure 4.6). Interestingly, $Q_G$ was low in 2009 despite similar low precipitation (446 mm) and even higher temperature (4.2 ºC). This contrary result is attributed to higher early summer temperature in 2001, which triggered more rapid snowmelt and led to earlier exposure of glacier ice. The extended duration of exposed ice during summer in 2001 likely contributed to increased icemelt compared to 2009. $Q_R$ contribution was maximum in 2016 because of the higher annual temperature (3.9 ºC), resulting in a large portion of precipitation as rainfall (Figure 4.6). $Q_B$ showed a minimal interannual variability for GGS over 1980–2020 (Figure 4.6).

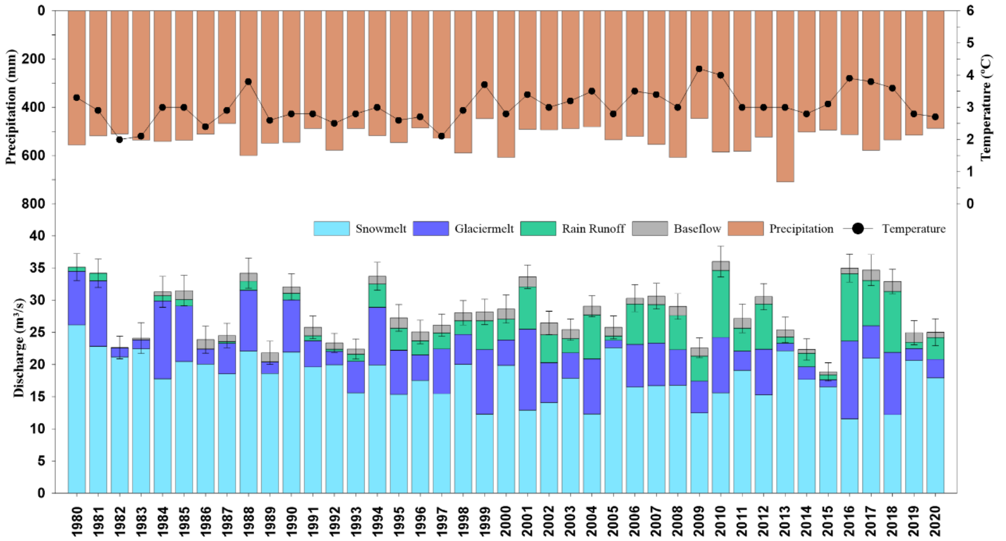

Figure 4.6 Annual discharge variability of different discharge components over 1980–2020, snowmelt (sky blue), Glacier melt (blue), rainfall-runoff (green), baseflow (grey) with annual precipitation (brown) and temperature (black line). The annual discharge uncertainties are shown with black error bars.

### 4.5.2 Monthly and seasonal discharge patterns

The mean monthly $Q_T$ varies from 0.9 to 129.9 m$^3$/s with an average monthly discharge of 28 m$^3$/s for GGS over 1980–2020 (Figure 4.7). $Q_T$ shows a significant increase from April and then peaks in July (129.9 m$^3$/s) (Figure 4.7). Similarly, $Q_S$ starts increasing in May and peaks in July, similar to $Q_T$ (99.1 m$^3$/s) (Figure 4.7). Whereas $Q_G$ starts increasing in June when the snow line reaches higher elevations and peaks in August (33.4 m$^3$/s) (Figure 4.7). In GGS, $Q_R$ contribution starts increasing from June with the onset of monsoon in this area and peaks in August (19.2 m$^3$/s), similar to $Q_G$ (Figure 4.7). There is minimal variability in mean monthly $Q_B$ with a maximum contribution in September and October (1.6 m$^3$/s), probably a delayed response of percolation of glacier meltwater and monsoonal rains during the melt season (June through September) (Figure 4.7). The average monthly $Q_S$, $Q_G$, $Q_R$ and $Q_B$ are 18.0 m$^3$/s, 5.7 m$^3$/s, 3.1 m$^3$/s and 1.1 m$^3$/s, respectively, for GGS over 1980–2020 (Figure 4.7).

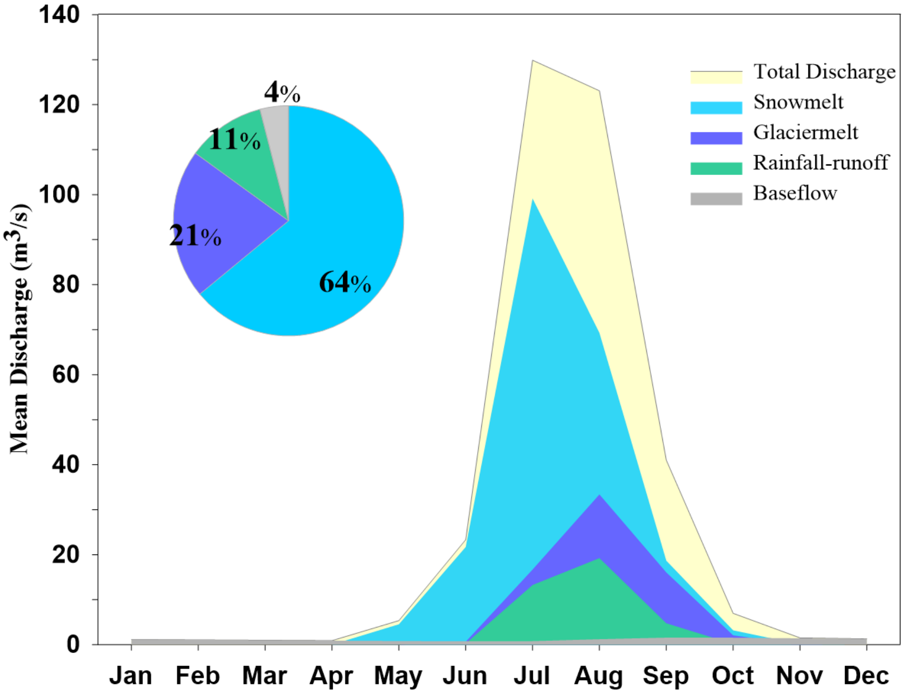

Figure 4.7 Mean monthly variability of different discharge components for GGS over 1980–2020. The pie chart shows the percentage contribution of each discharge component.

The seasonal discharge patterns on GGS were analyzed by considering two major seasons, summer (May–October) and winter (November–April). $Q_T$ is maximum during summer (54.9 m$^3$/s) while minimum during winter (1.1 m$^3$/s) for GGS over 1980–2020 (Figure 4.7). $Q_S$, $Q_G$ and $Q_R$ showed a similar seasonal pattern as $Q_T$, with maximum contribution in summer (36.1, 11.5 and 6.3 m$^3$/s, respectively) and negligible contribution in winter (Figure 4.7). $Q_B$ does not show any seasonal pattern, as its contribution is almost the same in summer and winter (Figure 4.7).

### 4.5.3 Decadal discharge patterns

41 years of modelled discharge data was analysed in four decades i.e., 1980–1990, 1991–2000, 2001–2010 and 2011–2020 to explore the decadal discharge pattern in GGS (Figure 4.8). $Q_S$ contribution to $Q_T$ decreased from 1980–1990 (73%) to 2001–2010 (52%) but increased again in 2011–2020 (63%), very similar to the variation in winter precipitation over the four decades in GGS (Figure 4.8). $Q_G$ contribution was almost the same (~22%) in 1980–1990, 1991–2000 and 2001–2010, whereas it decreased to 16% in the last decade

2011–2020 (Figure 4.8). The sudden increase in $Q_S$ and decrease in $Q_G$ in 2011–2020 is mainly caused by reduced winter temperature (−2ºC) and increased winter precipitation (262 mm), leading to high snow accumulation in winter which subsequently melts in summer as temperature increases (Figure 4.8). $Q_R$ contribution has significantly increased from 2% (1980–1990) and 9% (1991–2000) to 22% and 17% in 2001–2010 and 2011–2020, respectively, due to the increase of 0.5 ºC in the mean temperature over 2001–2020 as compared to 1980–2000 in GGS (Figure 4.8). The significant increase in $Q_R$ was also associated with the increased summer precipitation in 2001–2020 (293 mm) as compared to 1980–2000 (272 mm) and reduced average $Q_S$ in 2001–2020 (57.5%) as compared to 1980–2000 (69%) (Figure 4.8). $Q_B$ contribution showed a very small decadal change over the four decades from 3% to 5% for GGS (Figure 4.8). Similar observations of decreasing $Q_S$ with increasing $Q_R$ were also documented in the previous studies in the other part of HK (Lutz et al., 2014; Khanal et al., 2021). It was observed that the decadal $Q_T$ varies from a minimum of 26.8 $m^3/s$ in 1991–2000 to a maximum of 28.9 $m^3/s$ in 2001–2010, corresponding to the highest mean decadal temperature of 3.4ºC in 2001–2010 (Figure 4.8). $Q_T$ showed the highest volumetric increase of 7.8% corresponding to the highest increase in summer precipitation and temperature rise from 1991–2000 to 2001–2010 (Figure 4.8). The positive association between temperature increase resulting in an increased discharge, is consistent with trends observed across HK (Lutz et al., 2014).

The monthly decadal discharge showed a distinct pattern in 1980–1990 as compared to the last three decades on GGS (Figure 4.8). In 1980–1990, the monthly $Q_T$ peaks in August due to the increased $Q_S$ in August corresponding to the highest winter precipitation over 1980–1990 (264 mm) in GGS (Figure 4.8). In the last three decades (1991–2000, 2001–2010, 2011–2020), the peak in monthly $Q_T$ occurred in July (Figure 4.8). Results showed a shift in discharge peak post-1990 from August to July (Figure 4.8). Unlike other months, in August $Q_S$ contribution has significantly decreased from 70% in 1980–1990 to 54% in 1991–2000 and 41% in 2001–2010, then again increased to 57% in 2011–2020 (Figure 4.8). This reduction in $Q_S$ during August occurred because of the increased early summer temperature and reduced winter precipitation from 1980–1990 to 2001–2010 (Figure 4.8). There was no shift observed in the monthly decadal $Q_G$ peaks over 1980–2020 for GGS (Figure 4.8). There is a significant increase in $Q_R$ contribution in July to September in the last two decades as compared to 1980–2000 due to the increased summer precipitation associated with higher temperature (Figure 4.8).

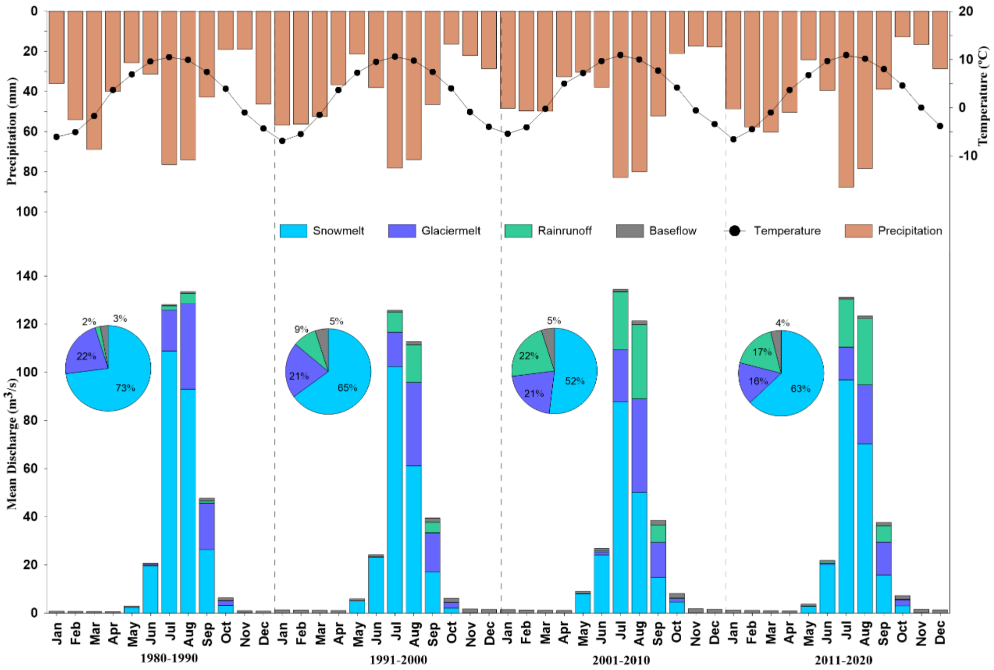

Figure 4.8 Decadal discharge variability and contribution of different discharge components over 1980–2020, snowmelt (sky blue), Glacier melt (blue), rainfall-runoff (green) and baseflow (grey) with precipitation (brown) and temperature (black). Pie charts show the percentage contribution of different discharge components.

## 4.6 Discussions

### 4.6.1 Climatic drivers for GGS discharge

To understand the influence of climate drivers, i.e. precipitation and temperature on GGS discharge, the correlation coefficients (r) were calculated between the climate drivers, discharge and its different components over 1980–2020 (Figure 4.9).

Despite $Q_S$ being the dominant contributor to $Q_T$, the annual $Q_G$ showed strong control over annual $Q_T$ ($r = 0.81$), suggesting that GGS discharge variability was primarily governed by changes in $Q_G$ rather than $Q_S$, whose variability was less aligned with $Q_T$. Additionally, annual $Q_T$ is also correlated with annual $Q_R$ (r = 0.57) (Figure 4.9). Summer $Q_T$ showed almost the same relationships as the annual $Q_T$ showing its dominant control over GGS discharge (Figure 4.9). Winter $Q_T$ showed the strongest correlation with the winter and summer $Q_B$ (r = 1 and 0.73, respectively) and weak correlation with winter $Q_S$ and winter $Q_G$ (r = 0.14 and 0.06, respectively), this indicates that GGS discharge in winter is mainly driven by $Q_B$ (Figure 4.9). Annual $Q_S$ showed a strong correlation with winter precipitation (WP) (r = 0.64) and moderate negative correlation with winter temperature WT (r = −0.47) (Figure 4.9), possibly because the study region receives almost equal amount of precipitation in winter but in the form of snowfall which further contributes to $Q_S$ when the temperature rises in summer. The inverse correlation with WT also reflects that colder winters favour greater snow retention, setting the stage for enhanced meltwater input during summer. It was also observed that annual $Q_G$ has a strong correlation with WP (r = −0.66), likely because reduced precipitation in winter (mostly snowfall) leads to increased $Q_G$ in summer (Figure 4.9). The negative relationship indicates that thick snow cover insulates glacier ice due to its high albedo and delays $Q_G$. In contrast, low snowfall years expose ice earlier, increasing $Q_G$ through greater solar absorption. Although $Q_R$ contributes less during winter, it showed a strong correlation with WT (r = 0.67), likely because small changes in temperature around $T_{crit}$ strongly influence precipitation phase (snow/rain) in this season. Overall, annual $Q_T$ showed a strong positive correlation with summer precipitation (SP) (r = 0.62) followed by WT (r = 0.52) as both of these climatic drivers influence annual $Q_G$ and $Q_R$. Similar control of SP was also observed on the hydrology of the Dokriani Bamak Glacier catchment belonging to the same region as GGS (Srivastava and Azam, 2022b).

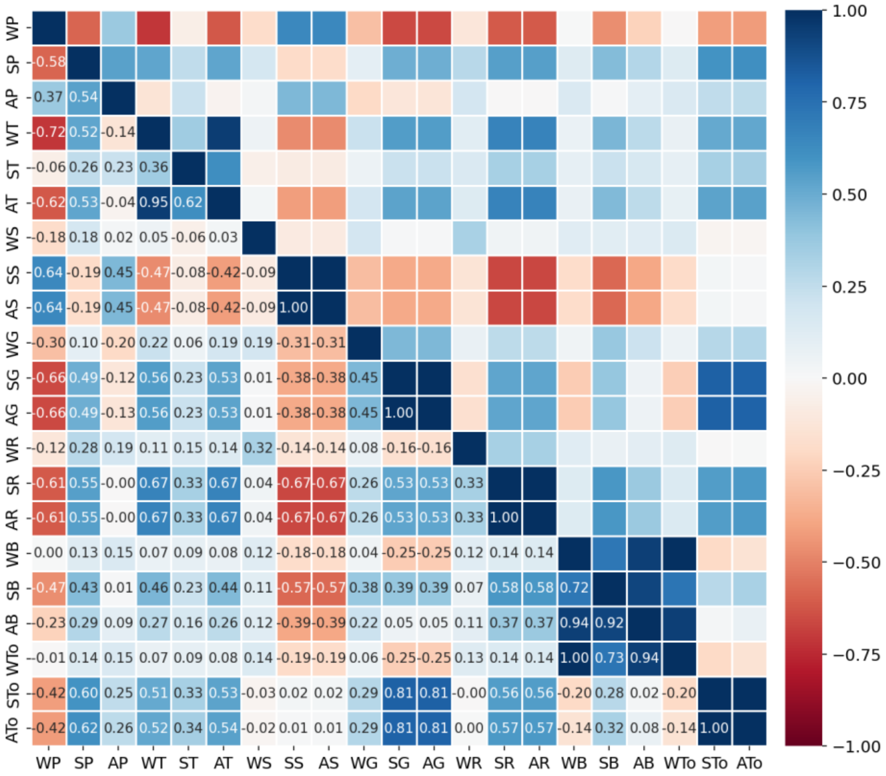

Figure 4.9 Correlation matrix for Gangotri Glacier System. The values from −1 to 1 denote the correlation coefficients (1 denotes the completely positive correlation, dark blue, and −1 denotes the completely negative correlation, dark brown). ATo, STo, and WTo = annual, summer, and winter discharge, respectively; AB, SB and WB = annual, summer and winter baseflow, respectively; AR, SR and WR = annual, summer and winter rainfall-runoff, respectively. AG, SG and WG = annual, summer and winter glacier melt, respectively; AS, SS and WS = annual, summer and winter snowmelt, respectively; AT, ST and WT = annual, summer and winter temperature, respectively; AP, SP and WP = annual, summer and winter precipitation, respectively.

### 4.6.2 Long-term trend analysis

The long-term $Q_T$, its different hydrologic components ($Q_S$, $Q_G$, $Q_R$ and $Q_B$), mean annual precipitation, temperature and snow cover area (%) were utilized to analyze the trends over 1980–2020 for GGS (Figure 4.10). For the trend analysis Men-Kendall test and Sen's slope estimator method were used (Mann, 1945; Kendall, 1948; Sen, 1968). The M-K test (Z value) assesses whether a significant trend exists, while Sen's slope estimator (Q value) quantifies the rate of change. These values define the trend only when the p-value is below 0.05 (95% confidence level), otherwise it suggests that no statistically significant trend is present.

The long-term trend analysis reveals key patterns in discharge, snow cover and temperature over 1980–2020 for GGS (Figure 4.10). $Q_T$ (Q-value = −0.006, Z-value = 0.010) does not show a statistically significant trend, however, the slightly negative Q value suggests a minor decrease in GGS discharge over 1980–2020, possibly because of the no significant trend observed in mean annual precipitation (Q-value = 0.262, Z-value = −0.013) (Figure 4.10). Similarly, $Q_G$ (Q-value = −0.037, Z-value = −0.095) shows no significant trend, but the small negative Q and Z values indicate a slight decrease in $Q_G$ over 1980–2020 (Figure 4.10). In contrast, $Q_S$ is significantly decreasing (Q-value = −0.134, Z-value = −0.327), likely due to rising temperature trend (Q-value = 0.018, Z-value = 0.286) and reducing snow cover area (Q-value = −0.07, Z-value = −0.315) for GGS over 1980–2020 (Figure 4.10). The snow-covered area decreased by approximately 5% in 2020 compared to 1980. However, it exhibits considerable interannual variability, with some years showing the increase in snow cover, rather than a uniform decrease. $Q_R$ (Q-value = 0.149, Z-value = 0.471) and $Q_B$ (Q-value = 0.015, Z-value = 0.202) exhibit a significantly increasing trend (Figure 4.10), suggesting possible shifts in precipitation patterns and hydrological responses on GGS.

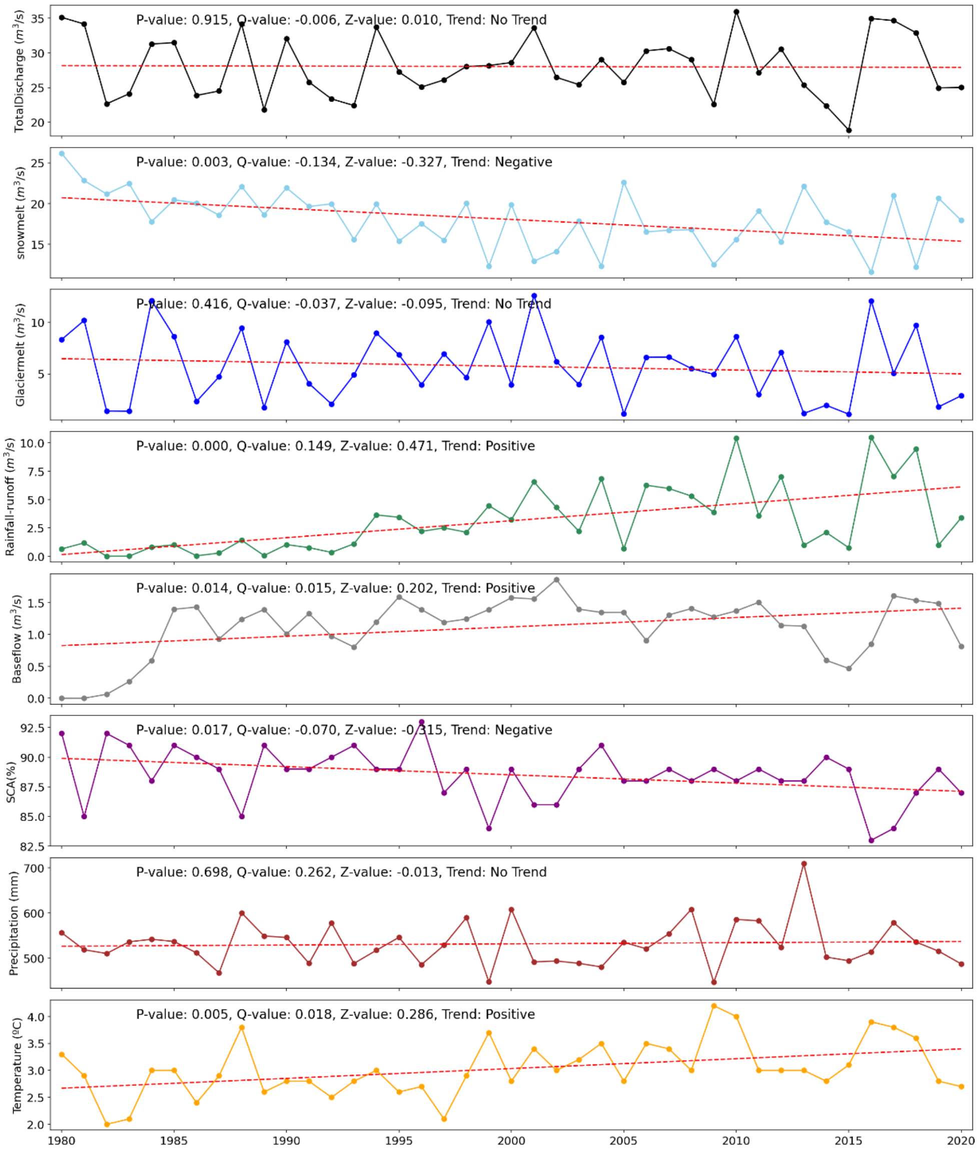

Figure 4.10 Observed trend in temperature (orange), precipitation (brown), snow cover area (SCA) (purple), total discharge (black), snowmelt (sky blue), glacier melt (blue), rainfall-runoff (green) and baseflow (grey) for GGS over 1980–2020.

Similar to these trends, previous studies also observed that the increase in $Q_R$ and $Q_B$ is offset by a significant decrease in $Q_S$ in the Himalaya (Lutz et al., 2014; Khanal et al., 2021). Importantly, the mean annual temperature displays a significant positive trend (Q-value = 0.018, Z-value = 0.286), aligning with broader warming patterns in the Himalaya (Kumar et al., 2011; Immerzeel et al., 2012; Nepal and Shrestha, 2015; Srivastava et al., 2024) (Figure 4.10). These findings suggest that increasing temperature and decreasing snow cover are influencing different components of GGS discharge. Although higher temperature on GGS would typically enhance snowmelt, the significant concurrent reduction in snow cover on GGS is limiting snowmelt, while on the other hand, increasing rainfall-runoff on GGS over 1980–2020.

### 4.6.3 Sensitivity of discharge parameters

The sensitivity analysis for GGS revealed that the $T_{crit}$ and $DDF_{snow}$ exhibited the highest sensitivity, with a sensitivity of −3.5 $m^3/s$ and 1.48 $m^3/s$, respectively, corresponding to ±1ºC and ±10% change in $T_{crit}$ and $DDF_{snow}$, respectively (Table 4.1). SSC also showed a higher sensitivity of −0.22 $m^3/s$, emphasizing a significant influence on $Q_T$ whereas $DDF_{debris}$, $DDF_{ice}$ and GlacF exhibited moderate sensitivities of 0.05 $m^3/s$, 0.04 $m^3/s$ and 0.02 $m^3/s$ (Table 4.1). In line with the present study, the previous studies on hydrological models also found $DDF_{snow,}$ $T_{crit}$, SSC, $DDF_{debris}$ and $DDF_{ice}$ are among the most sensitive model parameters (Azam et al., 2019; Fatima et al., 2020; Srivastava et al., 2024). The parameters related to subsurface flow, such as root zone thickness, sublayer thickness, groundwater layer thickness, and saturated groundwater content, showed relatively low sensitivities, indicating a lesser impact on immediate discharge response (Table 4.1).

### 4.6.4 Comparison with the other studies

The results from previous studies on GGS were compiled to assess the reliability of modelled discharge in the present study (Table 4.2). The findings indicate that snowmelt remains the primary contributor to discharge, followed by glacier melt, rainfall-runoff and baseflow (Table 4.2). Similar results were documented in previous studies on GGS (Singh et al., 2008; Rai et al., 2019; Singh et al., 2023; Arora et al., 2024) (Table 4.2).

A previous study by (Lutz et al., 2014) applied the SPHY model to simulate discharge in HMA basins over 1998–2007, and the results are freely available (ICIMOD, 2021). The results for GGS were extracted and the mean discharge reported by (Lutz et al., 2014) is twice (56 $m^3/s$) as compared to present study (28 $m^3/s$) (Table 4.2). The reason for this could be the different spatial resolution of the model used in both the studies and that the model by (Lutz et al., 2014) was not calibrated at the glacier-catchment scale using field measurements. In the present study, the calibration with the in-situ discharge measurement at the nearest outlet (Bhojbasa) resulted in significantly better modelled discharge estimates. Another reason could be the high resolution (0.12° × 0.12°) precipitation and temperature data used in the present study compared to the coarse resolution (0.5° × 0.5°) data used in (Lutz et al., 2014).

GGS mean discharge observed in the present study (27.7 $m^3/s$) showed a small difference compared to the results in (Singh et al., 2023) (38.1 $m^3/s$) over 2012–2020, this small difference could be attributed by the different datasets and time period considered for the model calibration (Table 4.2). The monthly and seasonal discharge patterns observed in the present study are similar to the monthly patterns reported in the previous studies on GGS (Rai et al., 2019; Singh et al., 2023). The maximum annual discharge was observed in 2010 which was also reported by (Salim and Pandey, 2021).

Table 4.2 Estimates of different discharge components from previous studies on Gangotri Glacier System.

| Catchment | Time period | Model/ technique | Mean discharge ($m^3/s$) | Snowmelt (%) | Glacier melt (%) | Rainfall-runoff (%) | Baseflow (%) | References |
|---|---|---|---|---|---|---|---|---|
| Gangotri | 2000–2004 | SNOWMOD | – | 97 (combined) |  | 3 | – | (Singh et al., 2008) |
| Gangotri | 1998–2007 | SPHY | 56 | 7 | 73 | 10 | 10 | (Lutz et al., 2014) |
| Gangotri | 2012–2020 | SPHY | 38.1 | 52 | 27 | 17 | 3 | (Singh et al., 2023) |
| Gangotri | 2013–2019 | HBV | – | 56 | 30 | 15 | – | (Arora et al., 2024) |
| Gangotri | 2005 | Isotopes | – | 60 | 36 | 4 | – | (Rai et al., 2019) |
| Gangotri Glacier System | 1980–2020 | SPHY | 28 | 64 | 21 | 11 | 4 | Present study |

### 4.6.5 Uncertainties and limitations

The modelled GGS discharge exhibit a few uncertainties, which are important to consider while interpreting the results. The main source of uncertainty arises from the sensitivity of SPHY model parameters. These uncertainties were systematically assessed by error propagation law (section 4.4.5; Figure 4.6). The average uncertainty in the modelled discharge was ±1.9 $m^3/s$, with inter annual variability ranging between ±1.4 and ±2.4 $m^3/s$ over 1980–2020. Additionally, the differences in glacier area estimates between the different glacier inventories are also a source of uncertainty in the glaciohydrological model output. Importantly, understanding and quantifying these uncertainties enhances confidence in the modelled discharge and allows for more informed interpretation. It also enables more accurate projections of future water resources. Such insights are particularly valuable for strategic planning in glacier-fed basins under evolving climate scenarios.

While the reconstructed discharge provided valuable insights, the study has few limitations, which can guide future research. A major limitation of the SPHY model is that it does not include the losses due to sublimation, which impacts the total discharge of a glacierized catchment. Including sublimation in future model developments could improve the representation of glacier melt, particularly in arid and high-altitude zones (Azam et al., 2021). Another key limitation of the SPHY model is its inability to assign glacier- or elevation-specific $DDF_{debris}$ values due to its grid-based setup. This leads to uniform $DDF_{debris}$ across all glaciers in GGS, overlooking enhanced melt from supraglacial lakes and ice cliffs present on the Gangotri Glacier. Incorporating dynamic debris parameterization could significantly overcome this issue. While equifinality is an inherent limitation in hydrological models, efforts were made in this study to minimize its impact. For this, a two-tier calibration approach was adopted using in-situ discharge and geodetic mass balance, supported by validation against improved snow cover product (Section 4.4.3, 4.4.4). Although there are some uncertainties and limitations, the use of high-resolution meteorological datasets, two-tier calibration approach enhanced the reliability of modelled discharge for GGS.

## 4.7 Conclusions

The long-term glaciohydrological studies focusing on climatic drivers influencing long-term discharge are limited in HK. The present study addresses this research gap by providing a comprehensive assessment of the long-term discharge and control of climatic drivers on the hydrology of GGS from 1980–2020. The contributions from snowmelt, glacier melt, rainfall-runoff and baseflow were quantified by reconstructing GGS discharge spanning over four decades (1980–2020) using high-resolution SPHY model, combined with remote sensing datasets. The two-tier calibration using geodetic mass balance and field discharge data, along with validation using improved MODIS snow cover area, significantly increased the SPHY model reliability for simulating discharge. The findings indicate that snowmelt is the dominant contributor to GGS discharge, accounting for 64% of the mean annual GGS discharge (28 ± 1.9 $m^3/s$). Glacier melt contributed 21%, while rainfall-runoff and baseflow contributed 11% and 4%, respectively. The highest annual discharge was observed in 2010 with the lowest in 2015 on GGS over 1980–2020. The monthly discharge starts increasing in April and peaks in July in GGS. The decadal analysis showed that the maximum decadal discharge (28.9 $m^3/s$) was observed in 2001–2010 corresponds to the highest decadal temperature (3.4 ºC) over four decades (1980–2020) in GGS. The decadal mean discharge showed the highest volumetric increase of 7.8% from 1991–2000 to 2001–2010 on GGS. Decadal analysis showed a shift in peak discharge to July post-1990. Statistical analysis revealed that the hydrology of GGS is mainly controlled by the summer precipitation, which regulates the interannual variability of GGS discharge, despite snowmelt being the primary contributor. This is primarily due to summer snowfall, which increases surface albedo, suppresses melt during peak ablation even under high temperature, and thus significantly impacts annual discharge. Long-term trend analysis indicates an increasing trend in mean annual temperature with a decreasing trend in snow cover area, resulting in a decreasing trend of snowmelt on GGS over 1980–2020. Conversely, rainfall-runoff and baseflow have exhibited increasing trends on GGS, suggesting warming-induced hydrological changes. Sensitivity analysis revealed that $T_{crit}$ and $DDF_{snow}$ are the highest sensitive parameters to GGS discharge over 1980–2020. The findings underscore the urgent need for continued field monitoring and modelling efforts to enhance water resource management strategies in glacier-fed river basins. Future research should focus on integrating high-resolution climate projections and remote sensing datasets to improve discharge predictions under the changing climate in HK.

# Chapter 5

# Improved snowline extraction method

## 5.1 Introduction

Glaciers in High Mountain Asia are critical water resources for downstream communities, yet their response to climate change remains challenging to monitor (Armstrong et al., 2019; Azam et al., 2021). The Himalaya-Karakoram (HK) region contains thousands of glaciers, but only a tiny fraction (38 glaciers, ~0.09%) are monitored in the field (Vishwakarma et al., 2022). This paucity of in-situ data limits our understanding of glacier changes in these rugged, heterogeneous terrains (Bolch et al., 2019). Equilibrium line altitude (ELA) is a key indicator of glacier health, defined as the elevation where annual accumulation equals ablation; mass balance is zero (Braithwaite and Raper, 2009; Cuffey and Paterson, 2010). Year-to-year fluctuations in ELA reflect shifts in climate (primarily temperature and precipitation). Continuous ELA monitoring is thus crucial for calibrating glacio-hydrological models and reconstructing mass balance variations (Azam et al., 2021; Srivastava and Azam, 2022b). However, in-situ estimation of ELA using the traditional glaciological method (stake networks and snow pits) is laborious and often challenging on glaciers in remote, high-altitude areas. However, ELA estimates can be sensitive to the accuracy of digital elevation models and glacier outlines (Braithwaite and Raper, 2009; Oien et al., 2022). In regions like the Himalaya, researchers often rely on remote sensing snowline altitude (SLA) as a proxy for the ELA. The highest SLA at the end of the ablation season ($SLA_{max}$) is expected to correspond closely to the ELA (Rabatel et al., 2012).

Over the past two decades, remote sensing techniques for extracting glacier snowlines have advanced considerably (Pelto, 2011; Huss, 2013; Mernild et al., 2013; Tawde et al., 2016; Rabatel et al., 2017). Early studies relied on manual delineation of the snowline by visual inspection (Rabatel et al., 2016; Barandun et al., 2018; Chandrasekharan et al., 2018). Semi-automated algorithms have since leveraged band ratios and spectral indices (e.g., NIR/SWIR) for classification, using either fixed thresholds (Rastner et al., 2015; Racoviteanu et al., 2019) or adaptive thresholding methods like Otsu algorithm (Rastner et al., 2019; Liu et al., 2021). Multi-step classification approaches incorporating albedo, slope, or elevation have also been used (Lei et al., 2012; Naegeli et al., 2019; Barandun et al., 2021). Platforms like Google Earth Engine have enabled scalable SLA mapping (Liu et al., 2021; Loibl et al., 2025), and machine learning methods are also developed (Li et al., 2012; Prieur et al., 2022).

Despite these advances, SLA detection remains challenging due to deep shadows, crevasses, snow patches, steep terrain, and persistent cloud cover (Racoviteanu et al., 2019; Rastner et al., 2019). To mitigate such issues, various filtering techniques have been introduced: cloud cover thresholds, terrain masks, or filtering based on snow cover fraction (Racoviteanu et al., 2019; Prieur et al., 2022; Loibl et al., 2025). Some studies restrict SLA extraction to glacier flowlines (Rabatel et al., 2017; Davaze et al., 2020).

This chapter presents an improved semi-automated snowline extraction method implemented in Dudh Koshi basin. Our approach builds upon the method by Racoviteanu et al. (2019) and introduces a robust post-processing filtering procedure. The primary objectives are: (1) to improve a semi-automated SLA approach developed previously (Racoviteanu et al., 2019) by implementing it in Python, adapting it to Sentinel-2/Landsat 8 and adding post-processing filtering methods; (2) to validate the improved method using high-resolution Planet/Venµs images. The chapter also sets the foundation for analyzing the SLA-ELA relationship discussed in the next chapter by ensuring that the snowline data used are temporally consistent across the study area.

## 5.2 Study area

Our study area consists of the glacierized Dudh Koshi basin (~3711 km$^2$, 449 to 8761 m a.s.l.), located in the monsoon-dominated central Himalaya (Figure 5.1) (Thayyen and Gergan, 2010). ISM causes maximum precipitation (~80 % of the annual precipitation) during the summer months (June to September), Glaciers in these areas are referred to as “summer accumulation type glaciers” (Bookhagen and Burbank, 2010; Thayyen and Gergan, 2010). The simultaneous accumulation and ablation in this region introduce challenges to snowline detection, as SLAs are often indistinguishable due to cloud and/or temporary snow cover (Brun et al., 2015). During the summer, snowfall is frequent at higher elevations, while lower elevations may experience rainfall (Khadka et al., 2024). The post-monsoon period (October–November) marks a rapid shift to predominantly dry, sunny, and cooler weather, occasionally disrupted by typhoons that can bring heavy snowfall above 4000 m a.s.l. (Shea et al., 2015). The winter period (December–February) is characterized by even harsher conditions, with consistently cold, arid, and windy weather and minimal snowfall; any deposited snow is often blown away by strong westerly winds above 5000 m a.s.l. (Wagnon et al., 2013). During the pre-monsoon period (March–May), weather gradually becomes warmer and wetter, making this the second wettest season of the year (Khadka et al., 2022). The unique climatic setting and dynamic surface conditions, including wind-driven snow redistribution, sublimation, and temporary snow cover make it a highly dynamic system.

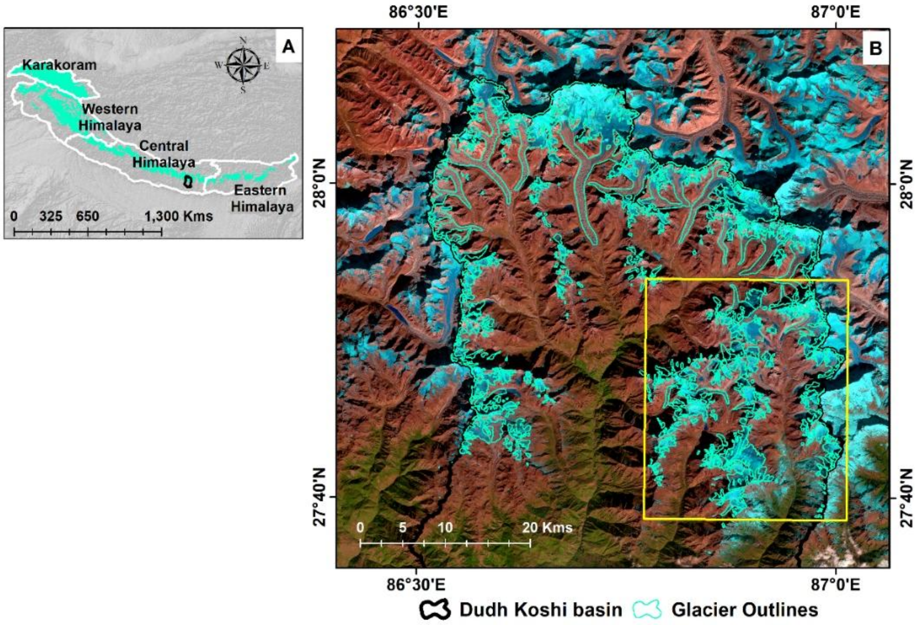

Figure 5.1 Study area showing the upper Dudh Koshi basin in the central Himalaya, with glaciers from the GAMDAM inventory shown in cyan (A, B). The yellow box shows the subset used for validation around the Hinku sub-basin (n = 177 glaciers) (B). The background image is a false color composite of the Sentinel-2 image (bands 11,8,4) from 14 Jan 2016 (B).

## 5.3 Datasets

### 5.3.1 Remote sensing data

To extract glacier SLAs, sub-monthly, multi-temporal data were used from Sentinel-2 (denoted hereafter as 'S2') and Landsat 8 ('L8') sensors for the period 2016–2022 (Table 5.1). For S2, collection 1 MSI Level-1C (L1C) data were obtained from Copernicus Open Access Hub, consisting of orthorectified Top-Of-Atmosphere (TOA) reflectance in cartographic geometry for 13 spectral bands, with 10 m spatial resolution in the visible (VIS) and 20 m in the shortwave infrared (SWIR) bands. For L8, collection 2, level-1 data were obtained from the United States Geological Survey (USGS, 2019), which consists of radiometrically calibrated and terrain-corrected (L1TP) data provided as scaled Digital Numbers (DN) for 11 bands, with 30 m pixel size in VIS to SWIR bands. Since L8 has only a 16-day revisit time, there were less available dates compared to S2 (5-day revisit time). For both sensors, cloud-free contrast images were selected from post monsoon October to December/January each year.  Atmospheric and topographic corrections were performed on all images using the open-access Atmospheric and Radiometric Correction of Satellite Imagery (ARCSI) software (Bunting and Clewley, 2018), based on the 6S (Second Simulation of a Satellite Signal in the Solar Spectrum) algorithm, which is a radiative transfer model (Vermote et al., 1997) (Figure 5.2A). This yielded the standardized surface reflectance for all the scenes, with deep shadows masked out as NoData.

High-resolution Planet and Venµs data (3–5 m) were used to validate the S2/L8-derived SLAs over the period 2016–2022. Images from Planet RapidEye (5 m)/PlanetScope (3 m) consist of multi-spectral data (five and four spectral bands, respectively, in the VIS/NIR) with a positional accuracy of < 10 m (PlanetLabs, 2021). Level 3A/B data were obtained, which comprises radiometrically-corrected, orthorectified surface reflectance computed from TOA radiance products using the 6S radiative transfer model (Vermote et al., 1997). The Venµs sensor acquired images with a two-day revisit time, 5 m spatial resolution and 12 narrow spectral bands (VIS to NIR) over the period 2017–2020 in our study area. VM1 (Venµs Mission 1) products from the first acquisition phase were freely accessed through the French CNES Theia website (https://www.theia-land.fr/en/blog/product/venus/). The Flat Reflectance (FRE) products were obtained, which consist of topographic and radiometric corrected data produced by CNES on the basis on L1C and L1A TOA reflectance (Theia-Land, 2022). Planet/Venµs images were used for the snowline validation, by selecting the images closest to the dates of the S2/L8 images (~1–2 days). A list of all images used and their specific details are provided in Table 5.1.

## 5.3.2 Glacier masks

For the entire Dudh Koshi basin, glacier outlines from the GAMDAM glacier inventory (Sakai, 2019) were used, constructed using semi-automated mapping of satellite imagery (Landsat ETM+ imagery from 1999–2003) and manual corrections. This inventory covers 425 km$^2$ of the Dudh Koshi basin, with a total of 462 glaciers. While there is a mismatch of ~10 years between the date stamp of these outlines and the period of our analysis, these were used only as a glacier mask, so this should not affect the SLA extraction routine as most glaciers have shrunk (Li et al., 2022). For the detailed validation of the

SLA method in the Hinku sub-basin, the glacier outlines were updated based on manual delineation on end-of-the ablation season Planet/Venμs satellite imagery from 2nd December 2020.

### 5.3.3 Elevation data

The ALOS Global Digital Surface Model (AW3D30 version 2.2, at 30 m) (Takaku and Tadono, 2017) was used for the topographic correction and SLA extraction. This DEM version contained fewer data voids and provided better shadow rendering in ARCSI in our study area, as reported by (Racoviteanu et al., 2021). The AW3D30 DEM was also has a high reported vertical accuracy of ~10 m in our study area (Tadono et al., 2014).

## 5.4 Methodology

### 5.4.1 Snowline extraction

This study builds on the method proposed by (Racoviteanu et al., 2019), which was improved here for a more accurate SLA extraction. Specifically, the shadowed area was automatically masked out and the Otsu method was used for automatically selecting distinct thresholds for every satellite image. The Otsu method is an unsupervised, histogram-based thresholding technique that determines an optimal threshold by maximizing between-class variance, enabling objective separation of two dominant pixel classes (Otsu, 1979). In snowline detection, these classes correspond to snow-covered and snow-free glacier surfaces with distinct reflectance characteristics. The method's image-specific threshold selection makes it well suited for automated SLA mapping from optical satellite imagery (Liu et al., 2021; Rastner et al., 2019). In the previous method by (Racoviteanu et al., 2019), shadows were masked using a single band ratio and the thresholds for surface partitioning were selected on the basis of visual inspection and prior knowledge (Figure 5.2A). The automated filtering step introduced in this study (Figure 5.2B) marks a key improvement over the previous method by addressing challenges such as shadows, crevasses, snow patches, etc., which often led to erroneous pixels in previous studies.

The SLA delimitation method used here consists of several steps implemented as conditional statements in Python (Figure 5.2) and applied over the entire Dudh Koshi basin (462 glaciers). The first part (Figure 5.2A) consists of separating snow and ice from the surrounding terrain using a fixed threshold based on literature, applied to a band ratio (NIR/SWIR > 1.5, S2: band 8/11, L8: band 5/6) (Racoviteanu et al., 2009, 2019), followed by NIR band thresholding automated using the Otsu method (Otsu, 1979) to separate snow from ice (Racoviteanu et al., 2019). Snow and ice areas were then buffered and intersected to extract “raw” snowlines as detailed in (Racoviteanu et al., 2019) (Figure 5.2A). In the second part, the raw SLAs were filtered to limit known outliers commonly found in both the ablation and accumulation areas of glaciers in previous studies (Racoviteanu et al., 2019) (Figure 5.2B). This consisted in: (a) applying a negative buffer of 100 m to the GAMDAM glacier outlines (Figure 5.2B); (b) applying a threshold between Q3 (third quartile) and Whislo (lower whisker) on a box plot, chosen on a trial-and-error basis (Figure 5.2B, C); and (c) applying a sieve filter on the binary image (SLA/non-SLA pixels) to further minimize common outliers in the accumulation/ablation areas (for example, the inclusion of false positives in the accumulation area). For the sieve filtering step, different thresholds were defined for each sensor (S2: 50 pixels and L8: 30 pixels); these thresholds were determined by several tests on glaciers of varying sizes (~2 to ~127 km$^2$) to capture isolated pixel groups of various sizes; (d) SLA extraction with the output binary image and DEM to yield the “final” SLAs at basin scale (Figure 5.2B). Glacier SLA were calculated as the mean elevation of all the pixels along the final snowline within the glacier boundary. Sub-basin-wide average SLA were calculated as an average of all glacier SLAs within the Hinku sub-basin.

### 5.4.2 Validation

The remote sensing S2 and L8 SLAs were validated in a subset of the Dudh Koshi basin, the Hinku sub-basin (177 glaciers), by comparing them with SLAs delineated manually on Planet/Venµs color composites (Planet: bands 4,3,2 and Venµs: bands 11,7,4). This was conducted as a double-blind experiment by a different analyst, independently of the semi-automated workflow. Both the semi-automated and the manually-delineated SLAs were extracted from the AW3D30 DEM using the 2020 Planet glacier mask. The mean SLAs were calculated from both datasets on a glacier-by-glacier basis and their means were compared from 13 common dates (±1 to 2 days) over the period 2016–2022. The accuracy of the semi-automated SLAs with respect to the Planet/Venµs SLAs was calculated as vertical root mean square error (RMSEz) and coefficient of determination ($R^2$). Two-sample t-tests were also performed to evaluate the differences in means between the two samples (S2/L8 vs. Planet/Venµs) and visually investigated outliers.

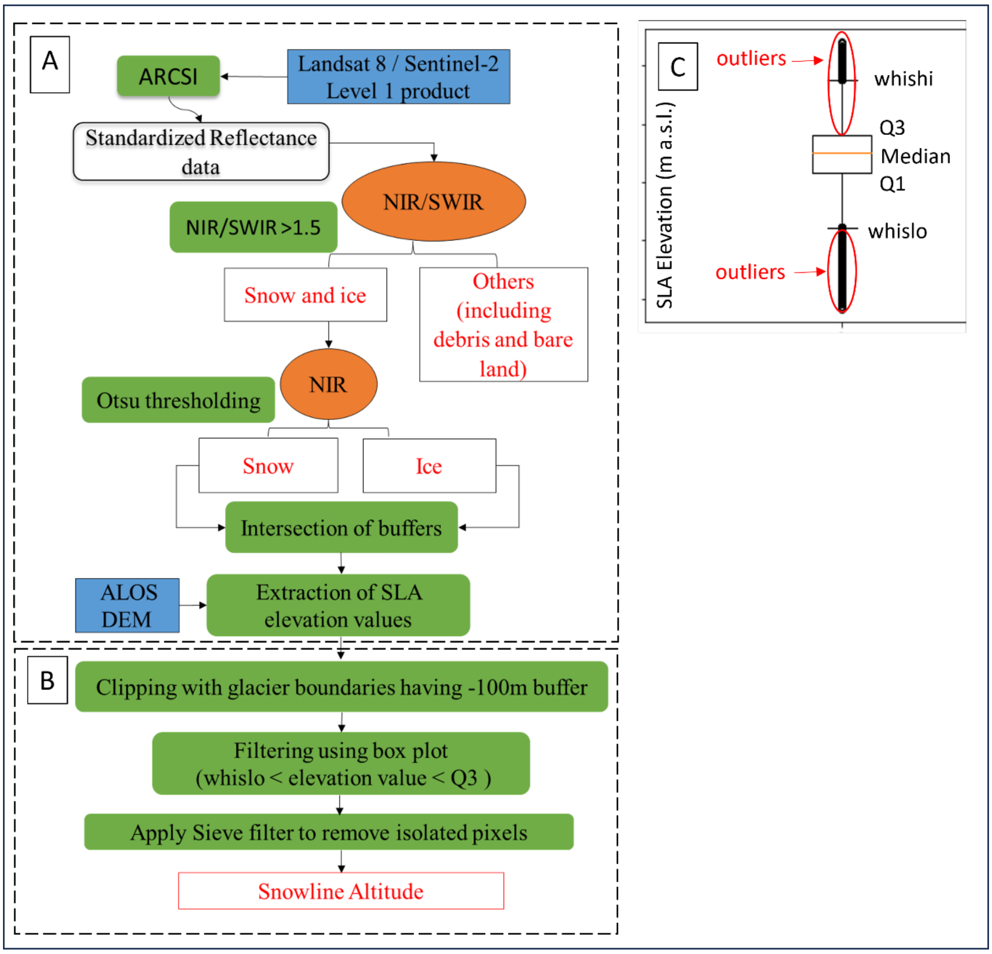

Figure 5.2 Flowchart showing the workflow of SLA extraction with all the inputs, outputs and their thresholds: raw SLA extraction using Otsu thresholding and buffer intersection (A), automated filtering to get final SLAs (B); box plot with thresholds (C). Here, Q1, Q3, whislo and whishi represent the first and third quartile, lowest whisker and highest whisker values, respectively.

## 5.5 Results

### 5.5.1 Performance of the snowline method

Initially, the raw SLAs exhibited outliers near the glacier ridgelines, crevasses, shadows and snow patches in the ablation area, etc. The filtering step (Figure 5.2B) allowed the removal of these outliers, an example shown with S2 and L8 images acquired four days apart (Figure 5.3). The outliers, initially present around the glacier ridgelines (white arrows in Figure 5.3A and 5.3C) were removed by the negative buffer applied to glacier boundaries. Similarly, the outliers with extreme elevation values in the accumulation areas, which fell outside the 100 m buffer from the ridgeline, were removed using the box plot filtering (green arrow in Figure 5.3C). The remaining isolated outliers were removed by sieve filtering (yellow arrow in Figure 5.3A). Most of the outliers/erroneous pixels were successfully removed, resulting in more reliable and clearer SLAs (Figure 5.3B, D).

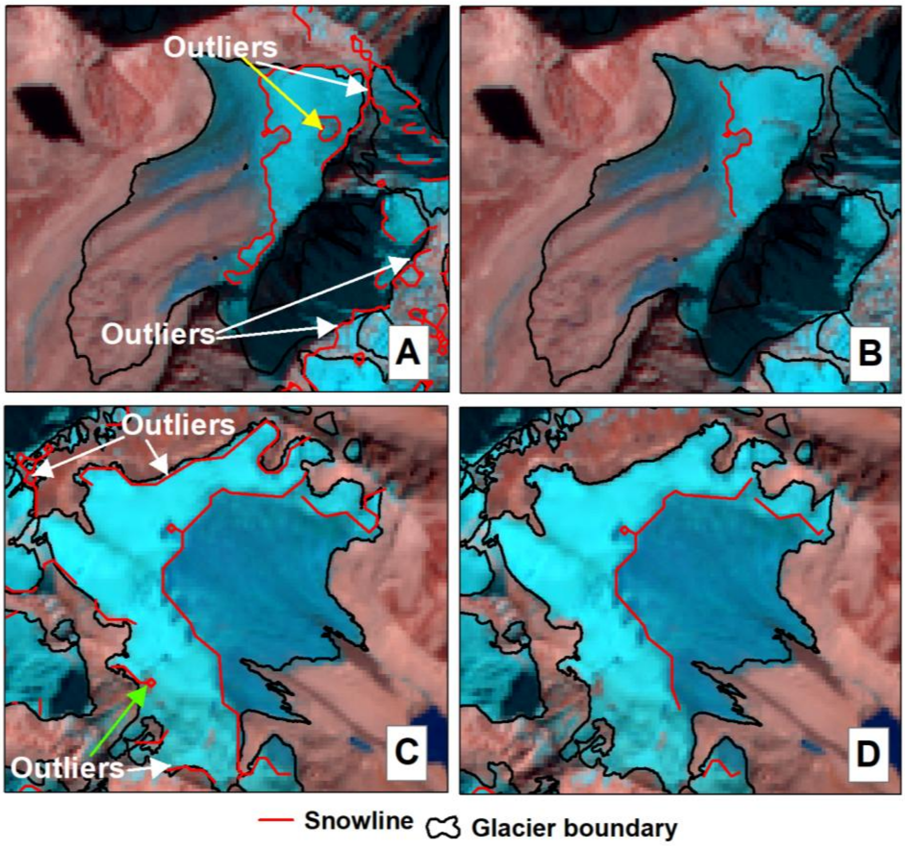

Figure 5.3 Illustration of the SLA filtering step showing raw SLAs (panels A, C) and the final SLAs (panels B, D) on two randomly selected glaciers in the Hinku sub-basin for S2 (top row, 20 Oct 2018, bands 11,8,4) and L8 (bottom row, 24 Oct 2018, bands 6,5,4). Arrows point to outliers near glacier ridgeline (white) at high elevations (green) and isolated pixels (yellow).

### 5.5.2 Validation with high-resolution data at sub-basin scale

For the Hinku sub-basin, final sub-monthly sub-basin-wide average SLA over 2016–2022 are shown in Table 5.1. Sub-basin-wide average SLA was lowest in 2016 (5484 m) and highest in 2018 (5645 m) (Table 5.1), with a mean of 5575 m over the period 2016–2022. Since the extent of the Planet scenes varied annually depending on acquisitions, only 381 glacier SLAs out of the total 1143 glacier SLAs, extracted from S2/L8 over the period 2016–2022 could be compared with the manually-delineated Planet/Venµs SLAs in the Hinku sub-basin (Table 5.1). This correlation was poor in the case of raw SLAs (non-filtered) ($R^2 = 0.41$, RMSEz = 188.8 m) (Figure 5.4A). However, a good agreement was found between filtered S2/L8 SLAs and the manually-delineated Planet/Venµs SLAs ($R^2 = 0.80$, RMSEz = 61.3 m) over 2016–2022 (Figure 5.4B). The year-by-year comparison of final SLAs from S2/L8 vs. manually delineated SLAs from Planet/Venµs shows variability in $R^2$, ranging from 0.65 in 2016 to a best fit of 0.90 in 2020 (Figure 5.5). This may illustrate the variability in surface conditions, as it will be discussed later in the discussion section. The means of the two sets of samples (S2/L8 final SLAs vs. Planet/Venµs) differed by only a few meters (Table 5.1). The differences were not statistically significant based on the two-sample t-test assuming unequal variances ($p > 0.05$, df = 791, where df denotes the degree of freedom).

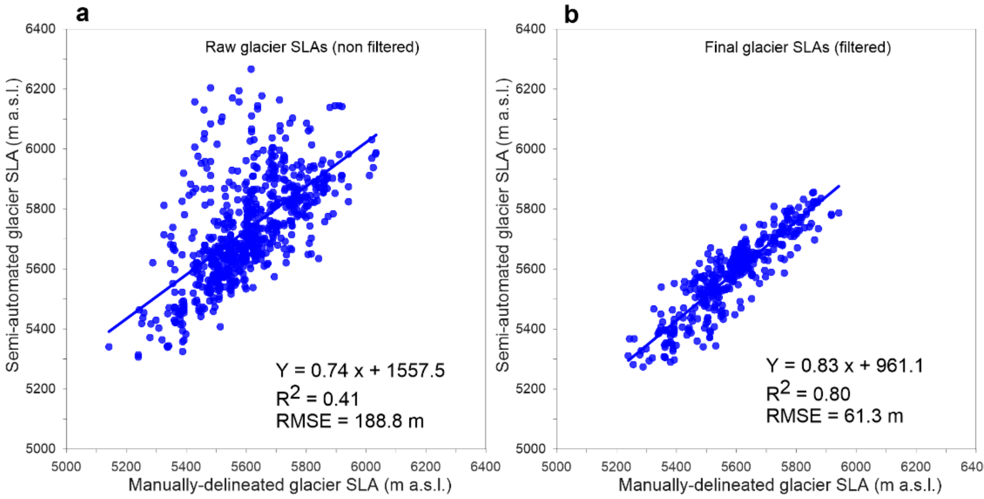

Figure 5.4 Regression between the semi-automated S2/L8 glacier SLAs and the manually-delineated Planet/Venµs glacier SLAs before and after automated filtering over the period 2016–2022.

Table 5.1 Summary statistics for S2/L8 sub-basin-wide average SLAs over the Hinku sub-basin (177 glaciers) and validation with manually-delineated sub-basin-wide average SLAs from Planet/Venµs images (denoted here as PS/VE) ± 1–2 days over the period 2016–2022

| Date | # SLAs | $SLA_{S2/L8}$ (m) | $SLA_{PS/VE}$ (m) | mean diff (m) | RMSEz (m) | $R^2$ |
|---|---|---|---|---|---|---|
| 2016-01-14 | 34 | 5592 | 5610 | 18 | 68.8 | 0.8 |
| 2016-11-19 | 14 | 5484 | 5494 | 10 | 82.9 | 0.7 |
| 2016-12-09 | 26 | 5543 | 5574 | 31 | 71.4 | 0.8 |
| 2016-12-29 | 28 | 5545 | 5585 | 40 | 88.4 | 0.7 |
| 2017-12-09 | 32 | 5604 | 5608 | 4 | 45.0 | 0.9 |
| 2017-12-29 | 37 | 5604 | 5602 | 2 | 50.0 | 0.9 |
| 2018-10-20 | 39 | 5610 | 5590 | 20 | 57.5 | 0.8 |
| 2018-10-24 | 17 | 5548 | 5570 | 22 | 65.2 | 0.6 |
| 2018-11-24 | 39 | 5614 | 5605 | 9 | 42.8 | 0.9 |
| 2018-11-25 | 21 | 5645 | 5619 | 26 | 51.1 | 0.9 |
| 2019-12-04 | 33 | 5557 | 5556 | 1 | 60.4 | 0.8 |
| 2020-12-03 | 32 | 5598 | 5593 | 5 | 40.5 | 0.9 |
| 2022-12-08 | 29 | 5548 | 5562 | 14 | 64.6 | 0.9 |
| Mean |  | 5575 | 5579 |  |  |  |

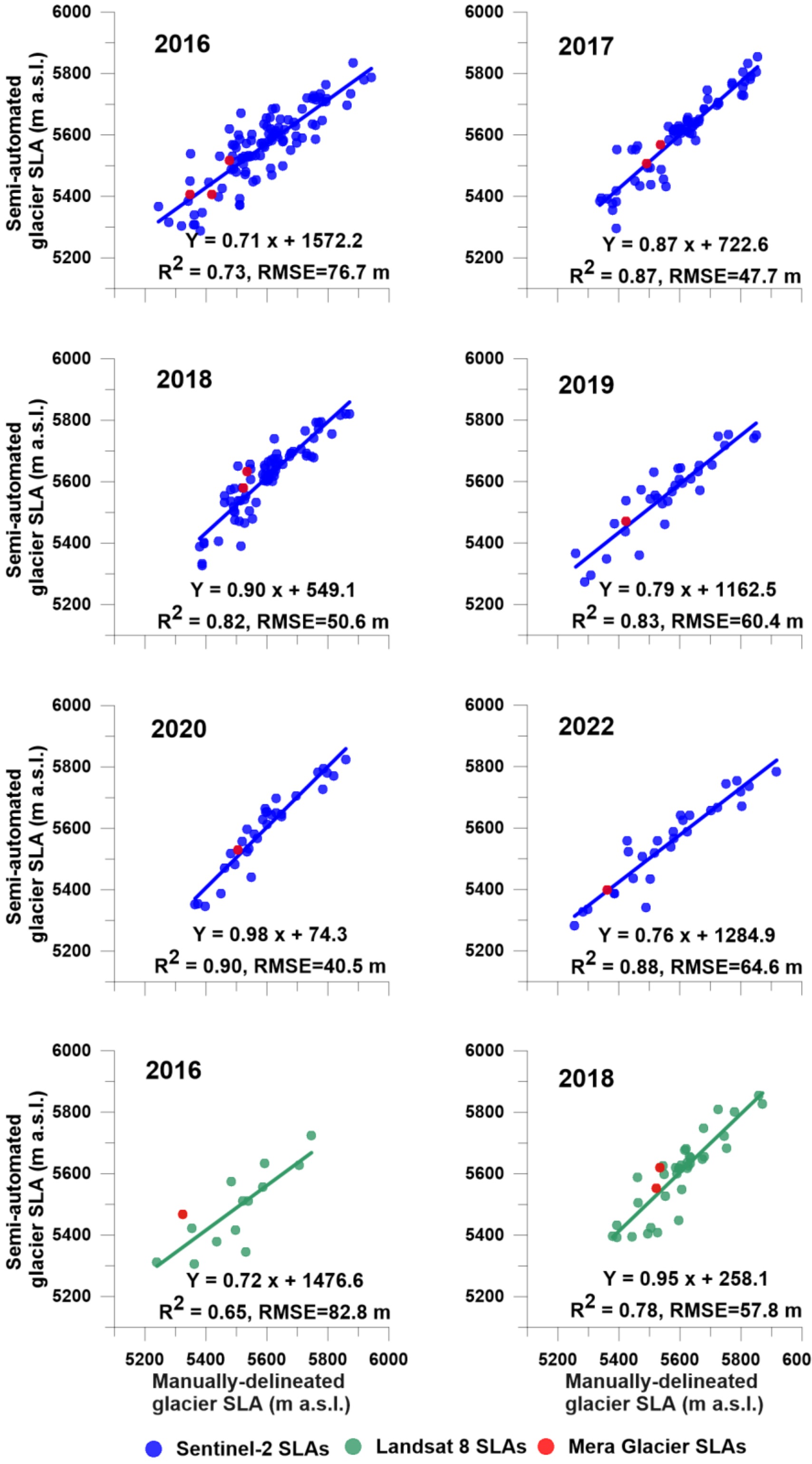

Figure 5.5 Yearly comparison of Landsat and Sentinel-2 glacier SLAs with high-resolution glacier SLAs on a glacier-by-glacier basis. SLAs for Mera are marked in red.

The residuals plotted against the averages of manually-delineated SLAs and semi-automated final SLAs (Figure 5.6A) follow a normal distribution, with a mean residual of 4.25 m (Figure 5.6A). The majority of the residuals (93%) fall within the limits of agreement (±1.96 standard deviation) (Bland and Altman, 1986), marked as shaded area in Figure 5.6, with only 27 residuals fall outside the limits of agreement. Some of the outliers in Figure 5.6A are most likely due to the presence of snow patches in the ablation areas as shown in Figure 5.7A. In other situations, parts of the glacier surface near the shadow have a lower reflectance and get misclassified as ice, resulting in false SLAs near the shadow edge, higher than the actual SLA location (i.e., negative residuals). Low reflectance crevassed areas shown in (Figure 5.7C) and spectrally-mixed pixels (snow/ice/shadow) (Figure 5.7D) impact the reflectance histogram utilized for Otsu thresholding, resulting in multiple peaks of different reflectance, and a threshold that is either lower or higher than the optimal threshold needed to effectively separate snow and ice. These resulted in positive and negative residuals, respectively (Figure 5.6A). Supraglacial lakes were misclassified as snow due to the high reflectance or frozen lakes in winter (Figure 5.7B) resulting in snowlines being located at lower altitudes than the actual snowline, which appeared as positive residuals in Figure 5.6A.

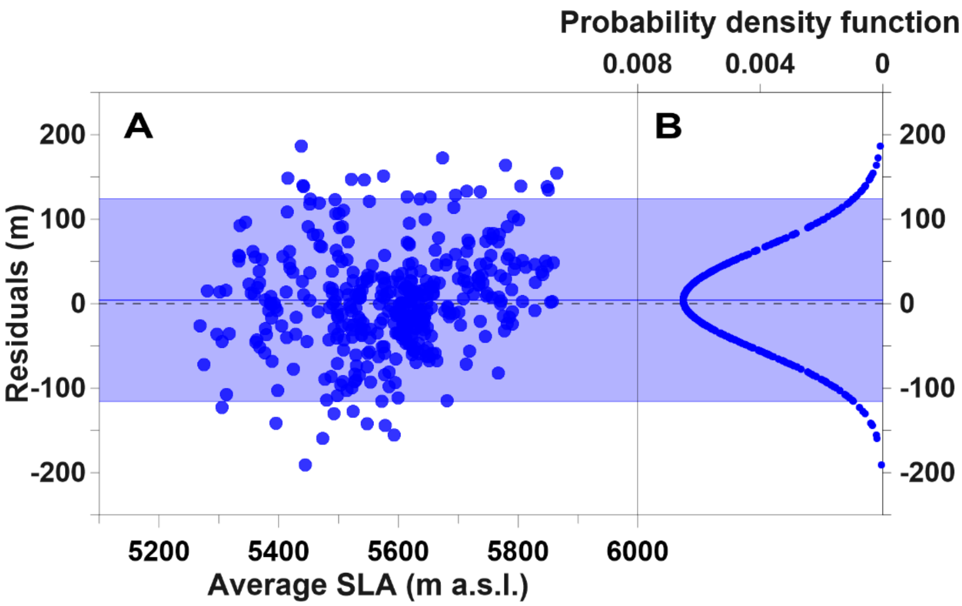

Figure 5.6 A) Bland-Altman plot of the average SLAs and the residuals (manually-delineated SLA minus semi-automated SLA); (B) normal distribution curve of residuals. The upper and lower limits of agreement correspond to ±1.96 times of standard deviation from the mean residual.

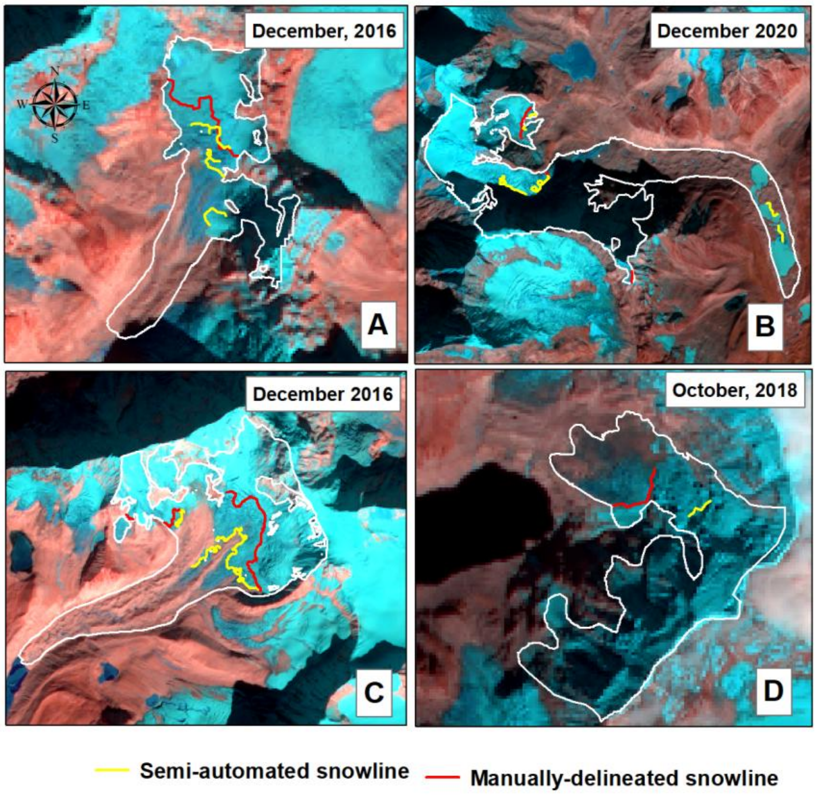

Figure 5.7Examples of challenging situations where the semi-automated method failed to accurately detect the SLA: glaciers with snow patches in the ablation area (A), shadows and supraglacial lakes (B), crevasses (C) and mixed pixels (snow/ice/shadow) (D). The background images are S2 false color composites (bands 11,8,4).

## 5.6 Discussion

### 5.6.1 Advances and limitations of the SLA method

The proposed SLA extraction method provides promising results, yielding overall very small differences in means of SLAs when compared to high-resolution satellite data (Table 5.1). However, these differences do vary on a year-by-year basis (S2: 1.06 to 23.95 m; L8: 4.36 to 9.74 m) depending on cloud cover and the quality of images (shadows, etc.). Overall, the performance of the method applied to basin scale showed good agreement with the manually-delineated SLAs at the glacier scale (Figure 5.4), with challenges remaining in different topographic settings (Figure 5.7). The automated filtering procedure based on the negative buffer, box plot and sieve filter proposed in this study effectively minimized the outliers around the ridgelines as well as in the accumulation and ablation areas.

While the present method shows potential for efficiently detecting SLAs, it is nevertheless subjected to the limitations of optical data, i.e., persistent cloud cover in the central-eastern region of the Himalaya during the monsoon. Therefore, in such areas, the use of other types of data such as Synthetic Aperture Radar, which are not affected by clouds, should be tested (Garg et al., 2022). In the monsoon-dominated areas, any (semi-) automated method is further challenged by the snowfall and wind re-deposition which may cover the glacier for part of the ablation season (Brun et al., 2015), as discussed above. Furthermore, the oversaturation issue due to highly reflective surfaces (i.e., bright snow) and stripping due to scanline corrector (SLC) failure in Landsat 7 (ETM+) (USGS, 2024) are general sources of uncertainties in optical data, but it did not affect this study which used Landsat 8. In this study, the image selection was quality controlled as much as possible to minimize the effect of these issues.

## 5.7 Conclusions

This improved semi-automated method, with Otsu thresholding and an automated filtering procedure, represents a robust approach for identifying glacier SLAs from satellite data such as Landsat and Sentinel. It has the advantage of using only limited input data (freely available DEM and multi-sensor satellite images), making it suitable for application to multi-spatial scales, from glacier to basin scale. The automated filtering procedure implemented in this study is an advancement in the previous semi-automated SLA delineation routine as it enhances the reliability of SLA estimates by minimizing errors due to shadows, crevassed areas, snow patches, etc. It provided high accuracy when compared to high-resolution data despite a few remaining outliers. Though in this study, the method was implemented on post-monsoon cloud-free images, the workflow is flexible and can also be used for other seasons, if images are cloud-free. This holds potential for investigating snowline evolution throughout the year from glacier to basin scale. Prospective improvements to separate snow and ice include the addition of more sophisticated methods based on spectral unmixing (Painter et al., 2009; Racoviteanu et al., 2021), machine learning-based classification for glacier surfaces and/or integration of the method in the Google Earth Engine platform (Loibl et al., 2025).

The method developed in this chapter lays the foundation for consistent and large-scale analysis of snowline altitudes across glacierized basins. By enabling the generation of reliable SLA datasets over time, it enables studying glacier-climate interactions, mass balance variability, and climate change impacts with improved spatial and temporal resolution. In the following chapter, this method is leveraged to reconstruct SLA time series across the Dudh Koshi basin and to investigate the relationship between SLA and ELA on Mera Glacier, thereby assessing the reliability of using remotely sensed snowlines ($SLA_{max}$) as a proxy for equilibrium line altitude (ELA) in monsoon-dominated regions.

# Chapter 6

# SLA-ELA relationship in the monsoon-dominated region

## 6.1 Introduction

Glacier equilibrium line altitude (ELA) is a robust climatic indicator and a key proxy for assessing glacier mass balance and long-term glacier health (Braithwaite and Raper, 2009; Cuffey and Paterson, 2010). Defined as the altitude at which annual accumulation equals ablation, the ELA reflects the net outcome of seasonal climate variability. In many glaciated regions, especially at mid-latitudes, the late-ablation maximum snowline altitude ($SLA_{max}$) has been widely used as a remote-sensing proxy for ELA (Rabatel et al., 2013; Tawde et al., 2016; Barandun et al., 2018; Chandrasekharan et al., 2018). The temporal evolution of SLA across glaciers is often closely tied to climate variables, especially temperature and precipitation. However, in monsoon-dominated regions such as the central Himalaya, this relationship becomes more complex (Rabatel et al., 2012; Yuwei et al., 2014). Here, the glacier mass balance regime is governed by simultaneous summer accumulation and ablation, driven by strong seasonality in both precipitation and cloud cover (Wagnon et al., 2013; Sherpa et al., 2017). This duality introduces temporal and spatial variability in snowline positions, complicating the assumption that $SLA_{max}$ approximates ELA. Factors such as episodic summer snowfall, post-monsoon accumulation, topographic shading, and microclimatic heterogeneity often result in decoupling between $SLA_{max}$ and true ELA (Fujita, 2008; Rabatel et al., 2012; Yuwei et al., 2014; Brun et al., 2015). Furthermore, persistent cloud cover during the ablation season frequently obscures the snowline, introducing observational gaps that challenge consistent monitoring (Racoviteanu et al., 2019; Barandun et al., 2021).

Despite these complexities, a few studies in High Mountain Asia have attempted to empirically test the SLA-ELA relationship in summer-accumulation type glaciers. For instance, Yuwei et al. (2014) and Rabatel et al. (2012) have shown that while $SLA_{max}$ remains a useful proxy for ELA, it often exhibits an offset that varies across years and glacier types. These deviations highlight the need for high-quality, temporally consistent SLA datasets—especially in regions with challenging observational conditions like the Himalaya.

This chapter investigates the SLA-ELA relationship on Mera Glacier, located in the monsoon-dominated central Himalaya, by leveraging a reconstructed multi-year SLA dataset. This dataset, generated using the method developed and validated in Chapter 5, allows us to explore the inter-annual and sub-monthly variability of SLA and assess the agreement of $SLA_{max}$ with field-based ELA estimates from the GLACIOCLIM observatory. Our analysis focuses on identifying temporal patterns in SLA, quantifying its elevation offset from ELA across multiple years, and evaluating the implications for using $SLA_{max}$ as a proxy under monsoon-dominated region.

## 6.2 Study area

The assumption that $SLA_{max} \approx ELA$ was tested for Mera Glacier (~4.8 $km^2$ in 2018, 4940 to 6420 m a.s.l.), located in the central part of the Dudh Koshi basin within the Hinku Valley (Figure 6.1). Mera Glacier is a small clean glacier monitored in the field since 2007 within the framework of the GLACIOCLIM network (Wagnon et al., 2013, 2021). It is north-oriented and it divides into two branches ~5800 m, referred to as Mera and Naulek (Wagnon et al., 2013). In this study, only the Mera branch was investigated, which has a denser network of ablation stakes, offering a-priori field knowledge and opportunities for comparing the remote sensing SLAs with field-based ELAs. The mass balance of Mera Glacier is highly sensitive to climatic variations, with a ±1°C change in temperature resulting in a −0.75 ± 0.17 m w.e. change in glacier-wide mass balance and a ±20% change in precipitation leading to a +0.52 ± 0.10 m w.e. change (Khadka et al., 2024).

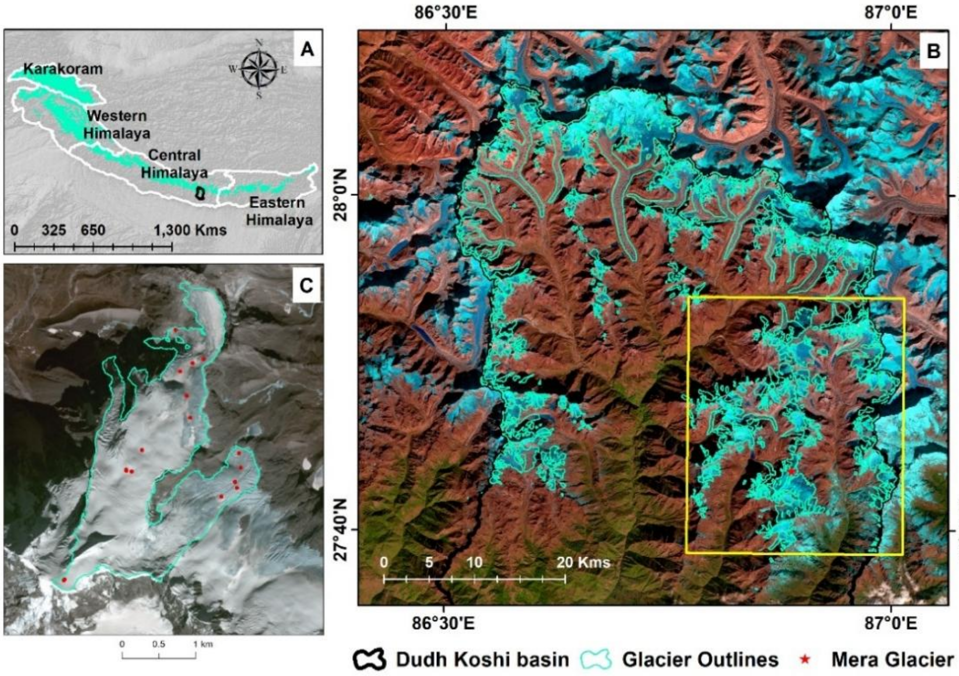

Figure 6.1 Study area showing the upper Dudh Koshi basin in the central Himalaya, with glaciers from the GAMDAM inventory shown in cyan (A, B). The yellow box shows the subset used for validation around the Hinku sub-basin (n = 177 glaciers) (B). Mera Glacier in this sub-basin is also marked (red star) (B) and shown in panel C along with the stake locations (red dots). The background images are a false color composite of the Planet RapidEye image (bands 5,4,3) from 10 Jan 2016 (C) and Sentinel-2 image (bands 11,8,4) from 14 Jan 2016 (B).

## 6.3 Datasets

### 6.3.1 Remote sensing data

This chapter utilizes an extended set of multi-temporal satellite imagery acquired from the Sentinel-2 (S2) and Landsat 8 (L8), consistent with the datasets described in Chapter 5. While the previous chapter focused on a limited number of post-monsoon scenes (October–December) from 2016 to 2022 for method development and validation, the current analysis incorporates a significantly broader temporal range. Specifically, all available cloud-free images between April and January during the period 2015–2023 were included to enable the reconstruction of a detailed SLA time series. All imagery underwent consistent pre-processing, including atmospheric and topographic correction, as detailed in Chapter 5. A complete list of all Sentinel-2, Landsat

8, PlanetScope, and Venµs images used in this analysis is provided in Table 6.1 including the images previously used for method validation in Chapter 5.

Table 6.1 Remote sensing datasets used in this study for the Dudh Koshi study area over the period 2015–2023

| | | | | | | |
|---|---|---|---|---|---|---|
| **Sentinel-2 MSI, Level L1C** | | | | | | |
| 2016-01-14* | 2016-04-13 | 2016-10-30 | 2016-11-29 | 2016-12-09* | 2016-12-29* | 2017-01-08 |
| 2017-01-18 | 2017-04-18 | 2017-10-15 | 2017-10-30 | 2017-11-19 | 2017-11-24 | 2017-12-09* |
| 2017-12-14 | 2017-12-29* | 2018-01-03 | 2018-01-08 | 2018-01-18 | 2018-01-23 | 2018-01-28 |
| 2018-04-23 | 2018-05-08 | 2018-10-15 | 2018-10-20* | 2018-10-30 | 2018-11-04 | 2018-11-09 |
| 2018-11-14 | 2018-11-24* | 2018-12-04 | 2018-12-09 | 2018-12-14 | 2018-12-19 | 2018-12-24 |
| 2018-12-29 | 2019-01-13 | 2019-01-18 | 2019-01-28 | 2019-05-08 | 2019-10-15 | 2019-11-19 |
| 2019-11-24 | 2019-12-04* | 2019-12-09 | 2019-12-19 | 2019-12-24 | 2019-12-29 | 2020-01-13 |
| 2020-01-23 | 2020-01-28 | 2020-04-02 | 2020-04-12 | 2020-04-17 | 2020-10-09 | 2020-10-24 |
| 2020-11-08 | 2020-11-13 | 2020-11-18 | 2020-11-23 | 2020-11-28 | 2020-12-03* | 2020-12-08 |
| 2020-12-13 | 2020-12-18 | 2020-12-28 | 2022-04-12 | 2022-10-24 | 2022-11-03 | 2022-11-13 |
| 2022-11-23 | 2022-11-28 | 2022-12-03 | 2022-12-08* | 2022-12-18 | 2022-12-23 | 2022-12-28 |
| 2023-01-07 | 2023-01-12 | 2023-01-17 | 2023-01-22 | 2023-01-27 | | |
| **Landsat-8 OLI, Collection 2 Level 1 (L1TP)** | | | | | | |
| 2015-05-25 | 2015-07-12 | 2015-09-30 | 2015-11-01 | 2015-11-17 | 2015-12-19 | 2016-11-03 |
| 2016-11-19* | 2017-11-06 | 2017-11-22 | 2018-10-24* | 2018-11-25* | 2019-10-27 | 2019-11-12 |
| 2020-10-29 | 2020-11-14 | 2020-11-30 | 2022-11-04 | 2022-11-20 | | |
| **Planet RapidEye, Level 3A** | | | | | | |
| 2016-01-10 | | | | | | |
| **Planet PSS, Level 3B** | | | | | | |
| 2016-11-17 | 2016-12-08 | 2016-12-30 | 2017-12-29 | 2020-12-02 | 2022-12-08 | |
| **VENµS VSSC, VM1 mission** | | | | | | |
| 2017-12-09 | 2018-10-21 | 2018-11-22 | 2019-12-04 | | | |

* denotes the images used for method validation in chapter 5

## 6.3.2 Field data

Field-based ELAs, point mass balance and corresponding snow depths for Mera Glacier were available from the GLACIOCLIM network over 2007−2022. Ablation stakes installed on the Mera branch are measured each year at the end of the ablation season (generally November) using the glaciological method (Wagnon et al., 2013). Field-based ELAs are estimated from the vertical mass balance gradient using stake measurements and elevations from the 2012 Pleiades DEM as reported in the studies.

## 6.4 Methodology

The same improved snowline extraction method described in chapter 5 was used to generate the SLA time series for Dudh Koshi basin. Basin-wide average SLA were calculated as an average of all glacier SLAs within the Dudh Koshi basin. To evaluate the reliability of $\mathrm{SLA}_{\mathrm{max}}$ as a proxy for ELA on Mera Glacier, SLAs on same dates as well as $\mathrm{SLA}_{\mathrm{max}}$ extracted from S2 and L8 images were compared with field-based ELAs obtained through direct mass balance measurements. This comparison was performed for the hydrological years over 2015–2023. For Mera Glacier, SLAs were masked from the basin scale final SLAs for all the available cloud-free satellite images over the period 2015–2023. Field measurements are generally performed during November at the end of the hydrological year, and our satellite data overlapped these dates ± 1 day.

## 6.5 Results

### 6.5.1 Basin- and Glacier-scale snowline fluctuations

Here the fluctuation of the basin-wide average SLAs over the Dudh Koshi basin and SLAs for Mera Glacier within this basin over the period 2015–2023 are presented (Figure 6.2). The annual basin-wide average $\mathrm{SLA}_{\mathrm{max}}$ and glacier $\mathrm{SLA}_{\mathrm{max}}$ for Mera Glacier are given in Table 6.2 and also shown with sub monthly basin-wide average SLAs in Figure 6.2 and Appendix A Table S1. Over the Dudh Koshi basin (462 glaciers), a total of 6330 glacier SLAs were detected over the period 2015–2023 ranging from 5090 m to 5624 m. Of these, a total of 68 glacier SLAs were detected on Mera Glacier, ranging from 5168 m to 5673 m over the period 2015–2023. The number of glacier SLAs detected varied annually depending on the sensor’s temporal resolution as well as cloud cover and surface conditions (Figure 6.2, Appendix A Table S1).

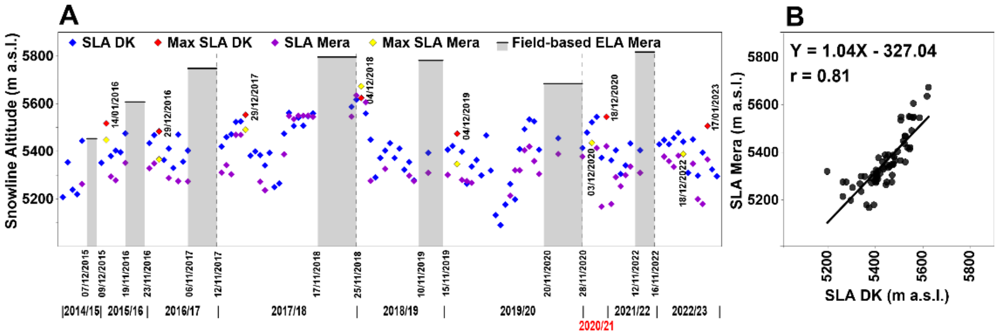

Figure 6.2 (A) Remote sensing basin-wide average SLAs for Dudh Koshi basin (blue) and glacier SLAs for Mera Glacier (purple) over the period 2015–23. $SLA_{max}$ are marked in red for Dudh Koshi basin and yellow for Mera glacier. The span of field measurements dates is shown as grey vertical bars with field-based ELAs as horizontal black line at top. X-axis displays the dates of field measurements and hydrological years. (B) The scatter plot of basin-wide average SLAs vs. glacier SLAs on common dates over the study period.

Table 6.2 Basin-wide average $SLA_{max}$ and glacier $SLA_{max}$ (Mera Glacier) for each hydrological year over the period 2015–2023.

| Year | Basin-wide average $SLA_{max}$ | Glacier $SLA_{max}$ | Difference (m) |
|---|---|---|---|
| 2014/15 | 5517 | 5458 | 69 |
| 2015/16 | 5481 | 5366 | 115 |
| 2016/17 | 5553 | 5491 | 62 |
| 2017/18 | 5624 | 5673 | -49 |
| 2018/19 | 5476 | 5347 | 129 |
| 2019/20 | 5546 | 5436 | 110 |
| 2021/22 | 5506 | 5389 | 117 |
| Average | 5525 | 5528 | 79 |

Basin-wide average $SLA_{max}$ ranged from 5476 m in 2019 to 5624 m in 2018 and averaged 5525 m over the period 2015–2023 (Table 6.2, Figure 6.2). $SLA_{max}$ of Mera Glacier ranged from 5347 m in 2019 to 5673 m in 2018 and averaged 5528 over the entire period (Table 6.2, Figure 6.2). The years with the lowest and highest $SLA_{max}$ (2019 and 2018, respectively) were consistent between the basin-wide average $SLA_{max}$ and glacier $SLA_{max}$, although glacier $SLA_{max}$ were on average ~79 m lower than basin-wide average $SLA_{max}$ (Table 6.2). The comparison between Mera Glacier SLAs and basin-wide average

SLAs shows a good agreement (Person’s r = 0.81), indicating that Mera Glacier SLA is representative of basin-wide average SLA (Figure 6.2). Estimated basin-wide average SLAs are within the range of SLAs reported in a previous study for the same basin by Racoviteanu et al. (2013) (5172−6047 m, mean ELA = 5568 m) based on analysis of December 2005 imagery. Our results are also in agreement with contemporary ELAs reported in Owen and Benn (2005) for the same region (5200−5800 m, with a mean value of 5600 m).

### 6.5.2 Spatial variability of snowline altitude

The spatial distribution of mean SLAs across the Dudh Koshi basin over 2015−2023 shows pronounced intra-basin variability (Figure 6.3). The mean SLA ranges from 4842 to 5858 m a.s.l. over 2015−2023. Mean SLAs are generally lower in the southern part and increases towards the north direction in the basin. This highlights the strong control of topography and local precipitation regimes on SLA behaviour. The observed spatial pattern corresponds well with the established precipitation gradient in the region, whereby windward slopes receive greater monsoonal accumulation while inner valleys remain comparatively dry (Sherpa et al., 2017). Grouping glaciers by mean elevation further highlights differences in SLA behaviour. Mean SLAs rise steadily from ~4950 m in the 4900–5100 m elevation band to ~5640 m in the 5900–6100 m elevation band. However, the relative position of SLA to glacier mean elevation reveals contrasting glacier sensitivities. In the lowest elevation bands, SLAs are very close to the glacier mean elevation (offsets of only −6 to −36 m), indicates small accumulation area and makes these glaciers highly vulnerable. Mid-elevation glaciers (5300–5700 m) show slightly larger offsets (−30 to −97 m), suggesting more balanced conditions. By contrast, high-elevation glaciers (>5700 m) have SLAs far below their mean elevations (−200 to −600 m), indicating substantial accumulation buffers and greater resilience under present climate.

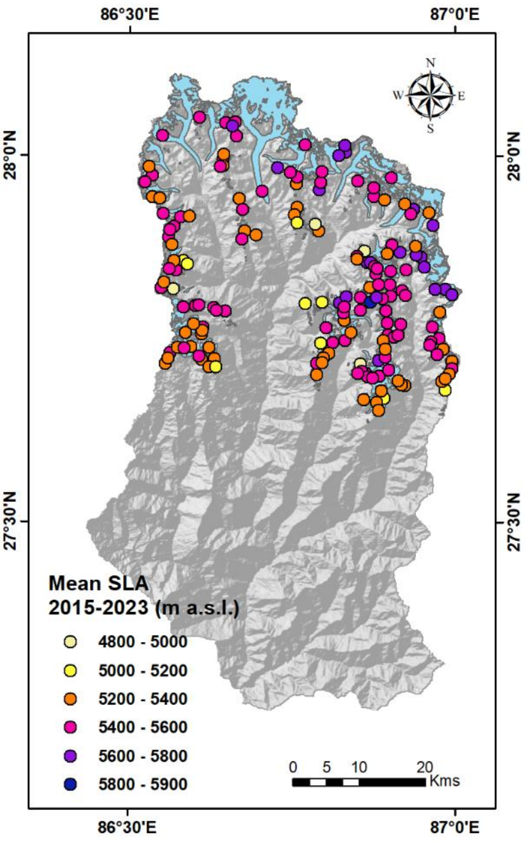

Figure 6.3 Spatial distribution of mean SLA over 2015–2023 in Dudh Koshi basin

## 6.6 Discussion

### 6.6.1 Intra- and inter-annual SLA trends

The intra- and inter-annual variability of SLA give insights into the temporal behavior of SLAs in a monsoon-dominated region. Intra-annual SLA evolution within each hydrological year showed generally increasing patterns from April to November, but our results show that none of the trends were statistically significant for either basin-wide average SLA or glacier SLA (Mera Glacier), assessed using the Mann-Kendall test with 95% confidence level ($p > 0.05$). Remote sensing SLA on Mera Glacier often continue to rise after the field measurement dates i.e., November. Basin-wide average SLA$_{max}$ and glacier SLA$_{max}$ do not occur on same dates every year but they usually occur in the post-monsoon to early winter months (December or even in January) which belongs to the next hydrological year (Figure 6.2A). This is consistent with the previous studies, which suggest that the SLA observed in post-monsoon or winter months reflects the previous ablation season due to the wind erosion, snow redistribution and sublimation (Wagnon et al., 2013; Brun et al., 2015). No significant trends were found in inter-annual basin-wide average $SLA_{max}$ and glacier $SLA_{max}$ over the study period, based on Mann-Kendall test with 95% confidence level ($p > 0.05$). While our results show considerable intra-annual variability in SLA and inter-annual variability in $SLA_{max}$, neither show a statistically significant trend over a relatively short period.

### 6.6.2 Discrepancies between the remote sensing SLAs and the field-based ELAs

When comparing field-based ELA and remote sensing SLA on Mera Glacier on the common dates at the end-of-the-ablation season (i.e. November), large differences were found, ranging from 161 m for the 2017/18 hydrological year to 508 m for 2021/22 (Figure 6.2). The average remote sensing SLA over the period 2015–23 (5377 m) was ~400 m lower than average field-based ELA (5739 m) estimated using the traditional glaciological method (Wagnon et al., 2021). These large differences persisted to some extent when comparing $SLA_{max}$ (generally occurring at a later date) with and field-based ELAs for all the hydrological years except 2014/15 (5 m difference) (Table 6.3 and Figure 6.2). However, these were smaller (up to 435 m in 2018/19) than those based on concomitant SLAs and field-based ELAs as mentioned above. These mismatches suggest that the remote sensing SLAs (and even $SLA_{max}$) do not fully capture the true ELA on Mera Glacier. To check for potential biases in the remote sensing SLAs, the impact of spatial resolution and choice of DEM was evaluated. The comparison of $SLA_{max}$ estimated from S2/L8 images and high-resolution imagery on the same or nearby date (1 or 2 days) showed no significant differences (Table 6.3). Similarly, a sensitivity analysis of remote sensing SLAs to the choice of DEM (AW3D30 DEM, 30 m spatial resolution vs. HMA DEM, 8 m) yielded only ~35 m difference (Table 6.3). This is roughly 10 times smaller than the mean difference of ~400 m between remotely sensed SLA and field-based ELA (2015–23). This shows that the choice of DEM did not significantly influence the large negative bias in the remote sensing SLA values, indicating that other surface processes at play on monsoon-dominated glaciers contribute to the low remote sensing SLAs/$\text{SLA}_{\text{max}}$.

It is hypothesized that the systematic mismatch between the concomitant SLAs and field-based ELAs on Mera Glacier, (i.e., observed on the same dates), is due to either snow persisting from the monsoon, or snowfall events occurring at the end-of-the-ablation season. Mera Glacier, being a summer-accumulation-type glacier, receives snowfall throughout the summer. While most of this snow is expected to melt during the monsoon due to higher temperatures thus exposing the glacier ice over the ablation area, some snow can persist throughout the post-monsoon. Similarly, any snowfall occurring in October and November (when temperatures are generally much lower), is more likely to persist on the glacier surface. Furthermore, throughout the period October to April, snow is systematically redistributed from the higher altitudes by the strong winds (Wagnon et al., 2013). The combination of snow persistence and snow redistribution most likely contributes to the systematically lower SLAs compared to field-based ELAs observed at the end of the ablation season. As a result, in most years, the maximum SLA (~ ELA) may not occur until later in the winter or the following year before the melting season starts (Brun et al., 2015).

To support this hypothesis, field measurements (snow depths and point mass balance) on Mera Glacier were examined. Field measurement data show snow persistence during the November field campaigns, even below the ELA (Table 6.4). In most years, glacier areas between 5400 and 5600 m showed negative mass balances; yet, by the end-of-the-ablation season, these areas remained snow-covered, with average snow depths ranging from ~15 cm (2019/20) to ~72 cm (2020/21), and an overall mean of ~37 cm except in 2017/18, when snowfall was minimal (a dry year). Consistent with our hypothesis that late-season/persistent snowfall drives the SLA-ELA difference, the 2017/18 hydrological year showed the smallest discrepancy between the remotely sensed SLA and the field-based ELA (161 m) (Figure 6.2), likely due to minimal snowfall over the glacier surface during October–November, just prior to field measurements. Comparison between SLA and field-based ELA in 2020/21 could not be performed because the glacier was completely snow-covered following the typhoon event.

Table 6.3 Comparison of remote sensing (S2/L8 and Planet/Venµs) SLA$_{max}$ with field-based ELAs for Mera Glacier over the period 2015–2023, extracted from AW3D30 (30 m) and HMA (8 m) DEMs

| **Year** | **Field observation data** | | **S2/L8 SLA$_{max}$ (m)** | | | **Planet/Venµs SLA$_{max}$ (m)** | | |
|---|---|---|---|---|---|---|---|---|
| | **Measurement date** | **Field-based ELA** | **Image date** | **AW3D30 DEM** | **HMA DEM** | **Image date** | **AW3D30 DEM** | **HMA DEM** |
| 2014/15 | 07–09 Dec 2015 | 5453 | 14 Jan 2016 | 5448 | 5421 | 10 Jan 2016 | 5438 | 5431 |
| 2015/16 | 19–23 Nov 2016 | 5607 | 29 Dec 2016 | 5366 | 5327 | 30 Dec 2016 | 5313 | 5256 |
| 2016/17 | 06–12 Nov 2017 | 5748 | 29 Dec 2017 | 5491 | 5448 | 29 Dec 2017 | 5564 | 5544 |
| 2017/18 | 17–25 Nov 2018 | 5796 | 04 Dec. 2018 | 5673 | 5670 | NA | NA | NA |
| 2018/19 | 10–15 Nov 2019 | 5782 | 04 Dec. 2019 | 5347 | 5305 | 04 Dec 2019 | 5394 | 5341 |
| 2019/20 | 20–28 Nov 2020 | 5684 | 03 Dec. 2020 | 5436 | 5417 | 02 Dec 2020 | 5449 | 5404 |
| 2021/22 | 12–16 Nov 2022 | 5817 | 18 Dec. 2022 | 5389 | 5338 | NA | NA | NA |

Table 6.4 Average snow depth H (cm) and mean altitudinal mass balance b$_a$ (m w.e.) on Mera Glacier for the hydrological years over the period 2015–23. Ablation stake measurements were averaged per 100 m elevation bin at altitudes above 5400 m.

| **Year** | **2014/15** | | **2015/16** | | **2016/17** | | **2017/18** | | **2018/19** | | **2019/20** | | **2020/21** | | **2021/22** | |
|---|---|---|---|---|---|---|---|---|---|---|---|---|---|---|---|---|
| **Elev.(m)** | **H** | **b$_a$** | **H** | **b$_a$** | **H** | **b$_a$** | **H** | **b$_a$** | **H** | **b$_a$** | **H** | **b$_a$** | **H** | **b$_a$** | **H** | **b$_a$** |
| 5400–5500 | 18.3 | -0.2 | 64.5 | -0.9 | 24.8 | -1 | 0 | -1.3 | 48.5 | -1.2 | 17.0 | -1.3 | 72 | 0.3 | 62.5 | -1.4 |
| 5500–5600 | 16.5 | | 64.0 | | 16.5 | -1.1 | 5.4 | -1 | 57.7 | -1.1 | 12.5 | -0.4 | | | 70.5 | |

This analysis of Mera Glacier suggests that comparing satellite-derived SLAs with field-based ELAs is particularly challenging in monsoon-dominated regions. In such regions, late-summer snowfall often persists on the glacier surface due to lower temperatures, leading to systematically lower SLAs compared to field ELAs. This is evident from the significant discrepancies observed on Mera Glacier and on other glaciers in the Tian Shan and tropical regions (Rabatel et al., 2012; Yuwei et al., 2014). In these regions, due to simultaneous ablation and accumulation processes, remote sensing SLAs do not accurately capture the true ELA, suggesting that the assumption that $SLA_{max} \approx ELA$ does not hold in such regions.

## 6.7 Conclusions

This chapter examined the spatio-temporal variability of SLAs at both basin and glacier scale using a consistent semi-automated method, with a particular focus on evaluating $SLA_{max}$ as a proxy for ELA on Mera Glacier. The method, previously validated over a subset of images in chapter 5, was applied across a broader set of cloud-free satellite scenes spanning April to January over 2015–2023, enabling the construction of a robust SLA time series. The proposed SLA extraction method successfully captured the intra- and interannual evolution of snowlines, revealing important seasonal patterns and post-monsoon snowline exposures. On Mera Glacier, the method allowed detailed tracking of SLA fluctuations throughout the hydrological year, including the detection of $SLA_{max}$ typically exposed during the dry, post-monsoon months.

However, when $SLA_{max}$ values were compared with field-based ELA measurements, systematic discrepancies were observed, with $SLA_{max}$ consistently lower than ELA. This indicates that the common assumption $SLA_{max} \approx ELA$ does not hold true for summer accumulation-type glaciers such as Mera Glacier. The mismatch is explained by frequent fresh snowfalls, wind-driven snow redistribution and sublimation which obscure the actual equilibrium line and contribute to overestimating the accumulation area when using optical imagery. These findings highlight the limitations of relying solely on remote sensing-derived $SLA_{max}$ as a proxy for ELA in monsoon-dominated regions. At the same time, the study underscores the value of using a consistent, scalable, and semi-automated SLA extraction method to capture snowline dynamics. In conclusion, while $SLA_{max}$ offers useful insights into glacier surface conditions, its use as an ELA proxy in regions with complex climatic regimes must be approached with caution. Efficient, validated SLA estimation methods remain essential for monitoring glacier behavior and climate sensitivity in High Mountain Asia.

# Chapter 7

# Conclusions and future work

## 7.1 Conclusions

This thesis presents an integrated assessment of snow and glacier melt hydrology in the Himalaya, addressing some of the most pressing challenges associated with modelling meltwater contributions, evaluating the reliability of remote sensing-derived indicators, and understanding regional hydrological responses to climate change. The work combines temperature-index models and spatially distributed glaciohydrological modelling with remote sensing and field data across three climatically diverse Himalayan basins: Chandra-Bhaga Basin in the western Himalaya, Gangotri Glacier System and Dudh Koshi basins in the central Himalaya. The chapters are organized to progressively tackle model calibration and parameter transferability, long-term melt reconstruction, remote sensing method development, and validation of glacier equilibrium line estimation.

The modelling tests conducted in the Chandra-Bhaga Basin highlight critical limitations in applying parameters calibrated at smaller catchments to larger or more complex basins. Specifically, parameters tuned using detailed observations from the well-monitored Chhota Shigri Glacier Catchment were found to produce reliable discharge simulations within the catchment but failed to replicate discharge dynamics accurately when applied to the broader Chandra-Bhaga Basin. Discharge was substantially overestimated, indicating that parameter sensitivity, catchment area characteristics, glacier cover distribution, and local climate play important roles in model parameter transferability. This finding reinforces the need for caution when applying temperature-index models such as SRM across different spatial scales.

Although SRM remains a practical and low-data-requirement tool for glaciohydrological modelling, its effective application requires basin-specific calibration, especially in the heterogeneous and data-scarce Himalayan terrain.

The subsequent chapter shifts focus to the long-term hydrological behaviour of the Gangotri Glacier System (GGS), one of the largest and most studied glacier systems in the central Himalaya. Using the Spatial Processes in Hydrology (SPHY) model, forced by bias-corrected IMDAA reanalysis data, the study reconstructs snow and glacier melt contributions from 1980 to 2020. A two-tier calibration approach utilizing both in-situ discharge (2000–2003) and geodetic glacier mass balance (2000–2019) was implemented to reduce parameter equifinality and enhance model robustness. Results reveal that snowmelt was the predominant contributor to total streamflow (64%), followed by glacier melt (21%), rainfall runoff (11%), and baseflow (4%). A decadal shift in the timing of peak discharge from August to July was also observed, which is attributed to increased temperature and declining winter snowfall. Interestingly, although temperature has increased during the study period, glacier melt contributions remained stable, while snowmelt showed a declining trend due to shrinking snow cover. These results suggest a complex interplay between warming-induced melt acceleration and the reduction in available snowpack, illustrating different response of cryospheric components to climatic change.

Building upon these modelling efforts, the next chapter of the thesis introduces a refined, semi-automated methodology for extracting snowline altitudes (SLAs) from optical satellite imagery. Recognizing the limitations of SLA extraction in high-relief, cloud-prone regions, a new workflow was developed in Python, incorporating atmospheric and topographic corrections, dynamic thresholding using the Otsu method, and post-processing filters to eliminate erroneous pixels caused by shadows, crevasses, snow patches, and steep slopes. The methodology was implemented over the Dudh Koshi basin using Sentinel-2 and Landsat imagery and validated using high-resolution Planet and Venµs satellite data. In this chapter, the method was applied specifically to post-monsoon satellite images when clearer atmospheric conditions prevail to assess its accuracy and reliability. By applying the approach across hundreds of glaciers, including a dense validation subset in the Hinku Valley, the workflow demonstrated its ability to extract consistent SLAs across sub-monthly timescales despite difficult conditions. This chapter not only offers a replicable framework for large-scale SLA monitoring in the monsoon-dominated Himalaya but also sets the stage for improved integration of satellite-derived SLAs in glaciohydrological models and mass balance studies.

The final chapter focuses on evaluating the long-held assumption that the end-of-ablation season SLA ($SLA_{max}$) is a suitable proxy for equilibrium line altitude (ELA), particularly in monsoon-dominated glacier systems. Expanding the temporal scale of the dataset, SLAs were extracted across the full period from April to January to develop a robust seasonal SLA time series for Dudh Koshi basin as well as Mera Glacier. This extended dataset was then used to identify $SLA_{max}$ for each year and compare it systematically with field-based ELA measurements from the GLACIOCLIM monitoring network. The results clearly show that $SLA_{max}$ consistently underestimates ELA in this region, challenging the validity of this proxy relationship in summer accumulation-type glaciers. This underestimation is attributed to dynamic surface processes including frequent monsoonal snowfall, snow redistribution by wind, sublimation, and temporary snow cover over ablation zones. These conditions disrupt the typical melt–accumulation transition zone visibility and render remote sensing-based SLA proxies unreliable without region-specific corrections. The chapter demonstrates that assumptions validated in temperate or mid-latitude settings may not be held in the monsoon-dominated Himalaya, underscoring the importance of field-based validation.

Together, the findings of this thesis converge on several overarching themes. First, model calibration must be highly localized in glacierized regions due to the steep spatial gradients in topography, climate, and glacier cover. Second, multi-criteria calibration using independent datasets (e.g., discharge and geodetic mass balance) significantly improves model credibility in data-scarce regions. Third, while remote sensing offers unparalleled spatial and temporal coverage, the interpretation of glacier surface features such as SLAs requires a deep understanding of local meteorological and glaciological processes. Finally, the combined use of multi-criteria calibration in hydrological modelling, advanced remote sensing, and in-situ observations forms a powerful trio for understanding and anticipating hydrological change in Himalaya Karakoram. The insights from this thesis contribute to methodological improvements in modelling and monitoring snow and glacier melt contributions and offer a scientific foundation for developing climate-resilient water resource strategies in the Himalaya. They also provide transferable frameworks for other glacierized regions globally, where similar data limitations and climatic variability pose significant challenges to hydrological forecasting and glacier mass balance assessment.

## 7.2 Limitations of the study

Despite providing robust insights into snow and glacier melt processes across contrasting Himalayan basins, the thesis work is subject to some limitations related to data availability, methodological assumptions, and the intrinsic constraints of modelling and remote sensing approaches in complex mountain environments.

Following are some limitations of this thesis work:

- Precipitation forcing relied on reanalysis datasets and an elevation-based extrapolation approach, which are subject to known uncertainties in complex orographic terrain and propagate uncertainty into simulated snow and glacier melt contributions
- The SPHY model does not explicitly account for sublimation losses, which may be non-negligible in high-altitude glacier environments, and applies spatially uniform debris-related degree-day factors, limiting the representation of glacier- and elevation-specific melt enhancement associated with heterogeneous debris cover
- Optical satellite data used for SLA extraction are affected by persistent cloud cover, terrain shadows, and reflectance saturation, which constrain the temporal continuity of SLA estimates despite rigorous quality control

## 7.3 Future work

The complex and rapidly changing cryospheric and hydrological conditions in the Himalaya demand sustained scientific attention through new data sources, improved modelling approaches, and expanded spatial and temporal coverage.

Future research must adapt to the dynamic challenges posed by climate variability, technological innovations, and the growing importance of regional water security. Several key directions emerge from current gaps and challenges that can guide future research in this field.

Following are some possible future works:

- Future work should focus on developing transferable hydrological model parameterizations that reduce dependence on local calibration, thereby enabling broader application across diverse regions and scales
- Approaches such as statistical regression, physical scaling laws, or machine learning can be explored to relate model parameters directly to physiographic and climatic controls, improving scalability and applicability in ungauged basins
- Future studies can extend the multi-criteria calibration approach used here by incorporating additional datasets and evaluation metrics, improving parameter reliability and model robustness
- Integrating energy-balance components would address key limitation of the current model and enable more realistic simulation of glacier melt and other runoff components
- Applying this modelling framework to multiple Himalayan basins would enhance the consistency and reliability of long-term discharge reconstructions across diverse climatic settings
- On the remote sensing front, further automation and scaling of SLA extraction methods represent a promising direction. Building upon threshold-based and post-processing approaches, future research could incorporate machine learning classifiers, spectral unmixing, or time-series trend analyses to identify SLA under more challenging conditions such as high cloud frequency, variable surface albedo, or complex shadow
- Systematic, multi-site investigations across diverse Himalayan settings are needed to assess the validity of the $SLA_{max} \approx ELA$ assumption, and to guide necessary corrections in cases where the assumption does not hold
- Integration of diverse high-resolution satellite datasets to advance multi-dimensional glacier monitoring thereby improving both temporal and spatial resolution

In the broader climate and water management context, future efforts should focus on downscaling model outputs to support basin-scale water allocation, reservoir operations, and early warning systems, ensuring that meltwater projections translate into actionable adaptation strategies for downstream communities. At the same time, addressing persistent data gaps through expanded in-situ networks, low-cost sensors, and enhanced data-sharing will remain essential. By advancing process-based modelling, remote sensing automation, and regional parameter estimation, future research can bridge the gaps between data, methods, and applications, thereby strengthening the resilience of Himalayan water systems under a changing climate.

# REFERENCES

Aggarwal, S.P., Thakur, P.K., Nikam, B.R., Garg, V., 2014. Integrated approach for snowmelt run-off estimation using temperature index model, remote sensing and GIS. Current Science 106, 397–407.

Ahmed, R., Shamim, T., Bansal, J.K., Rather, A.F., Javaid, S., Wani, G.F., Malik, I.H., Ahmed, P., Jain, S.K., Imdad, K., Ford, J.D., Mir, R.A., 2024. Assessing climate trends in the Northwestern Himalayas: a comprehensive analysis of high-resolution gridded and observed datasets. Geomatics, Natural Hazards and Risk 15, 2401994. https://doi.org/10.1080/19475705.2024.2401994

Andermann, C., Longuevergne, L., Bonnet, S., Crave, A., Davy, P., Gloaguen, R., 2012. Impact of transient groundwater storage on the discharge of Himalayan rivers. Nature Geosci 5, 127–132. https://doi.org/10.1038/ngeo1356

Armstrong, R.L., Rittger, K., Brodzik, M.J., Racoviteanu, A., Barrett, A.P., Khalsa, S.-J.S., Raup, B., Hill, A.F., Khan, A.L., Wilson, A.M., Kayastha, R.B., Fetterer, F., Armstrong, B., 2019. Runoff from glacier ice and seasonal snow in High Asia: separating melt water sources in river flow. Reg Environ Change 19, 1249–1261. https://doi.org/10.1007/s10113-018-1429-0

Arora, M., Goel, N.K., Kesarwani, K., Malhotra, J., 2024. Integrated hydrological modelling and streamflow characterization of Gangotri Glacier meltwater. Appl Water Sci 14, 231. https://doi.org/10.1007/s13201-024-02283-3

Azam, M.F., Kargel, J.S., Shea, J.M., Nepal, S., Haritashya, U.K., Srivastava, S., Maussion, F., Qazi, N., Chevallier, P., Dimri, A.P., Kulkarni, A.V., Cogley, J.G., Bahuguna, I., 2021. Glaciohydrology of the Himalaya-Karakoram. Science 373, eabf3668. https://doi.org/10.1126/science.abf3668

Azam, M.F., Ramanathan, Al., Wagnon, P., Vincent, C., Linda, A., Berthier, E., Sharma, P., Mandal, A., Angchuk, T., Singh, V.B., Pottakkal, J.G., 2016. Meteorological conditions, seasonal and annual mass balances of Chhota Shigri Glacier, western Himalaya, India. Ann. Glaciol. 57, 328–338. https://doi.org/10.3189/2016AoG71A570

Azam, M.F., Wagnon, P., Berthier, E., Vincent, C., Fujita, K., Kargel, J.S., 2018. Review of the status and mass changes of Himalayan-Karakoram glaciers. J. Glaciol. 64, 61–74. https://doi.org/10.1017/jog.2017.86

Azam, M.F., Wagnon, P., Vincent, C., Ramanathan, A., Favier, V., Mandal, A., Pottakkal, J.G., 2014b. Processes governing the mass balance of Chhota Shigri Glacier (western Himalaya, India) assessed by point-scale surface energy balance measurements. The Cryosphere 8, 2195–2217. https://doi.org/10.5194/tc-8-2195-2014

Azam, M.F., Wagnon, P., Vincent, C., Ramanathan, A., Linda, A., Singh, V.B., 2014. Reconstruction of the annual mass balance of Chhota Shigri glacier, Western Himalaya, India, since 1969. Ann. Glaciol. 55, 69–80. https://doi.org/10.3189/2014AoG66A104

Azam, M.F., Wagnon, P., Vincent, C., Ramanathan, Al., Kumar, N., Srivastava, S., Pottakkal, J.G., Chevallier, P., 2019. Snow and ice melt contributions in a highly glacierized catchment of Chhota Shigri Glacier (India) over the last five decades. Journal of Hydrology 574, 760–773. https://doi.org/10.1016/j.jhydrol.2019.04.075

Azam, Mohd.F., 2021. Need of integrated monitoring on reference glacier catchments for future water security in Himalaya. Water Security 14, 100098. https://doi.org/10.1016/j.wasec.2021.100098

Banerjee, A., Azam, M.F., 2016. Temperature reconstruction from glacier length fluctuations in the Himalaya. Ann. Glaciol. 57, 189–198. https://doi.org/10.3189/2016AoG71A047

Barandun, M., Huss, M., Usubaliev, R., Azisov, E., Berthier, E., Kääb, A., Bolch, T., Hoelzle, M., 2018. Multi-decadal mass balance series of three Kyrgyz glaciers inferred from modelling constrained with repeated snow line observations. The Cryosphere 12, 1899–1919. https://doi.org/10.5194/tc-12-1899-2018

Barandun, M., Pohl, E., Naegeli, K., McNabb, R., Huss, M., Berthier, E., Saks, T., Hoelzle, M., 2021. Hot Spots of Glacier Mass Balance Variability in Central Asia. Geophysical Research Letters 48, e2020GL092084. https://doi.org/10.1029/2020GL092084

Beven, K., 2016. Facets of uncertainty: epistemic uncertainty, non-stationarity, likelihood, hypothesis testing, and communication. Hydrological Sciences Journal 61, 1652–1665. https://doi.org/10.1080/02626667.2015.1031761

Beven, K., 2004. Robert E. Horton's perceptual model of infiltration processes. Hydrological Processes 18, 3447–3460. https://doi.org/10.1002/hyp.5740

Beven, K., 1981. Kinematic subsurface stormflow. Water Resources Research 17, 1419–1424. https://doi.org/10.1029/WR017i005p01419

Beven, K., Germann, P., 1982. Macropores and water flow in soils. Water Resources Research 18, 1311–1325. https://doi.org/10.1029/WR018i005p01311

Bland, J.M., Altman, D., 1986. Statistical methods for assessing agreement between two methods of clinical measurement. The Lancet 327, 307–310. https://doi.org/10.1016/S0140-6736(86)90837-8

Bolch, T., Shea, J.M., Liu, S., Azam, M.F., Gao, Y., Gruber, S., Immerzeel, W.W., Kulkarni, A.V., Li, H., Tahir, A.A., Zhang, G., Zhang, Y., 2019. Status and Change of the Cryosphere in the Extended Hindu Kush Himalaya Region, in: Wester, P., Mishra, A., Mukherji, A., Shrestha, A.B. (Eds.), The Hindu Kush Himalaya Assessment. Springer International Publishing, Cham, pp. 209–255. https://doi.org/10.1007/978-3-319-92288-1_7

Bookhagen, B., Burbank, D.W., 2010. Toward a complete Himalayan hydrological budget: Spatiotemporal distribution of snowmelt and rainfall and their impact on river discharge. J. Geophys. Res. 115, F03019. https://doi.org/10.1029/2009JF001426

Bormann, K.J., Brown, R.D., Derksen, C., Painter, T.H., 2018. Estimating snow-cover trends from space. Nature Clim Change 8, 924–928. https://doi.org/10.1038/s41558-018-0318-3

Braithwaite, R.J., Raper, S.C.B., 2009. Estimating equilibrium-line altitude (ELA) from glacier inventory data. Ann. Glaciol. 50, 127–132. https://doi.org/10.3189/172756410790595930

Brown, R., Derksen, C., Wang, L., 2010. A multi-data set analysis of variability and change in Arctic spring snow cover extent, 1967–2008. J. Geophys. Res. 115, 2010JD013975. https://doi.org/10.1029/2010JD013975

Brun, Berthier, E., Wagnon, P., Kääb, A., Treichler, D., 2017. A spatially resolved estimate of High Mountain Asia glacier mass balances from 2000 to 2016. Nature Geosci 10, 668–673. https://doi.org/10.1038/ngeo2999

Brun, F., Dumont, M., Wagnon, P., Berthier, E., Azam, M.F., Shea, J.M., Sirguey, P., Rabatel, A., Ramanathan, Al., 2015. Seasonal changes in surface albedo of

Himalayan glaciers from MODIS data and links with the annual mass balance. The Cryosphere 9, 341–355. https://doi.org/10.5194/tc-9-341-2015

Bunting, P., Clewley, D., 2018. Atmospheric and Radiometric Correction of Satellite Imagery (ARCSI).

Buri, P., Pellicciotti, F., Steiner, J.F., Miles, E.S., Immerzeel, W.W., 2016. A grid-based model of backwasting of supraglacial ice cliffs on debris-covered glaciers. Ann. Glaciol. 57, 199–211. https://doi.org/10.3189/2016AoG71A059

Butt, M.J., Bilal, M., 2011. Application of snowmelt runoff model for water resource management. Hydrological Processes 25, 3735–3747. https://doi.org/10.1002/hyp.8099

Chandrasekharan, A., Ramsankaran, R., Pandit, A., Rabatel, A., 2018. Quantification of annual glacier surface mass balance for the Chhota Shigri Glacier, Western Himalayas, India using an Equilibrium-Line Altitude (ELA) based approach. International Journal of Remote Sensing 39, 9092–9112. https://doi.org/10.1080/01431161.2018.1506182

Cogley, J.G., 2009. Geodetic and direct mass-balance measurements: comparison and joint analysis. Ann. Glaciol. 50, 96–100. https://doi.org/10.3189/172756409787769744

Corradini, C., Morbidelli, R., Melone, F., 1998. On the interaction between infiltration and Hortonian runoff. Journal of Hydrology 204, 52–67. https://doi.org/10.1016/S0022-1694(97)00100-5

Cuffey, K.M., Paterson, W.S.B., 2010. The physics of glaciers, 4. ed. ed. Butterworth-Heineman, Amsterdam Heidelberg.

Davaze, L., Rabatel, A., Dufour, A., Hugonnet, R., Arnaud, Y., 2020. Region-Wide Annual Glacier Surface Mass Balance for the European Alps From 2000 to 2016. Front. Earth Sci. 8, 149. https://doi.org/10.3389/feart.2020.00149

Dehecq, A., Gourmelen, N., Gardner, A.S., Brun, F., Goldberg, D., Nienow, P.W., Berthier, E., Vincent, C., Wagnon, P., Trouvé, E., 2019. Twenty-first century glacier slowdown driven by mass loss in High Mountain Asia. Nature Geosci 12, 22–27. https://doi.org/10.1038/s41561-018-0271-9

Dimri, A.P., Niyogi, D., Barros, A.P., Ridley, J., Mohanty, U.C., Yasunari, T., Sikka, D.R., 2015. Western Disturbances: A review: WESTERN DISTURBANCE: A REVIEW. Rev. Geophys. 53, 225–246. https://doi.org/10.1002/2014RG000460

Dimri, A.P., Yasunari, T., Kotlia, B.S., Mohanty, U.C., Sikka, D.R., 2016. Indian winter monsoon: Present and past. Earth-Science Reviews 163, 297–322. https://doi.org/10.1016/j.earscirev.2016.10.008

Eeckman, J., Chevallier, P., Boone, A., Neppel, L., De Rouw, A., Delclaux, F., Koirala, D., 2017. Providing a non-deterministic representation of spatial variability of precipitation in the Everest region. Hydrol. Earth Syst. Sci. 21, 4879–4893. https://doi.org/10.5194/hess-21-4879-2017

Eeckman, J., Nepal, S., Chevallier, P., Camensuli, G., Delclaux, F., Boone, A., De Rouw, A., 2019. Comparing the ISBA and J2000 approaches for surface flows modelling at the local scale in the Everest region. Journal of Hydrology 569, 705–719. https://doi.org/10.1016/j.jhydrol.2018.12.022

Fatima, E., Hassan, M., Hasson, S.U., Ahmad, B., Ali, S.S.F., 2020. Future water availability from the western Karakoram under representative concentration pathways as simulated by CORDEX South Asia. Theor Appl Climatol 141, 1093–1108. https://doi.org/10.1007/s00704-020-03261-w

Favier, V., Wagnon, P., Chazarin, J., Maisincho, L., Coudrain, A., 2004. One-year measurements of surface heat budget on the ablation zone of Antizana Glacier 15, Ecuadorian Andes. J. Geophys. Res. 109, 2003JD004359. https://doi.org/10.1029/2003JD004359

Fowler, H.J., Archer, D.R., 2005. Hydro-climatological variability in the Upper Indus Basin and implications for water resources. Regional Hydrological Impacts of Climatic Change: Impact Assessment and Decision Making.

Fujita, K., 2008. Effect of precipitation seasonality on climatic sensitivity of glacier mass balance. Earth and Planetary Science Letters 276, 14–19. https://doi.org/10.1016/j.epsl.2008.08.028

Gaddam, V.K., Myneni, T.K., Kulkarni, A.V., Zhang, Y., 2022. Assessment of runoff in Chandra river basin of Western Himalaya using Remote Sensing and GIS Techniques. Environ Monit Assess 194, 145. https://doi.org/10.1007/s10661-022-09795-y

Gardelle, J., Berthier, E., Arnaud, Y., Kääb, A., 2013. Region-wide glacier mass balances over the Pamir-Karakoram-Himalaya during 1999–2011. The Cryosphere 7, 1263–1286. https://doi.org/10.5194/tc-7-1263-2013

Gardner, A.S., Moholdt, G., Cogley, J.G., Wouters, B., Arendt, A.A., Wahr, J., Berthier, E., Hock, R., Pfeffer, W.T., Kaser, G., Ligtenberg, S.R.M., Bolch, T., Sharp, M.J., Hagen, J.O., Van Den Broeke, M.R., Paul, F., 2013. A Reconciled Estimate of Glacier Contributions to Sea Level Rise: 2003 to 2009. Science 340, 852–857. https://doi.org/10.1126/science.1234532

Garg, P.K., Shukla, A., Azam, Mohd.F., 2024. Assessing the state, parameter-interlinkages and dynamic shift of glaciers in the western Himalaya. Cold Regions Science and Technology 217, 104052. https://doi.org/10.1016/j.coldregions.2023.104052

Garg, V., Thakur, P.K., Rajak, D.R., Aggarwal, S.P., Kumar, P., 2022. Spatio-temporal changes in radar zones and ELA estimation of glaciers in NyÅlesund using Sentinel-1 SAR. Polar Science 31, 100786. https://doi.org/10.1016/j.polar.2021.100786

Girona-Mata, M., Miles, E.S., Ragettli, S., Pellicciotti, F., 2019. High-Resolution Snowline Delineation From Landsat Imagery to Infer Snow Cover Controls in a Himalayan Catchment. Water Resources Research 55, 6754–6772. https://doi.org/10.1029/2019WR024935

Gupta, A., Jain, M.K., Pandey, R.P., Gupta, V., Saha, A., 2024. Evaluation of global precipitation products for meteorological drought assessment with respect to IMD station datasets over India. Atmospheric Research 297, 107104. https://doi.org/10.1016/j.atmosres.2023.107104

Haq, M.A., Azam, M.F., Vincent, C., 2021. Efficiency of artificial neural networks for glacier ice-thickness estimation: a case study in western Himalaya, India. J. Glaciol. 67, 671–684. https://doi.org/10.1017/jog.2021.19

Haq, M.A., Baral, P., Yaragal, S., Rahaman, G., 2020. Assessment of trends of land surface vegetation distribution, snow cover and temperature over entire Himachal Pradesh using MODIS datasets. Natural Resource Modeling 33, e12262. https://doi.org/10.1111/nrm.12262

Haritashya, U.K., Singh, P., Kumar, N., Gupta, R.P., 2006. Suspended sediment from the Gangotri Glacier: Quantification, variability and associations with discharge and air temperature. Journal of Hydrology 321, 116–130. https://doi.org/10.1016/j.jhydrol.2005.07.037

Harrison, S., Kargel, J.S., Huggel, C., Reynolds, J., Shugar, D.H., Betts, R.A., Emmer, A., Glasser, N., Haritashya, U.K., Klimeš, J., Reinhardt, L., Schaub, Y., Wiltshire, A., Regmi, D., Vilímek, V., 2018. Climate change and the global pattern of moraine-dammed glacial lake outburst floods. The Cryosphere 12, 1195–1209. https://doi.org/10.5194/tc-12-1195-2018

Hasson, S.U., 2016. Future Water Availability from Hindukush-Karakoram-Himalaya upper Indus Basin under Conflicting Climate Change Scenarios. Climate 4, 40. https://doi.org/10.3390/cli4030040

Hayat, H., Akbar, T.A., Tahir, A.A., Hassan, Q.K., Dewan, A., Irshad, M., 2019. Simulating Current and Future River-Flows in the Karakoram and Himalayan Regions of Pakistan Using Snowmelt-Runoff Model and RCP Scenarios. Water 11, 761. https://doi.org/10.3390/w11040761

Hewitt, K., 2005. The Karakoram Anomaly? Glacier Expansion and the 'Elevation Effect,' Karakoram Himalaya. Mountain Research and Development 25, 332–340. https://doi.org/10.1659/0276-4741(2005)025%255B0332:TKAGEA%255D2.0.CO;2

Hewlett, J.D., 1961. Soil moisture as a source of base flow from steep mountain watersheds. Southeastern Forest Experiment Station, 132.

Heynen, M., Pellicciotti, F., Carenzo, M., 2013. Parameter sensitivity of a distributed enhanced temperature-index melt model. Ann. Glaciol. 54, 311–321. https://doi.org/10.3189/2013AoG63A537

Hock, R., 2003. Temperature index melt modelling in mountain areas. Journal of Hydrology 282, 104–115. https://doi.org/10.1016/S0022-1694(03)00257-9

Hugonnet, R., McNabb, R., Berthier, E., Menounos, B., Nuth, C., Girod, L., Farinotti, D., Huss, M., Dussaillant, I., Brun, F., Kääb, A., 2021. Accelerated global glacier mass loss in the early twenty-first century. Nature 592, 726–731. https://doi.org/10.1038/s41586-021-03436-z

Huss, M., 2013. Density assumptions for converting geodetic glacier volume change to mass change. The Cryosphere 7, 877–887. https://doi.org/10.5194/tc-7-877-2013

Huss, M., Hock, R., 2018. Global-scale hydrological response to future glacier mass loss. Nature Clim Change 8, 135–140. https://doi.org/10.1038/s41558-017-0049-x

Hussain, Md.A., Azam, Mohd.F., Srivastava, S., Vinze, P., 2022. Positive mass budgets of high-altitude and debris-covered fragmented tributary glaciers in Gangotri Glacier System, Himalaya. Front. Earth Sci. 10, 978836. https://doi.org/10.3389/feart.2022.978836

ICIMOD, 2023. Improved 8-day version 6.1 Terra–Aqua MODIS cloud-free snow cover and Randolph Glacier Inventory 6.0 product for high-mountain Asia between 2002 and 2022. https://doi.org/10.26066/RDS.1973819

ICIMOD, 2021. Daily different contribution of total flow from HI-SPHY model for baseline period. https://doi.org/10.26066/RDS.22290

Immerzeel, Droogers, P., de Jong, S.M., Bierkens, M.F.P., 2009. Large-scale monitoring of snow cover and runoff simulation in Himalayan river basins using remote sensing. Remote Sensing of Environment 113, 40–49. https://doi.org/10.1016/j.rse.2008.08.010

Immerzeel, Lutz, A.F., Andrade, M., Bahl, A., Biemans, H., Bolch, T., Hyde, S., Brumby, S., Davies, B.J., Elmore, A.C., Emmer, A., Feng, M., Fernández, A., Haritashya, U., Kargel, J.S., Koppes, M., Kraaijenbrink, P.D.A., Kulkarni, A.V., Mayewski, P.A., Nepal, S., Pacheco, P., Painter, T.H., Pellicciotti, F., Rajaram, H., Rupper, S., Sinisalo, A., Shrestha, A.B., Viviroli, D., Wada, Y., Xiao, C., Yao, T., Baillie, J.E.M., 2020. Importance and vulnerability of the world's water towers. Nature 577, 364–369. https://doi.org/10.1038/s41586-019-1822-y

Immerzeel, W.W., Pellicciotti, F., Bierkens, M.F.P., 2013. Rising river flows throughout the twenty-first century in two Himalayan glacierized watersheds. Nature Geosci 6, 742–745. https://doi.org/10.1038/ngeo1896

Immerzeel, W.W., van Beek, L.P.H., Bierkens, M.F.P., 2010. Climate Change Will Affect the Asian Water Towers. Science 328, 1382–1385. https://doi.org/10.1126/science.1183188

Immerzeel, W.W., Van Beek, L.P.H., Konz, M., Shrestha, A.B., Bierkens, M.F.P., 2012. Hydrological response to climate change in a glacierized catchment in the Himalayas. Climatic Change 110, 721–736. https://doi.org/10.1007/s10584-011-0143-4

Jackson, M., Azam, M.F., Baral, P., Benestad, R., Brun, F., Muhammad, S., Pradhananga, S., Shrestha, F., Steiner, J.F., Thapa, A., 2023. Chapter 2: Consequences of climate change for the cryosphere in the Hindu Kush Himalaya, in: Water, Ice, Society, and Ecosystems in the Hindu Kush Himalaya: An Outlook. International Centre for Integrated Mountain Development (ICIMOD), pp. 17–71. https://doi.org/10.53055/ICIMOD.1030

Jain, S.K., Goswami, A., Saraf, A.K., 2010. Snowmelt runoff modelling in a Himalayan basin with the aid of satellite data. International Journal of Remote Sensing 31, 6603–6618. https://doi.org/10.1080/01431160903433893

Kendall, M.G., 1948. Rank Correlation Methods. Griffin.

Khadka, A., Brun, F., Wagnon, P., Shrestha, D., Sherpa, T.C., 2024. Surface energy and mass balance of Mera Glacier (Nepal, Central Himalaya) and their sensitivity to temperature and precipitation. J. Glaciol. 70, e80. https://doi.org/10.1017/jog.2024.42

Khadka, A., Wagnon, P., Brun, F., Shrestha, D., Lejeune, Y., Arnaud, Y., 2022. Evaluation of ERA5-Land and HARv2 Reanalysis Data at High Elevation in the Upper Dudh Koshi Basin (Everest Region, Nepal). Journal of Applied Meteorology and Climatology 61, 931–954. https://doi.org/10.1175/JAMC-D-21-0091.1

Khanal, S., Lutz, A.F., Kraaijenbrink, P.D.A., Van Den Hurk, B., Yao, T., Immerzeel, W.W., 2021. Variable 21st Century Climate Change Response for Rivers in High Mountain Asia at Seasonal to Decadal Time Scales. Water Resources Research 57, e2020WR029266. https://doi.org/10.1029/2020WR029266

Kiba, L.G., Rajkumari, S., Chiphang, N., Bandyopadhyay, A., Bhadra, A., 2021. Comparison of Snowmelt Runoff from the River Basins in the Eastern and Western Himalayan Region of India using SDSRM. J Indian Soc Remote Sens 49, 2291–2309. https://doi.org/10.1007/s12524-021-01384-9

Kraaijenbrink, P.D.A., Bierkens, M.F.P., Lutz, A.F., Immerzeel, W.W., 2017. Impact of a global temperature rise of 1.5 degrees Celsius on Asia's glaciers. Nature 549, 257–260. https://doi.org/10.1038/nature23878

Krishnan, R., Shrestha, Arun B., Ren, G., Rajbhandari, R., Saeed, S., Sanjay, J., Syed, Md.A., Vellore, R., Xu, Y., You, Q., Ren, Y., 2019. Unravelling Climate Change in the Hindu Kush Himalaya: Rapid Warming in the Mountains and Increasing Extremes, in: Wester, P., Mishra, A., Mukherji, A., Shrestha, Arun

Bhakta (Eds.), The Hindu Kush Himalaya Assessment. Springer International Publishing, Cham, pp. 57–97. https://doi.org/10.1007/978-3-319-92288-1_3

Kumar, K.K., Patwardhan, S.K., Kulkarni, A., Kamala, K., Rao, K.K., Jones, R., 2011. Simulated projections for summer monsoon climate over India by a high-resolution regional climate model (PRECIS). Current science 312–326.

Laha, S., Banerjee, A., Singh, A., Sharma, P., Thamban, M., 2021. The control of climate sensitivity on variability and change of summer runoff from two glacierised Himalayan catchments. https://doi.org/10.5194/hess-2021-499

Lei, L., Zeng, Z., Zhang, B., 2012. Method for Detecting Snow Lines From MODIS Data and Assessment of Changes in the Nianqingtanglha Mountains of the Tibet Plateau. IEEE J. Sel. Top. Appl. Earth Observations Remote Sensing 5, 769–776. https://doi.org/10.1109/JSTARS.2012.2200654

Li, K., Cao, B., Guan, W., Pan, B., Shangguan, D., 2022. Reconstructed annual glacier surface mass balance in the Ányêmaqên Mountains, Yellow River source, based on snow line altitude. J. Mt. Sci. 19, 1070–1081. https://doi.org/10.1007/s11629-021-7157-9

Li, Lei Huang, Quan Chen, Bang-sen Tian, 2012. Glacier Snow Line Detection on a Polarimetric SAR Image. IEEE Geosci. Remote Sensing Lett. 9, 584–588. https://doi.org/10.1109/LGRS.2011.2175697

Liu, C., Li, Z., Zhang, P., Tian, B., Zhou, J., Chen, Q., 2021. Variability of the snowline altitude in the eastern Tibetan Plateau from 1995 to 2016 using Google Earth Engine. J. Appl. Rem. Sens. 15, 048505. https://doi.org/10.1117/1.JRS.15.048505

Loibl, D., Richter, N., Grünberg, I., 2025. Remote sensing-derived time series of transient glacier snowline altitudes for High Mountain Asia, 1985–2021. Sci Data 12, 103. https://doi.org/10.1038/s41597-024-04309-6

Lutz, A.F., Immerzeel, W.W., Shrestha, A.B., Bierkens, M.F.P., 2014. Consistent increase in High Asia's runoff due to increasing glacier melt and precipitation. Nature Clim Change 4, 587–592. https://doi.org/10.1038/nclimate2237

Mandal, A., Angchuk, T., Azam, M.F., Ramanathan, A., Wagnon, P., Soheb, M., Singh, C., 2022. 11-year record of wintertime snow surface energy balance and sublimation at 4863 m a.s.l. on Chhota Shigri Glacier moraine (western Himalaya, India) (preprint). Snow/Energy Balance Obs/Modelling. https://doi.org/10.5194/tc-2021-386

Mandal, A., Ramanathan, A., Azam, Mohd.F., Angchuk, T., Soheb, M., Kumar, N., Pottakkal, J.G., Vatsal, S., Mishra, S., Singh, V.B., 2020. Understanding the interrelationships among mass balance, meteorology, discharge and surface velocity on Chhota Shigri Glacier over 2002–2019 using in situ measurements. J. Glaciol. 66, 727–741. https://doi.org/10.1017/jog.2020.42

Mann, H.B., 1945. Nonparametric Tests Against Trend. Econometrica 13, 245. https://doi.org/10.2307/1907187

Martinec, J., Rango, A., Roberts, R., 2007. Snowmelt Runoff Model (SRM) User's Manual. USDA Jornada Experimental Range, New Mexico State University, Las Cruces, NM 88003, USA.

Maurer, J.M., Schaefer, J.M., Rupper, S., Corley, A., 2019. Acceleration of ice loss across the Himalayas over the past 40 years. Sci. Adv. 5, eaav7266. https://doi.org/10.1126/sciadv.aav7266

Maurya, A.S., Shah, M., Deshpande, R.D., Bhardwaj, R.M., Prasad, A., Gupta, S.K., 2011. Hydrograph separation and precipitation source identification using stable water isotopes and conductivity: River Ganga at Himalayan foothills. Hydrological Processes 25, 1521–1530. https://doi.org/10.1002/hyp.7912

Maussion, F., Scherer, D., Mölg, T., Collier, E., Curio, J., Finkelnburg, R., 2014. Precipitation Seasonality and Variability over the Tibetan Plateau as Resolved by the High Asia Reanalysis*. Journal of Climate 27, 1910–1927. https://doi.org/10.1175/JCLI-D-13-00282.1

Mernild, S.H., Lipscomb, W.H., Bahr, D.B., Radić, V., Zemp, M., 2013. Global glacier changes: a revised assessment of committed mass losses and sampling uncertainties. The Cryosphere 7, 1565–1577. https://doi.org/10.5194/tc-7-1565-2013

Miles, E.S., Pellicciotti, F., Willis, I.C., Steiner, J.F., Buri, P., Arnold, N.S., 2016. Refined energy-balance modelling of a supraglacial pond, Langtang Khola, Nepal. Ann. Glaciol. 57, 29–40. https://doi.org/10.3189/2016AoG71A421

Muhammad, S., Thapa, A., 2020. An improved Terra–Aqua MODIS snow cover and Randolph Glacier Inventory 6.0 combined product (MOYDGL06*) for high-mountain Asia between 2002 and 2018. Earth Syst. Sci. Data 12, 345–356. https://doi.org/10.5194/essd-12-345-2020

Müller, T., Fischer, M., Lane, S.N., Schaefli, B., 2025. Separating snow and ice melt using water stable isotopes and glacio-hydrological modelling: towards improving the application of isotope analyses in highly glacierized catchments. The Cryosphere 19, 423–458. https://doi.org/10.5194/tc-19-423-2025

Naegeli, K., Huss, M., Hoelzle, M., 2019. Change detection of bare-ice albedo in the Swiss Alps. The Cryosphere 13, 397–412. https://doi.org/10.5194/tc-13-397-2019

Neitsch, S.L., Arnold, J.G., Kiniry, J.R., Williams, J.R., 2009. Overview of soil and water assessment tool (SWAT) model. Tier B 8, 3–23.

Nepal, S., Krause, P., Flügel, W.-A., Fink, M., Fischer, C., 2014. Understanding the hydrological system dynamics of a glaciated alpine catchment in the Himalayan region using the J2000 hydrological model: HYDROLOGICAL SYSTEM DYNAMICS OF HIMALAYA RIVERS. Hydrol. Process. 28, 1329–1344. https://doi.org/10.1002/hyp.9627

Nepal, S., Shrestha, A.B., 2015. Impact of climate change on the hydrological regime of the Indus, Ganges and Brahmaputra river basins: a review of the literature. International Journal of Water Resources Development 31, 201–218. https://doi.org/10.1080/07900627.2015.1030494

Nepal, S., Steiner, J.F., Allen, S., Azam, Mohd.F., Bhuchar, S., Biemans, H., Dhakal, M., Khanal, S., Li, D., Lutz, A., Pradhananga, S., Ritzema, R., Stoffel, M., Stuart-Smith, R., 2023. Chapter 3: Consequences of cryospheric change for water resources and hazards in the Hindu Kush Himalaya, in: Water, Ice, Society, and Ecosystems in the Hindu Kush Himalaya: An Outlook. International Centre for Integrated Mountain Development (ICIMOD), pp. 73–121. https://doi.org/10.53055/ICIMOD.1031

Oerlemans, J., 1992. Climate sensitivity of glaciers in southern Norway: application of an energy-balance model to Nigardsbreen, Hellstugubreen and Alfotbreen. J. Glaciol. 38, 223–232. https://doi.org/10.3189/S0022143000003634

Oerlemans, J., Anderson, B., Hubbard, A., Huybrechts, P., Jóhannesson, T., Knap, W.H., Schmeits, M., Stroeven, A.P., van de Wal, R.S.W., Wallinga, J., Zuo, Z., 1998. Modelling the response of glaciers to climate warming. Climate Dynamics 14, 267–274. https://doi.org/10.1007/s003820050222

Oien, R.P., Rea, B.R., Spagnolo, M., Barr, I.D., Bingham, R.G., 2022. Testing the area–altitude balance ratio (AABR) and accumulation–area ratio (AAR) methods of calculating glacier equilibrium-line altitudes. J. Glaciol. 68, 357–368. https://doi.org/10.1017/jog.2021.100

Otsu, N., 1979. A Threshold Selection Method from Gray-Level Histograms. IEEE Trans. Syst., Man, Cybern. 9, 62–66. https://doi.org/10.1109/TSMC.1979.4310076

Owen, L.A., Benn, D.I., 2005. Equilibrium-line altitudes of the Last Glacial Maximum for the Himalaya and Tibet: an assessment and evaluation of results. Quaternary International 138–139, 55–78. https://doi.org/10.1016/j.quaint.2005.02.006

Painter, T.H., Rittger, K., McKenzie, C., Slaughter, P., Davis, R.E., Dozier, J., 2009. Retrieval of subpixel snow covered area, grain size, and albedo from MODIS. Remote Sensing of Environment 113, 868–879. https://doi.org/10.1016/j.rse.2009.01.001

Panday, P.K., Williams, C.A., Frey, K.E., Brown, M.E., 2014. Application and evaluation of a snowmelt runoff model in the Tamor River basin, Eastern Himalaya using a Markov Chain Monte Carlo (MCMC) data assimilation approach. Hydrological Processes 28, 5337–5353. https://doi.org/10.1002/hyp.10005

Pelto, M., 2011. Utility of late summer transient snowline migration rate on Taku Glacier, Alaska. The Cryosphere 5, 1127–1133. https://doi.org/10.5194/tc-5-1127-2011

Pepin, N., Bradley, R., Diaz, H., Baraër, M., Caceres, E., Forsythe, N., Fowler, H., Greenwood, G., Hashmi, M., Liu, X., Miller, J., 2015. Elevation-dependent warming in mountain regions of the world. Nature Clim Change 5, 424–430. https://doi.org/10.1038/nclimate2563

PlanetLabs, 2021. Planet labs pbc.

Pörtner, H.-O., Roberts, D.C., Tignor, M., Poloczanska, E.S., Mintenbeck, K., Alegría, A., Craig, M., Langsdorf, S., Löschke, S., Möller, V., Okem, A., Rama, B., 2022. Climate Change 2022: Impacts, Adaptation, and Vulnerability. Contribution of Working Group II to the Sixth Assessment Report of the Intergovernmental Panel on Climate Change. IPCC, Cambridge University Press. In Press.

Pratap, B., Sharma, P., Patel, L., Singh, A.T., Gaddam, V.K., Oulkar, S., Thamban, M., 2019. Reconciling High Glacier Surface Melting in Summer with Air Temperature in the Semi-Arid Zone of Western Himalaya. Water 11, 1561. https://doi.org/10.3390/w11081561

Prieur, C., Rabatel, A., Thomas, J.-B., Farup, I., Chanussot, J., 2022. Machine Learning Approaches to Automatically Detect Glacier Snow Lines on Multi-Spectral Satellite Images. Remote Sensing 14, 3868. https://doi.org/10.3390/rs14163868

Pritchard, H.D., 2019. Asia's shrinking glaciers protect large populations from drought stress. Nature 569, 649–654. https://doi.org/10.1038/s41586-019-1240-1

Rabatel, A., Bermejo, A., Loarte, E., Soruco, A., Gomez, J., Leonardini, G., Vincent, C., Sicart, J.E., 2012. Can the snowline be used as an indicator of the equilibrium line and mass balance for glaciers in the outer tropics? J. Glaciol. 58, 1027–1036. https://doi.org/10.3189/2012JoG12J027

Rabatel, A., Letréguilly, A., Dedieu, J.-P., Eckert, N., 2013. Changes in glacier equilibrium-line altitude in the western Alps from 1984 to 2010: evaluation by remote sensing and modeling of the morpho-topographic and climate controls. The Cryosphere 7, 1455–1471. https://doi.org/10.5194/tc-7-1455-2013

Rabatel, A., Sirguey, P., Drolon, V., Maisongrande, P., Arnaud, Y., Berthier, E., Davaze, L., Dedieu, J.-P., Dumont, M., 2017. Annual and Seasonal Glacier-Wide Surface Mass Balance Quantified from Changes in Glacier Surface State: A Review on Existing Methods Using Optical Satellite Imagery. Remote Sensing 9, 507. https://doi.org/10.3390/rs9050507

Rabatel, Dedieu, J.P., Vincent, C., 2016. Spatio-temporal changes in glacier-wide mass balance quantified by optical remote sensing on 30 glaciers in the French Alps for the period 1983–2014. J. Glaciol. 62, 1153–1166. https://doi.org/10.1017/jog.2016.113

Racoviteanu, A.E., Armstrong, R., Williams, M.W., 2013. Evaluation of an ice ablation model to estimate the contribution of melting glacier ice to annual discharge in the Nepal Himalaya: GLACIAL CONTRIBUTIONS TO ANNUAL STREAMFLOW IN NEPAL HIMALAYA. Water Resour. Res. 49, 5117–5133. https://doi.org/10.1002/wrcr.20370

Racoviteanu, A.E., Nicholson, L., Glasser, N.F., 2021. Surface composition of debris-covered glaciers across the Himalaya using linear spectral unmixing of Landsat 8 OLI imagery. The Cryosphere 15, 4557–4588. https://doi.org/10.5194/tc-15-4557-2021

Racoviteanu, A.E., Paul, F., Raup, B., Khalsa, S.J.S., Armstrong, R., 2009. Challenges and recommendations in mapping of glacier parameters from space: results of the 2008 Global Land Ice Measurements from Space (GLIMS) workshop, Boulder, Colorado, USA. Ann. Glaciol. 50, 53–69. https://doi.org/10.3189/172756410790595804

Racoviteanu, A.E., Rittger, K., Armstrong, R., 2019. An Automated Approach for Estimating Snowline Altitudes in the Karakoram and Eastern Himalaya From Remote Sensing. Front. Earth Sci. 7, 220. https://doi.org/10.3389/feart.2019.00220

Racoviteanu, A.E., Williams, M.W., Barry, R.G., 2008. Optical Remote Sensing of Glacier Characteristics: A Review with Focus on the Himalaya. Sensors 8, 3355–3383. https://doi.org/10.3390/s8053355

Ragettli, S., Pellicciotti, F., 2012. Calibration of a physically based, spatially distributed hydrological model in a glacierized basin: On the use of knowledge from glaciometeorological processes to constrain model parameters. Water Resources Research 48, 2011WR010559. https://doi.org/10.1029/2011WR010559

Ragettli, S., Pellicciotti, F., Bordoy, R., Immerzeel, W.W., 2013. Sources of uncertainty in modeling the glaciohydrological response of a Karakoram watershed to climate change: Sources of uncertainty in glaciohydrological modeling. Water Resour. Res. 49, 6048–6066. https://doi.org/10.1002/wrcr.20450

Rai, S.P., Singh, D., Jacob, N., Rawat, Y.S., Arora, M., BhishmKumar, 2019. Identifying contribution of snowmelt and glacier melt to the Bhagirathi River (Upper Ganga) near snout of the Gangotri Glacier using environmental isotopes. CATENA 173, 339–351. https://doi.org/10.1016/j.catena.2018.10.031

Rani, S.I., T, A., George, J.P., Rajagopal, E.N., Renshaw, R., Maycock, A., Barker, D.M., Rajeevan, M., 2021. IMDAA: High Resolution Satellite-era Reanalysis for the Indian Monsoon Region. Journal of Climate 1–78. https://doi.org/10.1175/JCLI-D-20-0412.1

Rastner, P., Nicholson, L., Sailer, R., Notarnicola, C., Prinz, R., 2015. Mapping the snow line altitude for large glacier samples from multitemporal Landsat imagery, in: 2015 8th International Workshop on the Analysis of Multitemporal Remote Sensing Images (Multi-Temp). Presented at the 2015 8th International Workshop on the Analysis of Multitemporal Remote Sensing Images (Multi-Temp), IEEE, Annecy, France, pp. 1–4. https://doi.org/10.1109/Multi-Temp.2015.7245788

Rastner, P., Prinz, R., Notarnicola, C., Nicholson, L., Sailer, R., Schwaizer, G., Paul, F., 2019. On the Automated Mapping of Snow Cover on Glaciers and Calculation of Snow Line Altitudes from Multi-Temporal Landsat Data. Remote Sensing 11, 1410. https://doi.org/10.3390/rs11121410

Reid, T.D., Carenzo, M., Pellicciotti, F., Brock, B.W., 2012. Including debris cover effects in a distributed model of glacier ablation. J. Geophys. Res. 117, 2012JD017795. https://doi.org/10.1029/2012JD017795

Sakai, A., 2019. Brief communication: Updated GAMDAM glacier inventory over high-mountain Asia. The Cryosphere 13, 2043–2049. https://doi.org/10.5194/tc-13-2043-2019

Salim, M., Pandey, A.C., 2021. Estimation of temporal snowmelt runoff using geospatial technique in Gangotri glacier basin, Uttarakhand, India. Remote Sensing Applications: Society and Environment 24, 100660. https://doi.org/10.1016/j.rsase.2021.100660

Sangrey, D.A., Harrop-Williams, K.O., Klaiber, J.A., 1984. Predicting Ground-Water Response to Precipitation. J. Geotech. Engrg. 110, 957–975. https://doi.org/10.1061/(ASCE)0733-9410(1984)110:7(957)

Sattar, A., Cook, K.L., Rai, S.K., Berthier, E., Allen, S., Rinzin, S., De Vries, M.V.W., Haeberli, W., Kushwaha, P., Shugar, D.H., Emmer, A., Haritashya, U.K., Frey, H., Rao, P., Gurudin, K.S.K., Rai, P., Rajak, R., Hossain, F., Huggel, C., Mergili, M., Azam, Mohd.F., Gascoin, S., Carrivick, J.L., Bell, L.E., Ranjan, R.K., Rashid, I., Kulkarni, Anil.V., Petley, D., Schwanghart, W., Watson, C.S., Islam, N., Gupta, M.D., Lane, S.N., Bhat, S.Y., 2025. The Sikkim flood of October 2023: Drivers, causes, and impacts of a multihazard cascade. Science 387, eads2659. https://doi.org/10.1126/science.ads2659

Savéan, M., Delclaux, F., Chevallier, P., Wagnon, P., Gonga-Saholiariliva, N., Sharma, R., Neppel, L., Arnaud, Y., 2015. Water budget on the Dudh Koshi River (Nepal): Uncertainties on precipitation. Journal of Hydrology 531, 850–862. https://doi.org/10.1016/j.jhydrol.2015.10.040

Scherler, D., Wulf, H., Gorelick, N., 2018. Global Assessment of Supraglacial Debris-Cover Extents. Geophysical Research Letters 45. https://doi.org/10.1029/2018GL080158

Sen, P.K., 1968. Estimates of the Regression Coefficient Based on Kendall's Tau. Journal of the American Statistical Association 63, 1379–1389. https://doi.org/10.1080/01621459.1968.10480934

Shea, J.M., Immerzeel, W.W., Wagnon, P., Vincent, C., Bajracharya, S., 2015. Modelling glacier change in the Everest region, Nepal Himalaya. The Cryosphere 9, 1105–1128. https://doi.org/10.5194/tc-9-1105-2015

Shean, D.E., Bhushan, S., Montesano, P., Rounce, D.R., Arendt, A., Osmanoglu, B., 2020. A Systematic, Regional Assessment of High Mountain Asia Glacier

Mass Balance. Front. Earth Sci. 7, 363. https://doi.org/10.3389/feart.2019.00363

Sherpa, S.F., Wagnon, P., Brun, F., Berthier, E., Vincent, C., Lejeune, Y., Arnaud, Y., Kayastha, R.B., Sinisalo, A., 2017. Contrasted surface mass balances of debris-free glaciers observed between the southern and the inner parts of the Everest region (2007–15). J. Glaciol. 63, 637–651. https://doi.org/10.1017/jog.2017.30

Shrestha, A.B., Agrawal, N.K., Alfthan, B., Bajracharya, S.R., Maréchal, J., Oort, B.V., 2015. The Himalayan Climate and Water Atlas: impact of climate change on water resources in five of Asia’s major river basins. The Himalayan Climate and Water Atlas: impact of climate change on water resources in five of Asia’s major river basins.

Shrestha, S., Nepal, S., 2019. Water Balance Assessment under Different Glacier Coverage Scenarios in the Hunza Basin. Water 11, 1124. https://doi.org/10.3390/w11061124

Siemens, K., Dibike, Y., Shrestha, R.R., Prowse, T., 2021. Runoff projection from an alpine watershed in western Canada: application of a snowmelt runoff model. Water 13, 1199.

Singh, A.T., Rahaman, W., Sharma, P., Laluraj, Patel, L.K., Pratap, B., Gaddam, V.K., Thamban, M., 2019. Moisture Sources for Precipitation and Hydrograph Components of the Sutri Dhaka Glacier Basin, Western Himalayas. Water 11, 2242. https://doi.org/10.3390/w11112242

Singh, A.T., Sharma, P., Sharma, C., Laluraj, C.M., Patel, L., Pratap, B., Oulkar, S., Thamban, M., 2020. Water discharge and suspended sediment dynamics in the Chandra River, Western Himalaya. J Earth Syst Sci 129, 206. https://doi.org/10.1007/s12040-020-01455-4

Singh, J., Singh, V., Ojha, C.S.P., Arora, M.K., 2023. Assessment of recent changes (2011–2020) in glacier thickness and runoff variability in Gangotri glacier, India. Hydrological Sciences Journal 68, 2223–2242. https://doi.org/10.1080/02626667.2023.2258861

Singh, Jain, S.K., Shukla, S., 2021a. Glacier change and glacier runoff variation in the Himalayan Baspa river basin. Journal of Hydrology 593, 125918. https://doi.org/10.1016/j.jhydrol.2020.125918

Singh, Laluraj, C.M., Sharma, P., Redkar, B.L., Patel, L.K., Pratap, B., Oulkar, S., Thamban, M., 2021b. Hydrograph apportionment of the Chandra River draining from a semi-arid region of the Upper Indus Basin, western Himalaya. Science of The Total Environment 780, 146500. https://doi.org/10.1016/j.scitotenv.2021.146500

Singh, P., Haritashya, U.K., Kumar, N., 2008. Modelling and estimation of different components of streamflow for Gangotri Glacier basin, Himalayas / Modélisation et estimation des différentes composantes de l’écoulement fluviatile du bassin du Glacier Gangotri, Himalaya. Hydrological Sciences Journal 53, 309–322. https://doi.org/10.1623/hysj.53.2.309

Singh, P., Haritashya, U.K., Kumar, N., Singh, Y., 2006. Hydrological characteristics of the Gangotri Glacier, central Himalayas, India. Journal of Hydrology 327, 55–67. https://doi.org/10.1016/j.jhydrol.2005.11.060

Singh, P., Haritashya, U.K., Ramasastri, K.S., Kumar, N., 2005. Prevailing weather conditions during summer seasons around Gangotri Glacier. Current science 753–760.

Singh, P., Jain, S.K., 2003. Modelling of streamflow and its components for a large Himalayan basin with predominant snowmelt yields. Hydrological Sciences Journal 48, 257–276. https://doi.org/10.1623/hysj.48.2.257.44693

Singh, P., Jain, S.K., 2002. Snow and glacier melt in the Satluj River at Bhakra Dam in the western Himalayan region. Hydrological Sciences Journal 47, 93–106. https://doi.org/10.1080/02626660209492910

Singh, P., Kumar, A., Kishore, N., 2011. Meltwater storage and delaying characteristics of Gangotri Glacier (Indian Himalayas) during ablation season. Hydrological Processes 25, 159–166. https://doi.org/10.1002/hyp.7828

Sloan, P.G., Moore, I.D., 1984. Modeling subsurface stormflow on steeply sloping forested watersheds. Water Resources Research 20, 1815–1822. https://doi.org/10.1029/WR020i012p01815

Soheb, M., Bastian, P., Schmidt, S., Singh, S., Kaushik, H., Ramanathan, A., Nüsser, M., 2024. Surface and subsurface flow of a glacierised catchment in the cold-arid region of Ladakh, Trans-Himalaya. Journal of Hydrology 635, 131063. https://doi.org/10.1016/j.jhydrol.2024.131063

Srivastava, S., Azam, M.F., 2022a. Mass- and Energy-Balance Modeling and Sublimation Losses on Dokriani Bamak and Chhota Shigri Glaciers in Himalaya Since 1979. Front. Water 4, 874240. https://doi.org/10.3389/frwa.2022.874240

Srivastava, S., Azam, M.F., 2022b. Functioning of glacierized catchments in Monsoon and Alpine regimes of Himalaya. Journal of Hydrology 609, 127671. https://doi.org/10.1016/j.jhydrol.2022.127671

Srivastava, S., Azam, Mohd.F., Thakur, P.K., 2024. Linking basin-scale hydrology with climatic parameters in western Himalaya: Application of satellite data, temperature index modelling and in-situ observations. Geoscience Frontiers 15, 101936. https://doi.org/10.1016/j.gsf.2024.101936

Srivastava, S., Garg, P.K., Azam, Mohd.F., 2022. Seven Decades of Dimensional and Mass Balance Changes on Dokriani Bamak and Chhota Shigri Glaciers, Indian Himalaya, Using Satellite Data and Modelling. J Indian Soc Remote Sens 50, 37–54. https://doi.org/10.1007/s12524-021-01455-x

Tadono, T., Ishida, H., Oda, F., Naito, S., Minakawa, K., Iwamoto, H., 2014. Precise Global DEM Generation by ALOS PRISM. ISPRS Ann. Photogramm. Remote Sens. Spatial Inf. Sci. II–4, 71–76. https://doi.org/10.5194/isprsannals-II-4-71-2014

Tahir, A.A., Chevallier, P., Arnaud, Y., Neppel, L., Ahmad, B., 2011. Modeling snowmelt-runoff under climate scenarios in the Hunza River basin, Karakoram Range, Northern Pakistan. Journal of Hydrology 409, 104–117. https://doi.org/10.1016/j.jhydrol.2011.08.035

Tahir, A.A., Hakeem, S.A., Hu, T., Hayat, H., Yasir, M., 2019. Simulation of snowmelt-runoff under climate change scenarios in a data-scarce mountain environment. International Journal of Digital Earth 12, 910–930. https://doi.org/10.1080/17538947.2017.1371254

Takaku, J., Tadono, T., 2017. Quality updates of 'AW3D' global DSM generated from ALOS PRISM, in: 2017 IEEE International Geoscience and Remote Sensing Symposium (IGARSS). Presented at the 2017 IEEE International Geoscience and Remote Sensing Symposium (IGARSS), IEEE, Fort Worth, TX, pp. 5666–5669. https://doi.org/10.1109/IGARSS.2017.8128293

Tawde, S.A., Kulkarni, A.V., Bala, G., 2016. Estimation of Glacier Mass Balance on a Basin Scale:An Approach Based on Satellite-Derived Snowlines and a

Temperature Index Model. Current Science 111, 1977. https://doi.org/10.18520/cs/v111/i12/1977-1989

Terink, W., Lutz, A.F., Simons, G.W.H., Immerzeel, W.W., Droogers, P., 2015. SPHY v2.0: Spatial Processes in HYdrology. Geosci. Model Dev. 8, 2009–2034. https://doi.org/10.5194/gmd-8-2009-2015

Thayyen, R.J., Gergan, J.T., 2010. Role of glaciers in watershed hydrology: a preliminary study of a Himalayan catchment. The Cryosphere 4, 115–128. https://doi.org/10.5194/tc-4-115-2010

Theia-Land, 2022. Venµs surface reflectance. Technical report CNES.

USGS, 2024. Landsat 7 Science Data User Handbook.

USGS, 2019. Landsat 8 Science Data User Handbook.

Vatsal, S., Azam, M.F., Bhardwaj, A., Mandal, A., Bahuguna, I., Ramanathan, A., Raju, N.J., Tomar, S.S., 2024. Glacier area change (1993–2019) and its relationship to debris cover, proglacial lakes, and morphological parameters in the Chandra-Bhaga Basin, Western Himalaya, India. J. Mt. Sci. 21, 1287–1306. https://doi.org/10.1007/s11629-023-8277-1

Veh, G., Korup, O., Walz, A., 2020. Hazard from Himalayan glacier lake outburst floods. Proc. Natl. Acad. Sci. U.S.A. 117, 907–912. https://doi.org/10.1073/pnas.1914898117

Venetis, C., 1969. A STUDY ON THE RECESSION OF UNCONFINED ACQUIFERS. International Association of Scientific Hydrology. Bulletin 14, 119–125. https://doi.org/10.1080/02626666909493759

Vermote, E.F., Tanre, D., Deuze, J.L., Herman, M., Morcette, J.-J., 1997. Second Simulation of the Satellite Signal in the Solar Spectrum, 6S: an overview. IEEE Trans. Geosci. Remote Sensing 35, 675–686. https://doi.org/10.1109/36.581987

Vishwakarma, B.D., Ramsankaran, R., Azam, Mohd.F., Bolch, T., Mandal, A., Srivastava, S., Kumar, P., Sahu, R., Navinkumar, P.J., Tanniru, S.R., Javed, A., Soheb, M., Dimri, A.P., Yadav, M., Devaraju, B., Chinnasamy, P., Reddy, M.J., Murugesan, G.P., Arora, M., Jain, S.K., Ojha, C.S.P., Harrison, S., Bamber, J., 2022. Challenges in Understanding the Variability of the Cryosphere in the Himalaya and Its Impact on Regional Water Resources. Front. Water 4, 909246. https://doi.org/10.3389/frwa.2022.909246

Wagnon, P., Brun, F., Khadka, A., Berthier, E., Shrestha, D., Vincent, C., Arnaud, Y., Six, D., Dehecq, A., Ménégoz, M., Jomelli, V., 2021. Reanalysing the 2007–19 glaciological mass-balance series of Mera Glacier, Nepal, Central Himalaya, using geodetic mass balance. J. Glaciol. 67, 117–125. https://doi.org/10.1017/jog.2020.88

Wagnon, P., Vincent, C., Arnaud, Y., Berthier, E., Vuillermoz, E., Gruber, S., Ménégoz, M., Gilbert, A., Dumont, M., Shea, J.M., Stumm, D., Pokhrel, B.K., 2013. Seasonal and annual mass balances of Mera and Pokalde glaciers (Nepal Himalaya) since 2007. The Cryosphere 7, 1769–1786. https://doi.org/10.5194/tc-7-1769-2013

Wuebbles, D.J., Fahey, D.W., Hibbard, K.A., 2017. Climate science special report: fourth national climate assessment.

Yuwei, W., Jianqiao, H., Zhongming, G., Anan, C., 2014. Limitations in identifying the equilibrium-line altitude from the optical remote-sensing derived snowline in the Tien Shan, China. J. Glaciol. 60, 1093–1100. https://doi.org/10.3189/2014JoG13J221

Zemp, M., Hoelzle, M., Haeberli, W., 2009. Six decades of glacier mass-balance observations: a review of the worldwide monitoring network. Ann. Glaciol. 50, 101–111. https://doi.org/10.3189/172756409787769591

Zhan, Y.-J., Ren, G.-Y., Shrestha, A.B., Rajbhandari, R., Ren, Y.-Y., Sanjay, J., Xu, Y., Sun, X.-B., You, Q.-L., Wang, S., 2017. Changes in extreme precipitation events over the Hindu Kush Himalayan region during 1961–2012. Advances in Climate Change Research 8, 166–175. https://doi.org/10.1016/j.accre.2017.08.002

Zhang, G., Xie, H., Yao, T., Li, H., Duan, S., 2014. Quantitative water resources assessment of Qinghai Lake basin using Snowmelt Runoff Model (SRM). Journal of Hydrology 519, 976–987. https://doi.org/10.1016/j.jhydrol.2014.08.022

Zhang, Y., Liu, S., Y.D., 2006. Observed degree-day factors and their spatial variation on glaciers in western China. Ann. Glaciol. 43, 301–306. https://doi.org/10.3189/172756406781811952

# APPENDIX A

This appendix contains Table S1, which provides values for all the processed SLAs for Dudh Koshi basin over the period 2015−2023

Table S 1 Summary statistics of S2/L8 basin-wide SLAs for the Dudh Koshi basin (462 glaciers) over the period 2015–2023; basin-wide $SLA_{max}$ is marked in bold

| Date | #SLAs | Min.(m) | Max.(m) | Mean (m) | STD (m) |
|---|---|---|---|---|---|
| 2015-05-25 | 6 | 5107 | 5309 | 5208 | 81.0 |
| 2015-07-12 | 24 | 5145 | 5517 | 5354 | 98.4 |
| 2015-09-30 | 21 | 5033 | 5377 | 5239 | 95.0 |
| 2015-11-01 | 22 | 4954 | 5419 | 5222 | 117.4 |
| 2015-11-17 | 49 | 5056 | 5682 | 5444 | 148.2 |
| 2015-12-19 | 11 | 5096 | 5505 | 5352 | 120.3 |
| 2016-01-14 | 95 | 5052 | 5833 | **5517** | 142.5 |
| 2016-04-13 | 97 | 4971 | 5583 | 5381 | 123.7 |
| 2016-10-30 | 88 | 4989 | 5678 | 5403 | 146.7 |
| 2016-11-03 | 44 | 5032 | 5604 | 5396 | 137.2 |
| 2016-11-19 | 46 | 5454 | 5695 | 5438 | 122.7 |
| 2016-11-29 | 88 | 4994 | 5724 | 5434 | 144.3 |
| 2016-12-09 | 95 | 5096 | 5747 | 5468 | 133.6 |
| 2016-12-29 | 91 | 5084 | 5780 | **5481** | 145.1 |
| 2017-01-08 | 58 | 4658 | 5620 | 5364 | 174.3 |
| 2017-01-18 | 73 | 4754 | 5704 | 5411 | 155.7 |
| 2017-04-18 | 30 | 5082 | 5575 | 5329 | 137.2 |
| 2017-10-15 | 99 | 5157 | 5734 | 5470 | 134.5 |
| 2017-10-30 | 70 | 4818 | 5596 | 5357 | 163.6 |
| 2017-11-06 | 39 | 5090 | 5673 | 5402 | 130.3 |
| 2017-11-19 | 93 | 4992 | 5684 | 5420 | 151.4 |
| 2017-11-22 | 46 | 5024 | 5791 | 5460 | 165.1 |
| 2017-11-24 | 67 | 5016 | 5773 | 5470 | 163.1 |

| | | | | | |
|---|---|---|---|---|---|
| 2017-12-09 | 88 | 5216 | 5807 | 5523 | 141.0 |
| 2017-12-14 | 88 | 5229 | 5820 | 5528 | 140.4 |
| 2017-12-29 | 88 | 5137 | 5854 | **5553** | 150.4 |
| 2018-01-03 | 50 | 4653 | 5704 | 5381 | 213.2 |
| 2018-01-08 | 27 | 4855 | 5713 | 5400 | 192.7 |
| 2018-01-18 | 28 | 4863 | 5648 | 5383 | 178.4 |
| 2018-01-23 | 37 | 4854 | 5708 | 5340 | 200.3 |
| 2018-01-28 | 81 | 4680 | 5655 | 5393 | 187.4 |
| 2018-04-23 | 42 | 4865 | 5448 | 5249 | 122.6 |
| 2018-05-08 | 43 | 4898 | 5438 | 5265 | 105.1 |
| 2018-10-15 | 85 | 5102 | 5672 | 5473 | 121.0 |
| 2018-10-20 | 99 | 5145 | 5817 | 5573 | 128.4 |
| 2018-10-24 | 37 | 5204 | 5702 | 5506 | 136.9 |
| 2018-10-30 | 95 | 5110 | 5795 | 5544 | 139.8 |
| 2018-11-04 | 90 | 5119 | 5737 | 5508 | 135.2 |
| 2018-11-09 | 75 | 5227 | 5740 | 5545 | 120.4 |
| 2018-11-14 | 95 | 5239 | 5821 | 5558 | 132.5 |
| 2018-11-24 | 92 | 5252 | 5820 | 5586 | 116.1 |
| 2018-11-25 | 40 | 5253 | 5856 | 5617 | 141.2 |
| 2018-12-04 | 89 | 5256 | 5900 | **5624** | 131.8 |
| 2018-12-09 | 89 | 5144 | 5843 | 5559 | 153.6 |
| 2018-12-14 | 62 | 5031 | 5680 | 5448 | 159.5 |
| 2018-12-19 | 50 | 4661 | 5607 | 5290 | 194.1 |
| 2018-12-24 | 59 | 5129 | 5559 | 5371 | 109.4 |
| 2018-12-29 | 36 | 5005 | 5617 | 5402 | 155.4 |
| 2019-01-13 | 63 | 4887 | 5704 | 5433 | 167.3 |
| 2019-01-18 | 64 | 4877 | 5592 | 5372 | 152.6 |
| 2019-01-28 | 68 | 4625 | 5794 | 5411 | 213.0 |
| 2019-05-08 | 62 | 4900 | 5527 | 5323 | 139.0 |
| 2019-10-15 | 80 | 4811 | 5690 | 5356 | 174.1 |
| 2019-10-27 | 29 | 4982 | 5462 | 5278 | 120.1 |

| | | | | | |
|---|---|---|---|---|---|
| 2019-11-12 | 37 | 5210 | 5579 | 5393 | 109.4 |
| 2019-11-19 | 87 | 4960 | 5699 | 5406 | 144.4 |
| 2019-11-24 | 27 | 5228 | 5627 | 5419 | 119.3 |
| 2019-12-04 | 100 | 4984 | 5752 | **5476** | 151.8 |
| 2019-12-09 | 77 | 5033 | 5615 | 5398 | 130.9 |
| 2019-12-19 | 49 | 4627 | 5537 | 5263 | 184.3 |
| 2019-12-24 | 46 | 4651 | 5577 | 5335 | 184.4 |
| 2019-12-29 | 46 | 4907 | 5611 | 5364 | 161.8 |
| 2020-01-13 | 54 | 4578 | 5590 | 5298 | 204.5 |
| 2020-01-23 | 63 | 4952 | 5788 | 5467 | 183.3 |
| 2020-01-28 | 56 | 4594 | 5580 | 5319 | 187.7 |
| 2020-04-02 | 19 | 4657 | 5303 | 5131 | 157.0 |
| 2020-04-12 | 26 | 4642 | 5254 | 5089 | 160.0 |
| 2020-04-17 | 24 | 4820 | 5345 | 5176 | 124.5 |
| 2020-10-09 | 65 | 4842 | 5436 | 5262 | 141.4 |
| 2020-10-24 | 45 | 4855 | 5425 | 5197 | 134.5 |
| 2020-10-29 | 41 | 5300 | 5814 | 5409 | 120.2 |
| 2020-11-08 | 106 | 5072 | 5804 | 5494 | 153.6 |
| 2020-11-13 | 108 | 5058 | 5806 | 5533 | 138.0 |
| 2020-11-14 | 50 | 5197 | 5815 | 5527 | 143.8 |
| 2020-11-18 | 79 | 4722 | 5677 | 5408 | 177.5 |
| 2020-11-23 | 100 | 4974 | 5673 | 5454 | 142.4 |
| 2020-11-28 | 86 | 4891 | 5656 | 5411 | 164.2 |
| 2020-11-30 | 47 | 5125 | 5690 | 5480 | 139.3 |
| 2020-12-03 | 105 | 5013 | 5824 | 5525 | 146.2 |
| 2020-12-08 | 93 | 5078 | 5814 | 5544 | 140.9 |
| 2020-12-13 | 27 | 4815 | 5682 | 5373 | 186.1 |
| 2020-12-18 | 91 | 5078 | 5829 | **5546** | 136.3 |
| 2020-12-28 | 26 | 4912 | 5636 | 5362 | 203.4 |
| 2022-04-12 | 99 | 4965 | 5630 | 5404 | 145.8 |
| 2022-10-24 | 71 | 4858 | 5562 | 5304 | 162.1 |
| 2022-11-03 | 74 | 4874 | 5619 | 5340 | 145.4 |

| | | | | | |
|---|---|---|---|---|---|
| 2022-11-04 | 33 | 5099 | 5665 | 5432 | 151.6 |
| 2022-11-13 | 91 | 5015 | 5695 | 5404 | 143.7 |
| 2022-11-20 | 47 | 5097 | 5658 | 5430 | 138.6 |
| 2022-11-23 | 99 | 4973 | 5744 | 5447 | 147.2 |
| 2022-11-28 | 96 | 4968 | 5721 | 5429 | 143.0 |
| 2022-12-03 | 100 | 4977 | 5735 | 5455 | 146.8 |
| 2022-12-08 | 97 | 5059 | 5786 | 5481 | 148.4 |
| 2022-12-18 | 71 | 5183 | 5647 | 5438 | 115.4 |
| 2022-12-23 | 24 | 4655 | 5602 | 5309 | 215.3 |
| 2022-12-28 | 80 | 5018 | 5763 | 5449 | 149.7 |
| 2023-01-07 | 25 | 4885 | 5634 | 5297 | 163.7 |
| 2023-01-12 | 34 | 5091 | 5649 | 5394 | 158.2 |
| 2023-01-17 | 72 | 5227 | 5781 | **5506** | 122.4 |
| 2023-01-22 | 35 | 4673 | 5652 | 5324 | 215.8 |
| 2023-01-27 | 19 | 4953 | 5555 | 5295 | 162.5 |